Investigation of Overpotential Distributions in a Solid Oxide Electrolysis Cell using Experimental and Modeling Approaches

Emilia Pasik

Master Thesis

This report is composed in the program LaTeX.

AAU Energy
Aalborg University
http://www.aau.dk

AALBORG UNIVERSITY
STUDENT REPORT

Title:
Investigation of Overpotential Distributions in a Solid Oxide Electrolysis Cell using Experimental and Modeling Approaches

Theme:
Solid oxide cells

Project Period:
Spring Semester 2025

Project Group:
HYTEC4

Participant(s):
Emilia Pasik

Supervisor(s):
Torsten Berning
Marius Müller

Page Numbers: 93

Date of Completion:
25.05.2025

Abstract:

This thesis investigates the distribution of overpotentials in a solid oxide cell using both experimental and modeling methods. A 3D finite element model is employed in COMSOL Multiphysics to simulate electrochemical, thermal, and transport phenomena. Experimental validation includes *I/U* curve measurements, electrochemical impedance spectroscopy, and gas composition analysis via mass spectrometry. The model shows good agreement with experiments and is able to capture variations in overpotentials along the cell. Electrolysis operation at thermoneutral voltage is studied in detail with the model to evaluate overpotentials and local heat sources and sinks. The results highlight the importance of spatially resolved modeling in understanding and optimizing solid oxide cell performance. The model enables detailed analysis of current density distribution, local overpotential behavior, and heat source contributions. Combined with experimental data, it provides a valuable tool for evaluating operating strategies and guiding design improvements in high-temperature electrolysis systems.

Summary

This thesis explores the spatial distribution of overpotentials in a solid oxide electrolysis cell using a combined experimental and modeling approach. The motivation behind the work is to support the industrial development of solid oxide technology as the energy production in Europe is hoping to partially rely on hydrogen. By understanding where and why overpotentials arise within the cell, it becomes possible to optimize both performance and durability of high-temperature electrolysis systems.
The investigated cell is a commercially available solid oxide cell from Elcogen with an active cell area of 16 cm^2, with a planar design and anode support structure. The cell consists of a Ni-YSZ fuel electrode, a YSZ electrolyte with a GDC barrier layer, and an LSC air electrode. The study is carried out in collaboration with Robert Bosch GmbH, using both experimental and simulation tools. Key techniques include electrochemical impedance spectroscopy, current-voltage measurements, and real-time gas composition analysis using mass spectrometry. These measurements are supported by a finite element model developed in COMSOL Multiphysics based on the works of H.Geisler [1], A.Leonide [2] and N.Russner [3]. The model simulates the electrochemical behavior, species transport, and heat transfer phenomena in 3D.
The modeling approach includes charge transport (both ionic and electronic), electrochemical reaction kinetics, multi-component gas diffusion (via the Dusty Gas Model), convective gas flow, and heat generation from both reversible and irreversible sources. The model geometry replicates a single cell in a stack configuration, and incorporates real cell dimensions and microstructural parameters derived from an analytical report from Bosch. In the model, in order to save computational resource, symmetry boundary is applied, allowing to simulate only half of the cell. The mesh applied on the geometry is validated through a grid independence study. Particular attention is given to the modeling the electrode-electrolyte interfaces, as that is where the activation overpotentials are defined.
Experimentally, the setup consists of a FuelCon Evaluator test bench, FRA Zahner Zennium X with Power Potentiostat 241 for EIS and *I/U* curves, and a mass spectrometer for real-time gas composition analysis. Measurements are carried out at 600°C and 700°C under various fuel and oxidant compositions, and both galvanostatic and potentiostatic modes are used. A key goal is to assess fuel utilization and gas conversion using MS. Due to unforeseen complication, a separate cell holder is implemented to improve sealing and minimize water condensation in the exhaust lines.Due to excessive leakage of the first iteration of the cell holder, the initial concept of measuring the gas composition at five different points along the cell length had to be adjusted to fit the project time frame. That however means that the gas composition can only be assessed at the outlet of the testing rig.
The thesis demonstrates that the COMSOL model reproduces the cell behavior realistically. Validation against *I/U* curves shows good agreement under both electrolysis (steam-rich) and fuel cell (hydrogen-rich) operating conditions. The model captures all key loss mechanisms,

including activation, ohmic, and concentration overpotentials. In the model, a detailed investigation of each overpotential is conducted. The model is able to spatially resolve the overpotentials. They are analyzed deeply at thermoneutral voltage operation.
The activation overpotential is found to be significantly higher on the fuel side than on the air side, with a decreasing trend along the cell length.
Ohmic overpotential is reassessed using a mixed empirical and theoretical approach, where experimental resistances are used to derive a surface resistance for the interdiffusion layer. The ohmic overpotential in the GDC layer, electrolyte and ID layer is decoupled which allows to scale the thicknesses of electrolyte and GDC layer, without inaccurately over- or underestimating the resistance of interdiffusion layer. This layer remains at constant thickness, regardless of the electrolyte or GDC sizes.
The concentration overpotential is found to be dominated by gas conversion losses, while diffusion overpotential is small for the air electrode due to low electrode thickness on the air side. The gas conversion losses are expected to have significant influence on the total overpotential in larger active area cells. That is why a cell with larger active area is chosen, as investigating the gas conversion along the length of the cell is the primary goal.
Mass spectrometry measurements provide insights into gas conversion behavior. At high steam content, water accumulation in the outlet lines limits the reliability of MS data. However, under lower humidification, the experimental and modeled gas compositions align well. The MS results also confirm oxygen leakage into the fuel side, which is quantified through stoichiometric analysis and accounted for in the model. Gas conversion loss emerges as the dominant form of concentration overpotential, especially at the outlet. There, the fuel mixture is much more hydrogen-rich than at the inlet, which causes the reaction to run slower, due to partial fuel starvation.
Thermoneutral voltage operation is investigated in the model in great detail to assess local temperature gradients and the influence of each heat source and sink, with particular focus on thermodynamics. The global temperature remains stable at 700°C at potentiostatic operation, with operational voltage of 1.2725 V. Local temperature still changes near the air electrode and metallic interconnector ribs due to contact resistance resulting in joule heating effects. Heat source analysis shows that contact losses contribute the most to internal heat generation, followed by ohmic and activation losses. The model predicts that even small deviations from thermoneutral voltage (e.g., operating at 1.3 V instead of 1.2725 V) can introduce measurable, although small, temperature gradients along and across the cell.
The thesis concludes that spatially resolved modeling, when validated experimentally, is a powerful tool for solid oxide cell diagnostics and design. The developed finite element model successfully captures the interplay between gas composition, overpotential distribution, and temperature gradients, providing detailed insights into local performance.

Preface

This report is written on the 4st semester in the master program *Fuel Cells and Hydrogen Technology* at the Faculty of Engineering and Science at Aalborg University. The report is written in the period from February 1th to May 25th 2025 from the semester theme that is *Solid Oxide Cells*. The Thesis is written in a collaboration with Robert Bosch GmbH.

Reading Guide

The references to literature in the report is done using the Vancouver method. The references are shown as [number], representing the order for which the reference appears in the project. The first reference can thereby be seen as [1]. A bibliography is included at the end of the report where the references along with the information of the source appear.
The main part of the project is divided into chapters and sections with assigned numbering as seen in the table of contents. Appendices are labeled with a letter. Figures, tables and equations are assigned numbers after which order they appear in the given chapter.
The report includes a nomenclature containing an overview of the used symbols and abbreviations arranged alphabetically.

Acknowledgments

The author would like to acknowledge professor *Torsten Berning* for supervision and help throughout the project on the Aalborg University side, as well as *Marius Müller* and *Jean-Claude Njodzefon* on the Robert Bosch GmbH side.

Emilia Pasik
<epasik23@student.aau.dk>

Nomenclature

Symbol	Description	SI Unit
c	Concentration	$[mol/m^3]$
$\mathbf{c}$	Vector of concentration	$[mol/m^3]$
d_{por}	Pore diameter	[m]
j	Current density	$[A/m^2]$
j_{ct}	Charge transfer current density	$[A/m^2]$
j_0	Exchange current density	$[A/m^2]$
k_i	Thermal conductivity	$[W/mK]$
$\dot{m}$	Mass flow	[kg/s]
n	Molarity	[mol]
$\mathbf{n}$	Vector of directions	[-]
n_e	Number of electrons	[-]
$\dot{n}$	Molar flow rate	[mol/s]
p	Pressure	[Pa]
p_i	Partial pressure	[Pa]
u	Velocity magnitude	[m/s]
$\mathbf{u}$	Vector of velocities in all directions	[m/s]
x	Molar fraction	[-]
A	Area	$[m^2]$
$C_{p,i}$	Specific heat	$[Jkg/K]$
D_{ab}	Binary diffusion coefficient	$[m^2/s]$
D_{bulk}	Bulk diffusion coefficient	$[m^2/s]$
E_{act}	Activation energy	[J/mol]
$\mathbf{E}$	Electric field	$[V/m]$
F	Faraday constant	[C/mol]
ΔG_0	Gibbs free energy	$[J/mol]$
ΔH_0	Enthalpy	$[J/mol]$
I	Current density	$[A/m^2]$
K_n	Knudsen number	[-]
M_i	Molar mass	[g/mol]
R	Gas Constant	$[J/molK]$
$R_{ele/ion}$	Electronic/Ohmic resistance	[Ω]
Q	Heat	[W]
δS	Entropy	[J/K]
T	Temperature	[K]
U	Voltage	[V]
U_N	Nernst voltage	[V]
U_{rev}	Reversible voltage	[V]
U_{tn}	Thermoneutral voltage	[V]
$\dot{V}$	Volumetric flow rate	$[m^3/s]$
X	Gas conversion	[-]
Z	Impedance	[Ω]

Nomenclature

Symbol	Description	SI Unit
α	Charge transfer coefficient	[-]
γ	Butler-Volmer Equation prefactor	[-]
ε	Volume fraction	[-]
η	Loss/Overpotential	[V]
κ	Permeability	$[m^2]$
μ_i	Dynamic viscosity	$[Pa \cdot s]$
ρ_i	Density	$[kg/m^3]$
σ_i	Conductivity	$[S/m]$
σ_{ab}	Conductivity	[S/m]
τ	Turtuosity	[-]
ϕ	Potential	[V]
φ	Amplitude	$[V$ or $A/cm^2]$
ω	Frequency	[Hz]

Sub-/superscript	Description
x_0	Standard
$x_{ion,ele}$	Ionic, electronic
$x_{pol,ohm,act,conc,diff,cont}$	Polarization, Ohmic, Activation, Concentration
x_{op}	Operating point
$x_{AE,FE}$	Air electrode, Fuel electrode
$x_{FC,EC}$	Fuel cell, Electrolysis

Abbreviations

Abbreviation	Description
AE	Air electrode
AFL	Anode functional layer
ASR	Area specific resistance
BC	Boundary condition
DGM	Dusty Gas Model
DRT	Distribution of relaxation times
EC	Electrolyser cell
ECM	Equivalent circuit model
EIS	Electrochemical impedance spectroscopy
Ely	Electrolyte
FC	Fuel cell
FE	Fuel electrode
FEM	Finite element model
FRA	Frequency response analyzer
GDC	Gadolinium doped Cerium
GCI	Grid independence index
ID	Interdiffusion
HTSE	High temperature steam electrolysis
LSCF	Lanthanum Strontium Cobalt Ferrite
MFC	Mass flow controller
MIC	Metallic interconnector
MIEC	Mixed ionic electronic conductivity
MS	Mass Spectroscopy
OCV	Open circuit voltage
SOEC	Solid oxide electrolyser cell
SOFC	Solid oxide fuel cell
SOC	Solid oxide cell
TNV	Thermoneutral voltage
YSZ	Yttria supported Zirconia

Contents

Chapter 1

Introduction

As the world's population keeps increasing, the energy consumption rises, which leads to higher demand for energy. Heightened energy production causes then increase in harmful emissions. The energy industry is responsible for approximately three quarters of greenhouse gas emissions and thus holds the key to limiting the most severe effects of climate change [4]. Therefore the global urge to reduce the amount of emitted harmful gases has been rising in recent decades.

Hydrogen, obtained through electrolysis, is an excellent energy carrier to store energy from intermitted sources, working dependent on sun or wind availability, rather than on demand. Therefore, to overcome this supply and demand mismatch, an energy storage solution is necessary, which if done through hydrogen can either be converted back directly to electricity in fuel cells or can be further processed within other sectors [5].

Fuel Cell's (FCs) convert water to hydrogen and electrical power. That means this process does not cause any harmful emissions by itself. The inhibitions, due to which FCs are not as wide spread are high manufacturing costs for efficiency similar to energy from traditional sources (~60%), unless integrated into a combined heat and power system (up to ~90%) [6].
As hydrogen is often sourced from syngas or biogas derived from fossil fuels (97% of all hydrogen in 2019) [7], these hydrocarbons must be reformed first. This reforming process is endothermic and releases carbon oxides into the environment. However, with technological advancements, more sustainable options emerge. FCs can be integrated with electrolysers in a closed-loop system. The electrolyser cell (EC) is able to produce green hydrogen, when supplied with electrical energy from renewable sources. The hydrogen is then stored, as mentioned above, ready to be converted back to electricity.
High temperature steam electrolysis (HTSE) using solid oxide electrolysis cells (SOECs) offers higher electrical efficiencies, due to faster kinetics and favorable thermodynamics at elevated temperatures in comparison to low temperature electrolysis [8]. Thus, SOECs present themselves as a promising technology for the hydrogen economy of the future. The industrialization of this technology requires more development. To improve the understanding of occurring loss processes in solid oxide cells (SOCs), physical models based on experimental parametrization and validation are employed.

1.1 Problem statement

The targeted development and operation of solid oxide cells at high efficiency and durability requires a detailed understanding of where and how losses —overpotentials— occur inside the cell during operation. While performance of the entire cell is readily measured by experimental means of e.g. electrochemical impedance spectroscopy and current-voltage curves, it does not reveal the spatial distribution of these losses resulting from their dependency on local gas composition and temperature. This lack of spatial resolution for experimental investigations limits the ability to validate distributions determined by spatially resolved models. Thermoneutral voltage is the targeted operating point for electrolysers, as it represents a thermal balance between the heat consumed and generated within the cell. Therefore, precise knowledge of local temperature variations and internal heat sources or sinks is essential to understand the cells's thermal behavior.

This thesis addresses this by combining experimental methods and spatially resolved modeling to investigate the distribution of activation, ohmic, and concentration overpotentials within a commercially available solid oxide cell. The goal is to identify dominant loss mechanisms, understand their spatial variation, and validate model predictions with experimental data. Ultimately, this approach aims to support the development of high-performance and robust solid oxide cells through better-informed design and operation.

Chapter 2

Theoretical Background

This chapter comprises the fundamentals of SOC technology, its performance and characterization and offers an introduction to the measurement of electrochemical impedance of the cells as well as tools to analyze the the obtained results.

In this work, a reversible solid oxide cell is investigated, but focusing mainly on the electrolysis mode. It means that the cell can operate in both FC and EC mode. The FC mode, however, has the same general rules of operation, but the reactions run in reverse compared to the EC mode. Due to the reversibility of the direction of the current the following naming convention is taken on for the electrodes. Instead of using the standard 'anode' for oxidation electrode and 'cathode' for reduction electrode, the electrodes are named after the gasses that flow through them. In EC mode, the fuel electrode will host an oxidation reaction and will be the anode, whereas in FC mode, the fuel electrode will host a reduction reaction, thus becoming the cathode. Using the name 'fuel/air electrode' allows to avoid confusion, when talking about cell layers and operation later on.

2.1 Working principle of a solid oxide cell

The structure of a solid oxide cell is similar to that of batteries, since both have an anode and a cathode connected by a conductive material. However, the difference lies in the fact that there is a constant supply and outflow of fuel and air into and from the cell [9].
The atmospheres of fuel and oxidant gases are separated by a gas-tight layer (electrolyte), which splits the reaction into spatially divided electrochemical half-reactions. The solid electrolyte is conductive for oxygen ions in high temperatures. Steam in EC mode is reduced at the fuel electrode from H_2O to O^{2-} by accepting $2e^-$. This is an endothermic reaction that requires supplied energy from an external voltage source. This half reaction in shown in the Equation 2.1.

$$H_2O + 2e^- \rightleftharpoons H_2 + O^{2-} \qquad \textbf{fuel electrode (FE), anode in EC mode} \tag{2.1}$$

The oxygen ions diffuse through the electrolyte, because of the difference in chemical potential on both sides of it. At the air electrode-electrolyte boundary the oxygen ions give up the electrons and form oxygen molecules. This can be seen in the Equation 2.2.

$$O^{2-} \rightleftharpoons \frac{1}{2}O_2 + 2e^- \qquad \textbf{oxygen electrode (AE), cathode in EC mode} \qquad (2.2)$$

The voltage source imposes an additional difference in electric potential between the two electrodes. The negative terminal of the voltage source pushes electrons toward the FE, making it more electron-rich (negative potential), while the positive terminal pulls electrons away from the AE, making it more electron-deficient (positive potential). [10]. The working principle is presented in a simplified manner in the Figure 2.1.

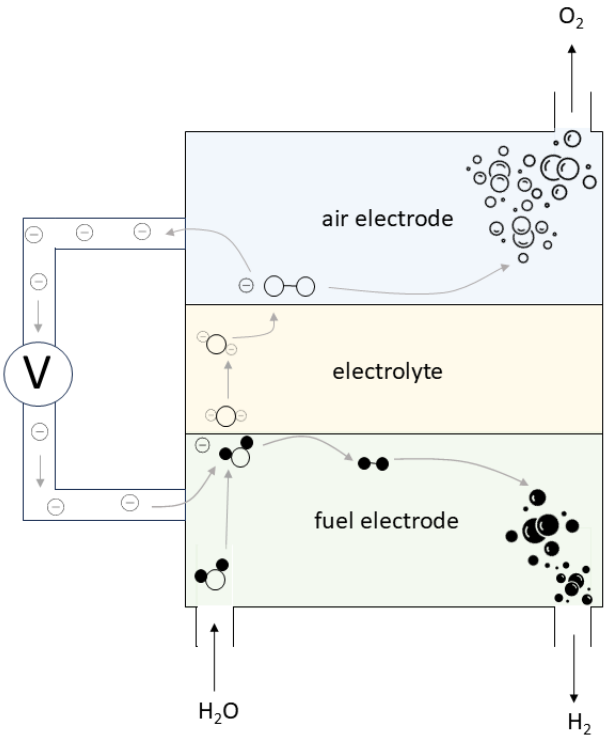

Figure 2.1: This figure illustrates spatial separation of the reaction happening in the cell. Oxygen is represented with unfilled bubbles, hydrogen with black, and the electrons have a "-" sign in the middle. The gray arrows show how the processes follow.

2.1.1 Materials in a solid oxide cell

The performance and functionality of SOCs rely on the choice of materials for the electrolyte and electrodes. A planar anode supported cell composition, that is used in this project, is visualized in the Figure 2.2.

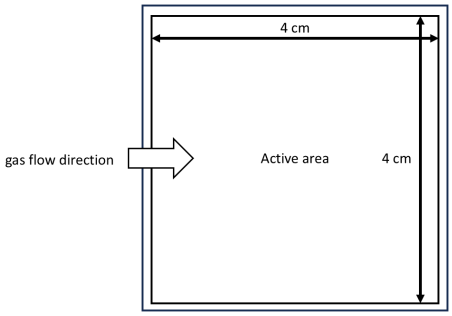

(a) Top view. From the top the AE active area is seen.

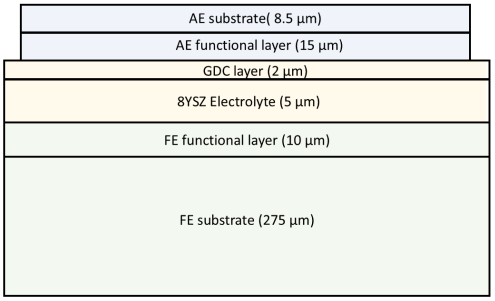

(b) Side view. From the side a cross-section of all the layers of the investigated cell is seen.

Figure 2.2: Cells consist of two electrodes and electrolyte of specific material and thickness. The colors are added to the side view of the cell to match the Figure 2.1. Figured inspired by A.Leonide [2].

The characteristic name of the cell points to the material of electrolyte. Crystalline oxide ceramic electrolytes conduct oxygen ions by lattice defect hopping mechanisms, caused by lattice vibrations, that only become significant at high temperatures, above 500°C. Yttria-stabilized zirconia, known as YSZ, is a ceramic oxide, with crystalline fluorite structure, that are widely used as electrolytes in SOC.
YSZ is the state of art electrolyte material, due it its relatively high ionic conductivity. The material is ZrO_2 doped with either 3 or 8% mol of Y_2O_3. The more yttria doping the better is the ionic conductivity, but the mechanical stability of the material worsens. The reason is that yttria introduces more oxygen vacancies in the lattice.
The cerium doped gadolinium (GDC) barrier layer allows to avoid chemical reaction between the electrolyte and the oxygen electrode, preventing the formation of less conductive interdiffusion layers in-between [11]. Besides the electrolyte, two porous electrodes, with a functional and substrate (contacting) layer each, are also necessary for high performance operation.

The electrochemical reactions can only occur when cell material molecules, ions and electrons meet at the catalytic active sites. SOC electrodes should ideally be porous and mixed ionic and electronic conductors (MIEC).
The AE should provide high electrochemical reactivity for oxygen. Therefore, only the ceramic materials that are stable and conductive at high temperatures and high oxygen partial pressures should be considered. Various lanthanum based perovskites oxides with good physical and chemical stability have been investigated. Iron-doped lanthanum cobaltites (LSCFs) have displayed MIEC properties at high temperatures and have not chemically interacted with electrolytes and therefore are a good choice for the AE material [9], [11].
Ni-YSZ solid mixtures are often used materials for the FE. They are prepared by sintering NiO and YSZ powders together, to obtain a NiO/YSZ composite. Sintering is a process of heating a powdered material to bond the particles together, increasing their strength and density. In reducing atmospheres (high H_2 content), the NiO phase is reduced to Ni, resulting in a desired porous Ni-YSZ electrode. Increased porosity is induced with intent, Ni has smaller volume than NiO and electrodes are manufactured to obtain a porous microstructure after reduction [12]. NiO is used initially as it has greater stability in powdered form during sintering but also because in contact with oxygen there is no risk of oxidation, unlike for Ni. Ni provides electrical conductivity and catalytic activity, while the YSZ provides ionic conductivity, as well as the structural stability. However, this ceramic-metal material presents some disadvantages that are

related to Ni coarsening while re-oxidation, which decreases the performance. [11].

2.2 Cell Performance

Cell performance is most commonly summarized with current-voltage curves (*I/U* curves). Since cells with larger areas are able to process (produce or utilize) more electricity, the curves should be normalized by the active area for comparison. An example of that graph is shown below in Figure 2.3. [10]
In the FC mode the higher the current density the lower the voltage, resulting in a decreasing curve, due to electrical resistances. For the EC mode voltage is supplied to the cell, so the goal is to achieve the highest absolute current density at the lowest voltage possible.

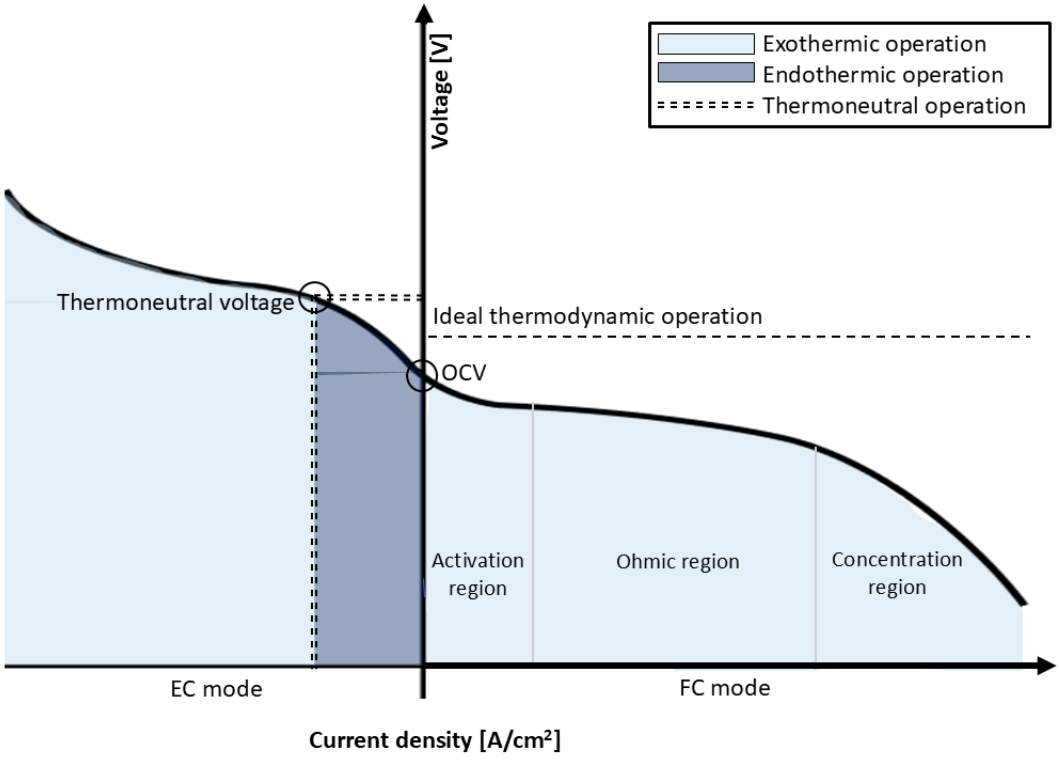

Figure 2.3: *I/U* curve for electrolysis mode (left) and fuel cell mode (right). Loss mechanisms regions are the same for the electrolysis, and are not marked to keep clarity on the plot. Figure inspired by [10].

In the Figure 2.3 the horizontal dashed, single line symbolizes the ideal cell performance predicted through the theoretical thermodynamic Nernst voltage - the maximum voltage output in FC operation, or minimum voltage supplied for electrolysis, which is explained in more detail later. It is described with the Equation 2.3. U_N is shown in the plot as a horizontal line (no slope or curve), which reflects an idealized case assuming constant gas composition equal to inlet conditions, no parasitic losses and no polarization loss. In reality, due to gas conversion, the local Nernst voltage changes along the cell, which is explored results in Chapter 5.3. Gibbs free energy included in the formula is a function of operating temperature and is calculated according to the formula in Equation D.15 present in Appendix D [10].

$$U_N = \frac{\Delta G_0(T)}{n_e F} - \frac{RT}{n_e F} \cdot ln\left(\frac{p_{H_2O,FE}}{\sqrt{p_{O_2,AE}} \cdot p_{H_2,FE}}\right) \tag{2.3}$$

The Nernst potential is shown in the plot as a horizontal line (no slope or curve), which means that an ideal (theoretical) cell maintains the constant voltage without losses. At open circuit voltage (OCV) a real cell voltage values lay below the ideal prediction, due to gas leakages altering gas composition. The OCV is the highest cell voltage achievable in an actual cell operation, or the lowest possible voltage in an actual EC operation [10].

Electrolysis operation and thermoneutral voltage

The whole cell operation in EC mode can be either endo- or exothermic, depending on the supplied voltage at a given temperature, as shown in the exemplary *I/U* curve in the Figure 2.3 with two shades of blue. The electrochemical reaction in EC mode always remains endothermic. Despite water splitting reaction remaining endothermic, the heat generated by the irreversible losses in the cell can offset that energy demand. To explain this phenomenon, the behavior of thermodynamic functions in an electrolysis cell is shown in the Figure 2.4.

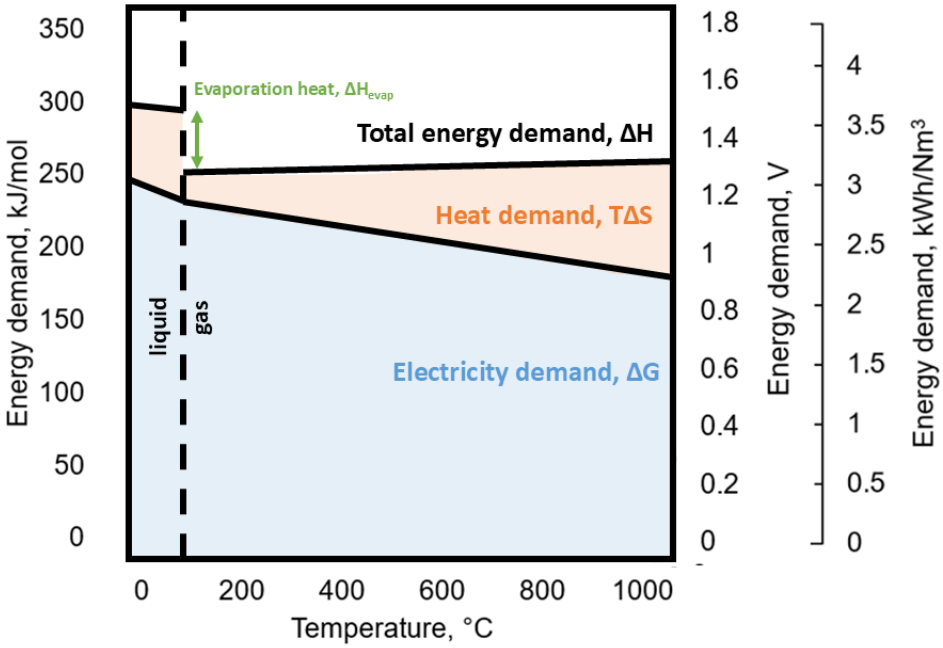

Figure 2.4: The relation between the two y-axes is simply the fact that energy measured in unit of "volt (V)" is equal to energy measured in unit of "kJ/mol" divided by 2F (2 comes from the exchange of 2 electrons per molecule in the reactions, F is Faraday number). Figure inspired by M.Mogensen [13].

To express the minimal, thermodynamic amount of voltage that needs to be supplied to operate the cell in the EC mode, reversible voltage/equilibrium voltage, described with Equation 2.4, is used [9]. This is a simplification of the Nernst voltage from Equation 2.3. $\Delta G_0(T)$ is temperature dependent Gibbs free energy of formation of the electrolysis products. The electrolyzer cell must

be operated above that value, so $U_{op} > U_{rev}$ always.

$$U_{rev} = \frac{\Delta G_0(T)}{n_e F} \tag{2.4}$$

In the Figure 2.4 also $\Delta H_0(T)$ is present, it denotes the enthalpy of formation of the electrolysis products as it is the total energy that is necessary to apply for the electrolysis process. Enthalpy covers both electricity and heat demand of the cell.
As mentioned above, at higher voltages (as consequence, higher current densities) the irreversible losses in the cell produce enough of heating to cover the heat demand, $T\Delta S$, (also shown in the figure) of the endothermic reaction in the cell. In other words, the rate of delivery of heat is higher than the rate of energy consumption. There is a certain voltage point at which both rates are equal, and this point is called the **thermoneutral voltage** (TNV).
This thermodynamical balance allows to define TNV only utilizing the enthalpy, $\Delta H_0(T)$, as seen in the Equation 2.5 [13]. This point can be observed on the *I/U* curve at around 1.3 V in the Figure 2.3. This value is often rounded up in literature to 1.3 V, whereas in reality $U_{tn} \approx 1.2725\ V$ in 700 °C.

$$U_{tn} = \frac{\Delta H_0(T)}{n_e F} = \frac{245.5\ \text{kJ/mol}}{2 \cdot (9.648 \cdot 10^4\ \text{C/mol})} \approx 1.2725\ V \tag{2.5}$$

The thermoneutral voltage can also be expressed in terms of entropy and Gibbs free energy. The notation would take the form of Equation 2.7, where $Q\ [kJ/mol]$ is the heat demand of the reaction. That heat is defined as $Q = T \cdot \Delta S$, where ΔS is the entropy change of the system.
Knowing the definitions of voltages given in Equations 2.4, 2.5 and using a definition of the Gibbs free energy in Equation 2.6 it can be deduced that this heat demand is the difference of U_{rev} and operating voltage, U_{op}, as can also be seen in the Figure 2.4, and for the case of $U_{op} = U_{tn}$ this difference equals zero.

$$\Delta G = \Delta H - T \cdot \Delta S \tag{2.6}$$

$$Q = (U_{tn} - U_{op}) \cdot n_e F = 0 \tag{2.7}$$

When the cell is operated above TNV ($U_{tn} - U_{op} < 0$), extra heat is generated and energy expenditure for cooling lowers the overall efficiency of the device. When operated below the TNV ($U_{tn} - U_{op} > 0$), the cell requires additional heating to maintain its operating temperature. It is therefore desired to operate an electrolyzer at the voltage of *ok*. $1.3V$, to achieve the highest thermodynamic efficiency [8].

2.2.1 Overpotentials

It is challenging to achieve high current densities, while maintaining low operating voltage, because of irreversible losses in the cell [9]. These losses stem from species or charge transport and electrochemical reactions kinetics. The losses are interchangeably called 'overpotentials' as to overcome the resistances, caused by the losses, some of the operating voltage needs to sacrificed. So 'overpotential', expresses the additional voltage (extra potential) required to overcome irreversible losses while operating the cell.

- **parasitic loss** - results from electrolytes not being gas-tight (leakages). They affect the

Nernst voltage [2].

- **ohmic loss** - arises, because of charge transport resistances. Mostly, because of the ionic transport (O^{2-}) through the electrolyte and barrier layer, but also contains a small contribution from electron charge transport. This loss is linear on the *I/U* curve.
- **activation loss** - stems from electrochemical reaction kinetics, due to activation energy required for the electrochemical reactions at both electrodes. [9]
- **diffusion loss** - arises, because of mass transport in the electrodes (diffusion) and flow structures (forced convection). Reactant depletion (or product accumulation) will cause adverse changes in concentration gradients, lowering the potential difference between the electrodes, according to the Nernst voltage Equation 2.3. [9]
- **gas conversion loss** - is the consequence of changing gas composition along the cell. An increasing current density results in an increased consumption of supplied gasses and eventually in the fuel depletion. This results in a changing $p_{O_2,FE}$ and $p_{O_2,AE}$ ratio. As a consequence U_N is unfavorably impacted [2].
- **concentration loss** - is the sum of diffusion loss and gas conversion loss
- **polarization loss** - is the sum of activation loss and concentration loss

After considering all the losses in the cell it is possible to distinguish between ideal and real operation, as shown in the Equation 2.8. Each type of loss is denoted as η, with a subscript indication: η_{pol} for polarization loss, η_{ohmic} for ohmic loss, η_{act} for activation loss and η_{conc} for concentration loss [9]. In case of η_{ohmic} a distinction for ionic and electronic charge transport losses is included.

$$U_{ideal} = U_N - \eta_{pol} - \eta_{ohmic} = U_N - (\eta_{act} + \eta_{diff}) - I \cdot (R_{ele} + R_{ion}) \tag{2.8}$$

In order to parameterize and develop more efficient SOCs the performance-related polarization processes have to be studied. In contrast to *I/U* curves, where only the overall loss of a cell can be identified, electrical impedance spectroscopy (EIS) is able to reveal the fraction of a single overpotential on total overpotential [2].

2.3 Electrochemical Impedance Spectroscopy

Electrochemical Impedance Spectroscopy (EIS) yields detailed information about the cell but is also demanding in terms of setup, settings and measurement time. It measures the frequency dependent resistance of the cell (dynamic behavior), called the impedance $Z(\omega)$ [14].

The operational impedance is the ratio of Laplace transforms of potential and current in the presence of resistance, including capacitance, and inductance. The total impedance can be calculated from Ohm's and Kirchhoff's laws. It is a complex quantity with a real part (resistance) and an imaginary part (reactance) as can be seen in the Equation 2.9. The reactance comes mainly from capacitance due to ion transport and charge accumulation (double-layers) within the cell, while the effect of inductance is negligible for the cell itself, in a measurement setup it can play a more significant role.[15].

$$Z(\omega) = Z_{real}(\omega) + iZ_{imag}(\omega) \tag{2.9}$$

The standard approach to measurements is to apply a sinusoidal alternating current, which excites the cell into a harmonic oscillation around the operating point, this is depicted in the Figure 2.5. The voltage response of the cell is measured and the phase shift and change in amplitude between the signal and the response is calculated. [2].

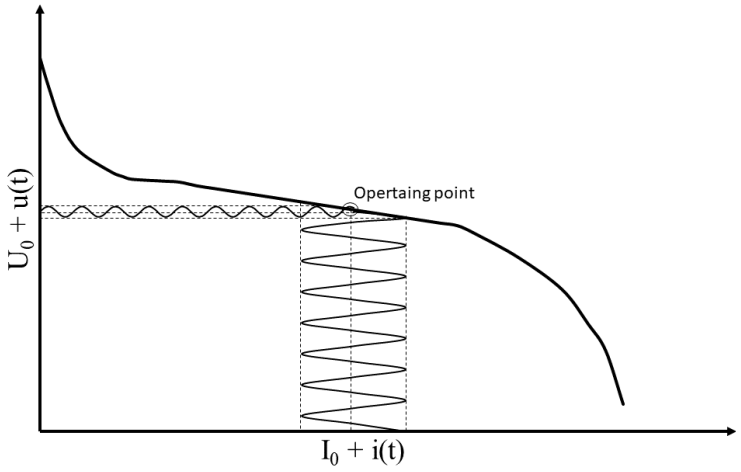

Figure 2.5: Illustration of the impedance measurement with the corresponding *I/U* curve. Inspired by H.Geisler [1]

For each frequency ω, a separate measurement is conducted with the excitation signal $\mathrm{I}(t)$ consisting of a constant bias (external load), I_0, superposed by a sinusoidal signal with the amplitude φ as shown in the Equation 2.10.

$$I(\omega) = I_0 + I \cdot sin(\omega t + \varphi) \tag{2.10}$$

Consequently, the measured system response of $\mathrm{U}(t)$ is the result, provided that the measured spectrum is linear, which is a requirement for an impedance measurement. Non-linearity of the spectrum can be caused by a too large perturbation amplitude. From these response signals impedance for the entire frequency spectrum can be determined, according to the Equation 2.11 [14].

$$Z(\omega) = \frac{U}{I} \cdot e^{i\cdot(\omega t(\varphi_U - \varphi_I))} \tag{2.11}$$

In contrast to static *I/U* curve measurement, the transient EIS measurement relies on the fact that different processes in the cell occur at different time constants (relaxation times). This refers to the time that a process requires to return to an equilibrium state after perturbation [16].
Some slower processes, e.g diffusion in the electrodes, are not able to 'react' quickly enough to high frequency perturbations and are only detectable with lower frequency signals . While faster processes display significant enough difference in reactance at high frequencies already. An example of such process is the charge transfer reaction at the FE [17]
.
The frequency response analyzer (FRA) software is able to calculate the real and imaginary

part of the impedance and output an impedance spectra that is presented as a Nyquist Plot. A Nyquist Plot is a complex plane on which $-Z_{imag}$ vs Z_{real} is be displayed. From the plot, information about the resistances of the cell can be read, but also a more in-depth analysis into the single loss mechanisms can be conducted.
It is important to note that the frequency is only implicitly included in the plot, as each data point represents one frequency. High frequencies are on the left, while lower frequencies are on the right.

The high frequency intercept with the real axis corresponds to the purely ohmic resistance (R_0) of the cell, whereas the intercept at the lowest frequency is called area specific resistance (ASR) of the cell. The difference between R_0 and ASR is the polarization resistance (R_{pol}) of the cell, previously introduced as a sum of activation and concentration resistances. The summation of R_0 and R_{pol} is also known as total resistance of the cell ($R_{tot} = ASR_{cell}$) [2].
Those resistances, when related to the differential current at the measured point, correspond to the losses discussed in the Section 2.2.1. R_0 aligns with η_{ohmic} and R_{pol} coincides with η_{pol}.
The figure Figure 2.6 shows an exemplary Nyquist plot, with all the crucial elements discussed in the paragraph. The frequencies are denoted with ω, and the resistances are indicated with arrows.

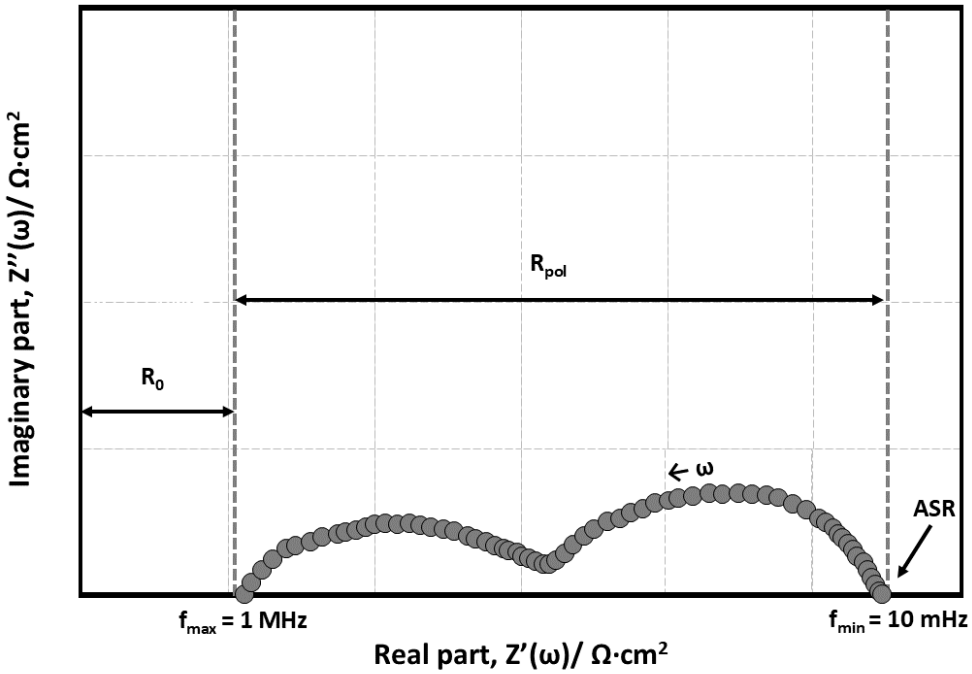

Figure 2.6: Typical Nyquist plot with annotations of the most important elements. Inspired by H.Geisler [1].

2.3.1 Equivalent Circuit Model

Since impedance is a complex quantity, it can be broken down into its fundamental components and presented as an electrical circuit using resistors and capacitors as well as other elements. That allows to use the impedance functions of those simpler elements to fit parameters of said functions as close as possible to the experimental data. Each element in an equivalent model should represent a specific loss process occurring in the cell [1]. A circuit prepared for that purpose is called an Equivalent Circuit Model (ECM). The most basic element of an ECM (be-

sides a simple resistor, equivalent to ohmic resistance) is a parallel connection of a resistor and a capacitor, called RC-element. It assumes ideal capacitive behavior. However its plot (perfect semicircle) on the EIS spectrum of a real cell might be equivalent to more than one process, because the processes represented by those elements overlap in the frequency and are almost impossible to distinguish through a singular measurement.
In real electrochemical systems, ideal capacitive behavior is rarely observed. To better capture the distributed or non-ideal nature of capacitive processes, a constant phase element is often used instead of a pure capacitor. This is called an RQ-element, which produces flatter semicircles in Nyquist plots and provides a more realistic representation of the impedance behavior.

The result of an ECM well fitted with experimental data is the resistance and characteristic frequency of each process. When a series of measurement with variation in load, fuel composition or temperature is fitted like this, it is possible to verify resistance of which element is dependent on a given variation. Allowing then to attribute certain resistances to real processes in the cell and also quantify them. It is a difficult task, therefore an additional analysis called distribution of relaxation times is often carried out before fitting.

Chapter 3

Model

The presented model of a cell in a stack is solved numerically using the finite element method (FEM) in the commercial software COMSOL Multiphysics v6.2 and draws from literature - dissertation by H.Geisler [1], A.Leonide [2] and N.Russner [3]. An explanation of the FEM can be found in the Appendix B. This model is stationary, no transient studies are included.
The model is comprised of balance and conservation equations describing coupled physical phenomena taking place taking place in a SOC. As the model is set up in a way that allows for both directions of current, SOFC operation can be investigated too. The following physics are accounted for:

- electronic and ionic charge transport
- electrochemistry
- laminar flow in the channels
- diffusion through porous electrodes
- heat transfer

In this chapter a brief description of the modeling approach is provided. First the geometry is described, and afterwards the balance equations are introduced.

3.1 Geometry

The model is a three dimensional representation of a single cell in a stack. The dimensions of the geometry are equivalent to those of a commercially available and experimentally investigated Elcogen cell and are compiled in the Table 3.1. The thickness of each layer was identified by focused ion beam scanning electron microscope measurements and provided in a cell microstructure analysis report.

Table 3.1: The dimensions of the geometry in each direction and the thicknesses of each individual layer

Dimensions	**Value [mm]**		
x direction	18		
y direction	4.44		
z direction	40		
Thickness of each layer			
Layer	**Value [mm]**	**Layer**	**Value [mm]**
Fuel channel	1.2	Contacting net	0.2
FE substrate	0.275	FE functional	0.011
Electrolyte	0.005	GDC barrier	0.002
AE functional	0.015	AE substrate	0.0085
Air channel	0.5	Interconnector	2

An illustration of the geometry is provided in the Figure 3.1. On the left-most a single unit from the geometry is shown. A single unit contains half of the rib width and half of the gas channel width. In the middle a zoomed in picture of the cell assembly allows to see the sequence of the thin layers of the cell. These layers described similarly to Figure 2.2b.
The Figure 3.2 shows how the geometry is developed. As the geometry is repetitive and simple in shape (it consist of purely out of rectangles (2D) or cuboids (3D)), it is important to be able to locate relevant layers. These layers need to be resolved individually, as different physical properties will be assigned to them in the model. The accuracy of the results and computation time are mitigated through a grid convergence index (GCI) study in the Appendix C.

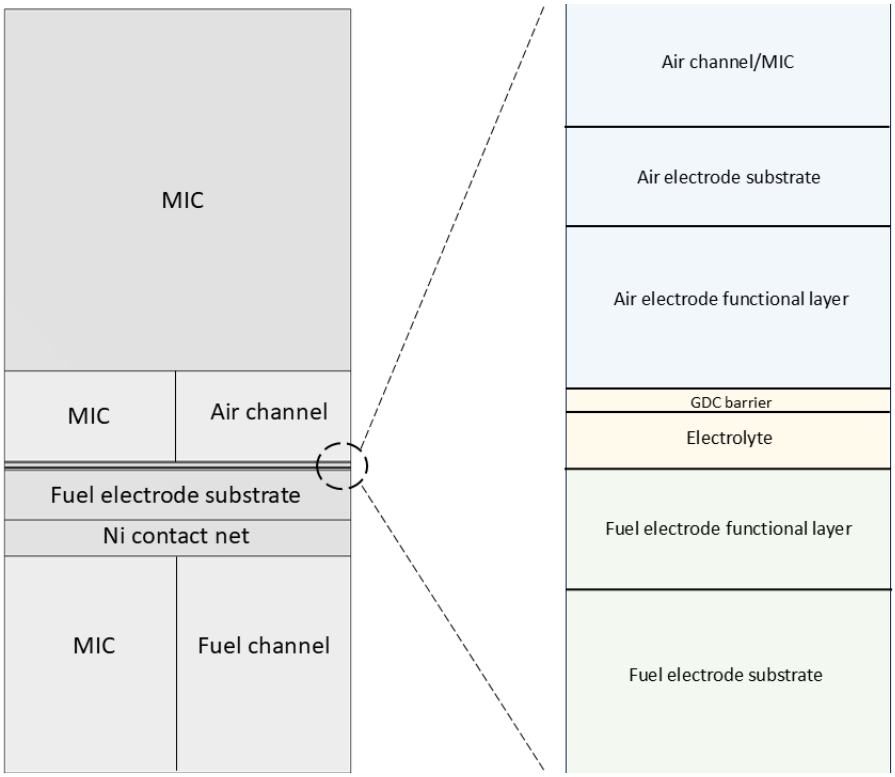

Figure 3.1: Description of the cell layers in the model geometry. A complementary Figure C.3 can be found in the Appendix C.

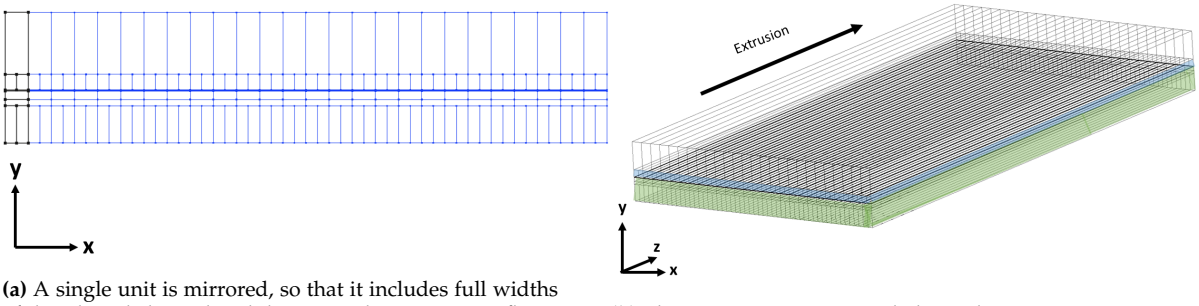

(a) A single unit is mirrored, so that it includes full widths of the rib and channel and then copied 13 times to reflect a symmetrical half of a cell.

(b) The 2D geometry is extruded in z direction to a 3D geometry

Figure 3.2: Explanation of the development of the model geometry

3.2 Scope of the model

This section presents the physical and electrochemical processes included in the model. It covers charge and species transport, electrochemical reactions at the electrodes, and heat transfer within the cell. Together, these phenomena are essential for describing the performance of the cell under any given operating conditions.

3.2.1 Charge transport and transfer

In electrolysis mode, voltage is applied to the cell. The potential difference between both electrodes drives the electrochemical reactions occurring at the electrode-electrolyte interfaces. The reactions involve the transfer of charge (electrons) between the electrode and a chemical species. Charge is transported from the fuel to the air electrode via oxygen ions crossing the electrolyte. An external circuit connects both electrodes and transports charge back as electrons.
The charge transfer current density is calculated with a Butler-Volmer-type Equation 3.1 for each electrode interface separately. It is computing the current at electrode-electrolyte boundaries. The coefficients of the Equation 3.1 can be found in Appendix D. The exchange current densities are denoted as $j_{0,AE/FE}$, charge transfer coefficients are α and activation overpotential as η .

$$j_{ct,AE/FE} = j_0 \cdot \left[exp\left(\frac{\alpha \cdot 2F \cdot \eta_{act}}{RT}\right) - exp\left(\frac{-(1-\alpha) \cdot 2F \cdot \eta_{act}}{RT}\right)\right] \tag{3.1}$$

In a SOC there are two types of currents. An electronic current flows in the electrodes and in the external circuit with electrons as charge carriers. An ionic current flows in the electrolyte and GDC barrier layer, where the charge carriers are oxygen ions. Both types of currents depend on the material's ability to conduct a given charge carrier. For example, YSZ has an excellent ionic conductivity, σ_{ion}, while Ni has outstanding electronic conductivity, σ_{ele}.
Charge transport by conduction is a generalized form of Ohm's law, described by the Equation 3.2. Charge transport equation 3.3 aims to describe the behavior of flow of electric charge carriers due to potential field denoted as **E**. Electric field is calculated as the negative potential gradient, U. The current is contained by a charge conservation equation 3.4.

$$\mathbf{I} = \sigma^{eff}_{ele/ion}\mathbf{E} \tag{3.2}$$

$$\mathbf{E} = -\nabla U \tag{3.3}$$

$$\nabla \mathbf{I} = Q_j \tag{3.4}$$

As the model represents cell in a stack, in the geometry metallic interconnector ribs are present. On the air side, certain amount of voltage is lost, at the contacting points between AE and those contacting ribs. The amount of voltage can be quantified with an overpotential here called η_cont calculated according to 3.5, where A_{cell} is the area of the cell. As can be seen, the magnitude of this overpotential depends on the current density, as higher current will result in more voltage loss.

$$\eta_{cont} = 0.1\,[V \cdot cm^2/A] \cdot j_{y,ele} \tag{3.5}$$

3.2.2 Electrochemistry

The resulting electrical current of the electrochemical reactions is calculated through Butler-Volmer Equation 3.1, as described above. The more moles of H_2 and O_2 are able to react at the electrode-electrolyte boundary the greater is number of released electrons, and thus bigger the charge transfer current. The relation between reacted number of molecules and resulting current is given by Faraday law 3.6, with the number of released electrons per molecule n_e, for

this reaction $n_{e^-} = 2$, and Faraday constant F. Therefore charge transfer current density can be used directly to calculate the molar streams at the electrode-electrolyte boundary.

$$\dot{n}_i = \frac{-j_{ct}}{n_e \cdot F} \tag{3.6}$$

3.2.3 Species transport

This section is divided into four subsections describing different types of approaches to calculate the species transport in the model. To aid with the understanding, figures indicating which domain in the model has a given approach applied is provided.

The transport of species in the cell and cell holder occurs by diffusion and convection. Diffusion dominates in the porous electrodes, while convection is prevalent in the gas channels. The assumptions made for modeling the gas flow are:

- Steady state - there is no time change in the model, meaning no time derivative
- Laminar flow - allows to eliminate any considerations of turbulence and eddies
- Incompressible flow - assumes constant density in continuity equation 3.7
- Ideal gas - enables to freely switch between volumetric and molar flow with $pV = nRT$
- Newtonian fluid - dynamic viscosity remains constant regardless of the shearing

Laminar flow

The above assumptions allow the governing equations for the bulk gas flow to be simplified to a form of the Navier-Stokes equations solved with a continuity equation (Equation 3.7) for momentum balance (Equation 3.8). According to these formulas velocity field variables **u** (flow in x,y and z direction) and pressure p_{ch} are calculated. The boundary conditions (BCs) for laminar flow are shown in the Table 3.2.
In the Equation 3.8 the left side accounts for convective effects, due to fluid motion and the right side accounts for viscous effects within the fluid. This equation is applied in the gas channels and in the Ni contacting domain which is treated as a porous solid, as can be seen in the Figure Figure 3.3. To include the effects that this porosity has on the flow, a modifier, $-\mathbf{u}\left(\mu\kappa^{-1}\right)$, needs to be applied to the momentum equation [1]. That concept is further explained in the paragraph below.

$$\rho\nabla\mathbf{u} = 0 \qquad \text{continuity} \tag{3.7}$$

$$\rho\left(\mathbf{u}\cdot\nabla\mathbf{u}\right) = -\nabla p_{ch} + \nabla\left(\mu\frac{1}{\epsilon}(\nabla\mathbf{u} + (\nabla\mathbf{u})^T)\right) - \mathbf{u}\left(\mu\kappa^{-1}\right) \qquad \text{momentum} \tag{3.8}$$

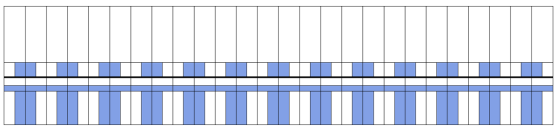

Figure 3.3: The domains highlighted in blue are the ones where laminar flow equations are defined.

Table 3.2: BCs for the laminar flow calculation in the model

Boundary condition	Expression
Inlets	$\dot{m} = \left(p_{atm}\dot{V}_{AE/FE}M_{gas}\right)/RT_0$
Outlets	$\mathbf{u} - (\mathbf{u}\cdot\mathbf{n})\mathbf{n} = 0$ at $p = p_{atm}$
Walls	No slip

Molecular diffusion

In the paragraph above the bulk flow (convection) is described, the gasses flow into gas channels according to the flux defined in the mass flow controller (MFC) or in the model's boundary condition (BC). However, when the entire mass transport of a component in a mixture is considered, besides just convective flow, diffusion also must be included. Diffusion to and from the reaction sites is caused by concentration gradients. Diffusion is a molecular motion, rather than the motion of a whole bulk volume.
Therefore, the combined effect of both convection and diffusion must be solved for in the gas channels [18], to find out the impact of velocity field on concentration gradients. Based on that relationship the model is able to calculate the molar fluxes and changes in them (gas compositions) along the cell.

Convection-diffusion equation describes, how molecules of different species interact with each other on their way through the flow domains (gas channels and Ni contacting). The domains for which convection and diffusion are considered are visible in the Figure 3.4. The convection-diffusion equation according to which the fluxes of molecular diffusion and convection are calculated is shown with the Equation 3.9.
The first term includes the diffusion coefficient, representing diffusion effects. On the fuel side, the fuel can be a mixture of more than two gasses and therefore bulk diffusion coefficient is applied. Bulk diffusion coefficient, D_{bulk}, is calculated through Wilke approach, as shown in Equation 3.10. On the air side, binary diffusion is sufficient as the only gasses present are O_2 and N_2. Binary diffusion coefficients, D_{ik}, are derived from Chapman-Enskog theory, as seen in Equation 3.11. The variables Ω_D and σ_{ik} are collision variables, Ω is the collision integral and σ is the collision diameter. [2]
The second term expresses the impact of convection, caused by the velocity field $\mathbf{u}$ on the concentration field. The vector of concentrations is denoted as $\mathbf{c}$ and contains concentrations of all species relevant for given domain. Source term is denoted as f and equals 0, as no chemical reactions are taking place in the channels
The BCs for molecular diffusion are given in the Table 3.3.

$$\nabla \cdot (-D\nabla \mathbf{c}) + \mathbf{u}\nabla \mathbf{c} = f \tag{3.9}$$

$$D_{bulk} = \frac{1 - x_i}{(x_j/D_{ij}) + (x_k/D_{ik})} \tag{3.10}$$

$$D_{ik} = 1.86 \cdot 10^{-3} \cdot T^{3/2} \cdot \frac{\sqrt{M_i^{-1} + M_k^{-1}}}{p \cdot \sigma_{ik}^2 \cdot \Omega_D} \tag{3.11}$$

Convection and molecular diffusion in Ni contacting layer

That modifier introduced in the Equation 3.8 is Darcian flow modifier, which includes permeability, κ. Permeability is defined with an empirical expression in Equation 3.12 [3].

$$\kappa_{Ni} = 0.15^{2/8} \quad m^2 \tag{3.12}$$

The Ni contacting mesh has lower gas flow resistance vertically (y direction) and higher horizontally (x and z directions). A parameter that quantifies how convoluted the flow path is, is called tortuosity, τ. In x and z direction, $\tau_{x/z} = 2.2$ and in y direction $\tau_y = 1.0$. The volume fractions, ε, of both solid (0.735) and gas (0.265) phases are also different from each other, as reported in [3]. Additionally since this layer is on the fuel side (the fuel can be a mixture of more than two gasses), bulk diffusion coefficients are applied. With the inclusion of tortuosity, τ, and volume fraction, ε, an effective diffusion coefficient is obtained, as seen in the Equation 3.13.

$$D^{eff} = \frac{\varepsilon}{\tau_{x,y,z}} \cdot D_{bulk} \tag{3.13}$$

When parameter is considered 'effective' it means that a homogenization of a porous structure is applied in the model (no explicit modeling of the microstructure geometrically) and to account for an actual amount of volume that is influenced, the parameter is multiplied with the volume fraction, ε, and if the distortion of transport paths is considered then also divided by tortuosity, τ. This way, the diffusion coefficient is only be calculated for the 26.5% of the volume, because only that much is occupied by the gas phase and the rest is a solid Ni contacting mesh, where no diffusion occurs.

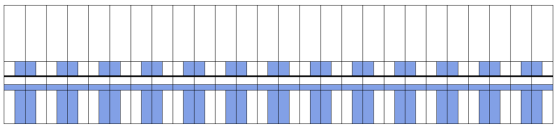

Figure 3.4: The domains highlighted in blue are the ones where convection-diffusion equations are defined.

Table 3.3: BCs for convection-diffusion calculation in the model, the same BCs apply for the upcoming section.

Boundary condition	Expression
AE Inlet	$\mathbf{c} = [c_{O2,0,AE}, c_{N2,0,AE}]$
FE Inlet	$\mathbf{c} = [c_{H2,0,FE}, c_{H2O,0,FE}, c_{N2,0,FE}]$
Outlets	$-nx_{ch} \cdot c_{i,x} - ny_{ch} \cdot c_{i,y} - nz_{ch} \cdot c_{i,z} = 0$

Dusty Gas Model

Molecular diffusion stems purely from molecular collisions. However, where the cross section of the medium in which the molecules are flowing is much smaller than the mean free path of the diffusing molecule wall collisions play the dominant role in loss mechanism.
According to the Knudsen diffusion definition [19], it becomes relevant when distance between the collision of two molecules λ_l exceeds pore diameter d_p. In the porous electrodes the pores of

the microstructure are sufficiently small $(200\text{nm} - 1.2\mu\text{mon average})$ to raise a concern if Knudsen diffusion plays a role in the overall diffusion.
To quantify the influence of wall collisions Knudsen number K_n can be calculated, and according to [2] for a similar cell it finds itself in the transitional region, where neither type of diffusion dominates and therefore both need to be considered. For that purpose multi-component porous media gas transport model called Dusty-gas model (DGM) is used. It is commonly used in literature to describe species transport in the porous electrode for the SOC models [8]. The domains where that model is used are visible in the Figure 3.5

DGM is based on Maxwell-Stefan diffusion equations. It is inspired by the idea of molecular and Knudsen fluxes flowing simultaneously with regard to viscous flow, but additionally introduces a pseudo species - thus 'Dusty gas' - that represent the solid phase. The particles of those species are assumed to be giant dust molecules with infinite mass, uniformly distributed in the domain and held in place by an unspecified external force. The molar based balance equation for this model is shown with Equation 3.14. DGM is used in the model in a matrix form. First, diffusion coefficients are calculated for each possible diffusion combination (binary, molecular, Knudsen). Then one Equation 3.14 is solved for each species i and the result is a molecular flux of the i species in x and y direction separately. [1]

$$\sum_{\substack{k=1 \\ k\neq i}}^{n} \frac{x_k \vec{n}_i - x_i \vec{n}_k}{D_{ik}^{\text{eff}}} - \frac{\vec{n}_i}{D_{Kn,i}^{\text{eff}}} = -\left[\nabla c_i + x_i \frac{\kappa_0 p}{\mu_{\text{el}}} \frac{1}{D_{Kn,i}^{\text{eff}}} \nabla c\right] \tag{3.14}$$

The molar fluxes are denoted with $\vec{n}$ and the subscript indicates which species is addressed. Effective bulk diffusion coefficient is D^{eff}. The coefficient is effective, because the approach to porous electrodes is the same as to the Ni contacting, as explained by the Equation 3.13. For each domain of the electrodes, tortuosity and volume fractions are defined and can be found in the Appendix E. On the right side of the equation in the Knudsen term, κ_0 denotes permeability in a given domain, which for the porous electrodes is defined with the Equation 3.15. In this equation z_{ch} is the thickness of the electrode layer that can be found in the table Table 3.1. Knudsen diffusion coefficients are calculated based on the Equation 3.16, where d_{por} is the diameter a pore and M_i is the molar mass of species i.

$$\kappa_{ch} = \left(\frac{z_{ch}}{2}\right)^{2/8} \tag{3.15}$$

$$D_{Kn,i} = \frac{2}{3} d_{\text{por}} \sqrt{\frac{8RT_k}{\pi M_i}} \tag{3.16}$$

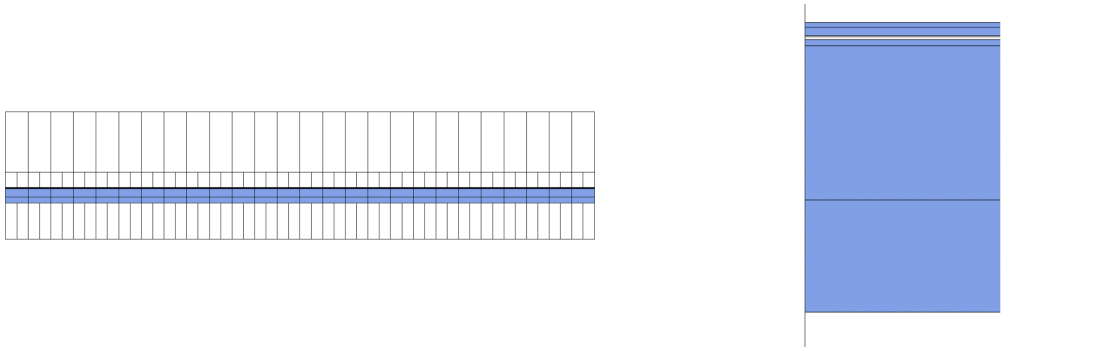

(a) Overview of the whole cell with highlighted domains

(b) Zoom in on the highlighted domains

Figure 3.5: The domains highlighted in blue are the ones where DGM is defined.

3.2.4 Heat Transfer

Depending on operation the reversible electrochemical reaction in the cell is either exothermic (FC) or endothermic (EC), therefore differences in the temperature profile along the cells are expected between both operation modes. At thermoneutral voltage (TNV) (ok. 1.3V) in EC mode minimal temperature change is expected and above it actually a temperature increase rather than decrease. In both operation modes some amount of heat is also generated due to current flowing through the cell or loss due to insufficient insulation, causing irreversible energy losses.

To determine the spatial temperature distribution, the energy balance for the stationary state is implemented with the Equation 3.17. The first term in this equation describes convective heat transport, which is the main heat transport mechanism in the flow channels domains. The second term is conductive heat transport and is influenced by the thermal conductivity of each material. The heat is transferred through each material, without velocity contribution from the flowing gasses. On the right hand side of the equations all heat sources and sinks are found.

$$\rho C_p \mathbf{u} \cdot \nabla T + \nabla \cdot (k \nabla T) = Q_{ohm} + Q_{contact} + Q_{reaction} + Q_{act} \tag{3.17}$$

Ohmic heat, Q_{ohm}, is generated through the flow of ionic current in the electrolyte and GDC barrier. It is calculated according to the Equation 3.18. Denoted by I_y is the ionic current in the y direction (normal to electrolyte-electrode interface), which corresponds to j_{ct}. The ionic conductivity of the electrolyte or barrier layer materials is σ_{ion}. Only these two domains conduct the ionic current. Heating from electronic conductivity is negligible in this SOC model, as the electronic conducting materials have sufficiently high electronic conductivities not to generate overabundance of heat. The difference between the heat generated through ohmic and electronic current has magnitude of four orders difference.

$$Q_{ohm} = \frac{I_{y,ion}^2}{\sigma_{ion}} \tag{3.18}$$

Heat generated by contact resistance is located between the contacting ribs on the air side and the air electrode. It stems from unideal contacting in the real cell, in the model it is accounted for with an current dependent Equation 3.19

$$Q_{contact} = \frac{0.1[V \cdot cm^2/A]}{I_{y,ele}^2} \tag{3.19}$$

Through the reversible electrochemical reaction occurring at the electrode-electrolyte boundaries, heat is either generated (FC mode) or consumed (EC mode). This thermal effect is referred to as the reversible heat of the electrochemical reaction and is calculated using Equation 3.20. The sign and magnitude of this heat depend on the total entropy change of the reaction, ΔS_{tot}. If $\Delta S_{\text{tot}} > 0$, the reaction is endothermic, meaning that heat is absorbed from the surroundings, resulting in $Q_{\text{reaction}} < 0$. Conversely, if $\Delta S_{\text{tot}} < 0$, the reaction is exothermic, and heat is released, i.e., $Q_{\text{reaction}} > 0$. In EC mode, the overall reaction is always endothermic. The total reaction entropy, ΔS_{tot}, is defined in Equation D.9 in Appendix D.

$$Q_{reaction} = \frac{-\Delta S_{tot} \cdot T \cdot j_{ct,AE}}{2F} \tag{3.20}$$

To calculate the amount of irreversible heat losses stemming from activation overpotential the Equations 3.21,3.22 are calculated for each electrode separately. Charge transfer current density is calculated with equation 3.1, activation overpotentials $\eta_{act,AE}$, $\eta_{act,FE}$ are calculated with equations D.4, D.3. These equations can be found in the Appendix D.

$$Q_{act,AE} = |\eta_{act,AE} \cdot j_{ct,AE}| \tag{3.21}$$

$$Q_{act,FE} = |\eta_{act,FE} \cdot j_{ct,FE}| \tag{3.22}$$

Chapter 4

Experimental Setup

In this chapter an explanation of the experimental setup including measurement devices, testing rig and the investigated operating conditions are given. In Figure 4.1 a schematic of it is shown.

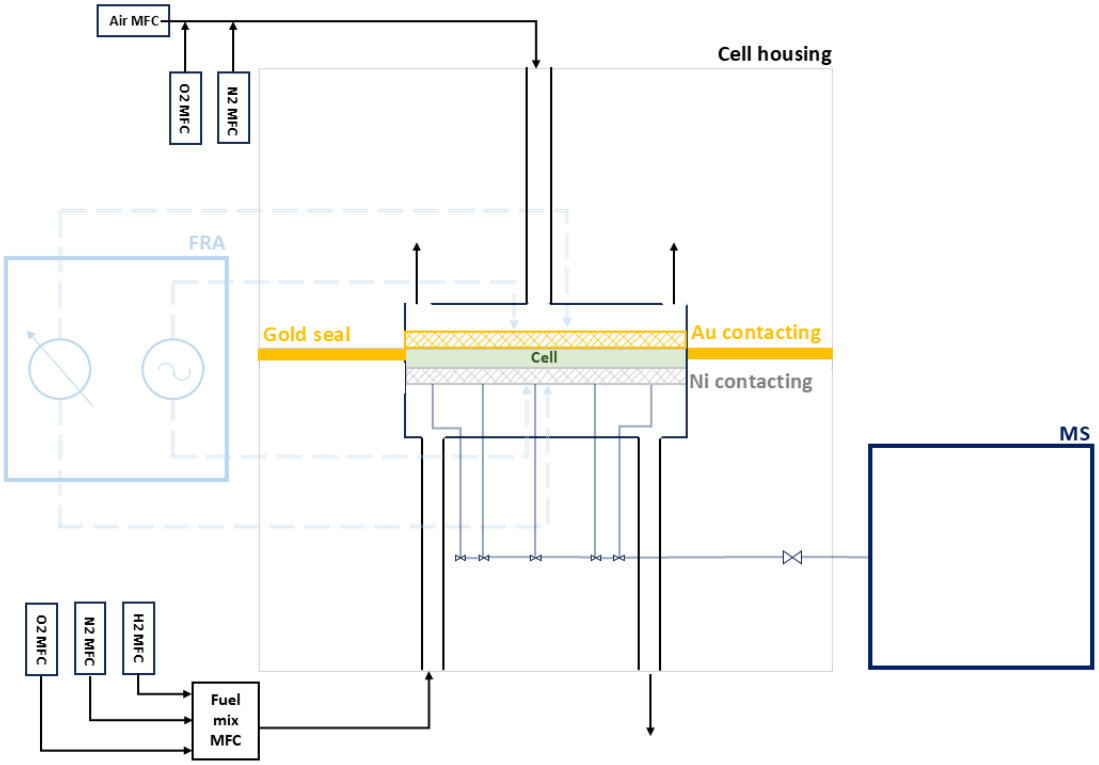

Figure 4.1: Illustration of the experimental set up inside the testing rig - ceramic cell housing indicated with gray dashed lines, FRA and potentiostat in pale blue and **mass spectrometer** with measurement probes in dark blue. Mass flow controllers for the gas supply of fuel and air electrode, as well as inlet and outlet are shown in black. The gold seal is on the sides of the cell. The cell contacting is shown with golden colored gold contacting mesh on the air side and light gray nickel contacting mesh on the fuel side. The cell is marked in green.

The investigated cell is manufactured by Elcogen and has an active area of $16cm^2$. The single cell is mounted in a ceramic cell housing. The substrate of the fuel electrode is contacted with a Ni mesh, which additionally ensures both an even gas distribution and electrical contacting. The air electrode is contacted with an Au mesh to achieve almost ideal contacting [1]. Fuel and air gas chambers are separated by a gold seal [14].

The housing is placed in an insulated oven inside a FuelCon Evaluator-C testing bench. The gasses are supplied from gas tanks and the flow is regulated by mass flow controllers (MFCs). One thermocouple is placed at the cell surface and another one in the oven space, which allows to control temperature.
The cell is connected by gold cables to frequency response analyzer (FRA) Zahner Zennium X and potentiostatic/current range extender PP 241, with which electrochemical measurements are taken (EIS and *I/U* curves as follows). Each cable is encased with ceramic beads to prevent an accidental short circuit. The cables are twisted around each other to cancel out inductance interactions between them [14].
Mass spectrometer Hiden Analytical, model HDR-20 R&D is used. It is a quadrupole spectrometer configured for continuous analysis of gases and vapors at pressures near atmosphere [20]. In this investigation, mass spectrometry allows to quantitatively analyze the composition of fuel gasses along the cell at five different points, allowing to determine gas conversion along the cell during operation. This will allow to calculate gas conversion along the cell and then from that the current density for those sections. The software of the gas spectrometer QGA 2 produces a continuously updated plot showing gas composition in percentages (based on partial pressures) of the species in the fuel gasses. The gas composition on the reacquired plot can be compared with the expected one.

In the Figure 4.2, the placement of the measurement positions (a) along the cell and (b) in the cell housing from the bottom is shown.
Each probe has a thermocouple inserted to be able to measure the temperature and to identify possible leakages of oxygen (from the air) to the cell housing.

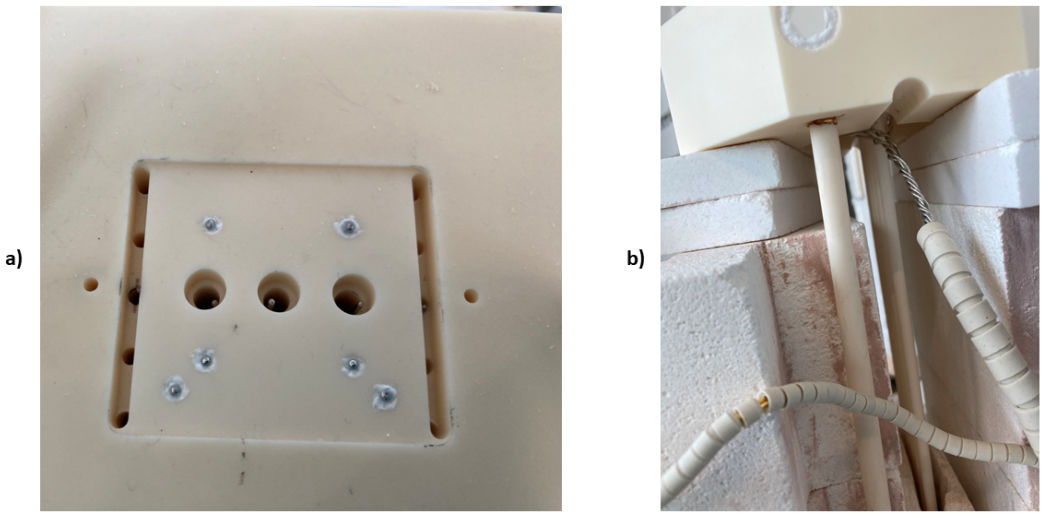

Figure 4.2: Cell holder setup for gas composition measurement showing (a) the placement of gas conversion measurement probes along the cell and (b) shows where the tubes are placed in the ceramic housing

Mass Spectrometry

MS is based on analyzing the mass-to-charge ratio of gaseous ions, a more in depth presentation of MS components as well as more detailed explanation of the working principle can be found in the Appendix A.
The ionizer converts the sampled analyte into gaseous ions. The analyte can undergo soft ionization or hard ionization. During soft ionization the compounds are not completely fragmented, but rather gently charged by ejecting an electron. This is done by adjusting the ionization energy for a particular mass.
The mass analyzer is able to determine the motion paths of the ions in magnetic and electric field based on their mass-to-charge ratio (m/Q), according to Lorentz force law and Newton's second law of motion. Any ions entering the analyzer field experience potential differences deflecting them from their theoretically predicted trajectory. The extent of deflection is related to its m/Q.
The detector records induced electric interaction when an ion approaches its surface. Then it converts this interaction into a specific electrical signal for each m/Q. The instrument records this signal and mass spectrum is created by plotting signal intensity (ion count) against m/Q [21].

In the Figure 4.3a a typical mass spectrum for air from [20] is shown. The molecules are recognized by the peak with the highest intensity and their corresponding molar mass. That type of result output is called a mass spectrum and is well suited for compound identification, however in the case of this project the compounds in the gas mixtures are already known.
The MS software QGA 2 offers a different type of results display, where partial pressures profiles of measured species are plotted overtime. It can be seen in the Figure 4.3b, and is used because the gas composition is known and the point of interest are the ratios (percentages/fraction) of the species.
To use that mode, first a so-called background scan to needs to be performed, to detect noise from the mass spectrometer itself. For all species pure gas needs to be fed to the spectrometer, for example 100% N_2. In that case the expected measurement would be 100% N_2 and no other gas should be present. In reality small amounts of other gasses are also detectable. Measuring the presence of other gasses allows to subtract the measured amount as noise in future measurements to avoid skewing results.
After the background scan, calibration scans for each gas mixture anticipated in the future scans, relative to a gas that has the highest partial pressure in the investigated mixtures, are conducted. That is to tune relative sensitivity. An expected gas composition is given and compared with the final measurement result. A calibration factor (a correction factor) is then calculated by the software and all future measurements with a chosen relative gas are multiplied with it.

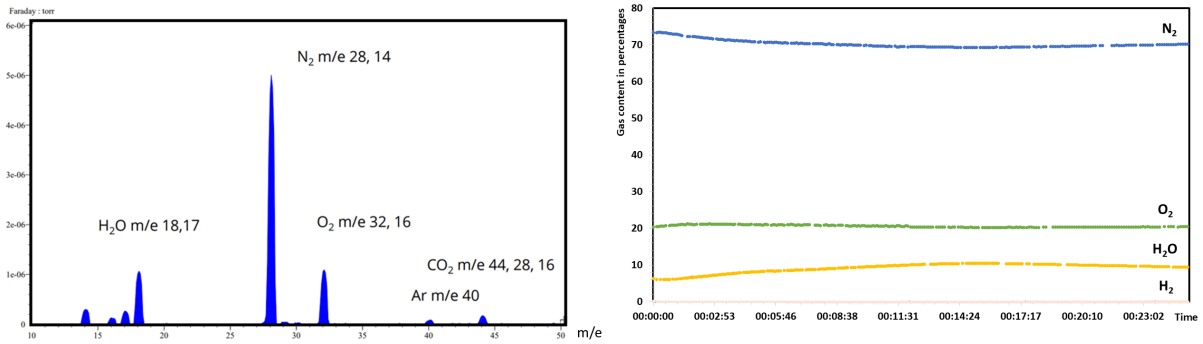

(a) Mass spectrum of air from Hidden Analytics [20]

(b) Profile of the measured composition of air over time

Figure 4.3: Comparison of the two ways of displaying MS results

4.1 Measurement techniques

The measurement procedure for the cell is carried out using the Fuel Work and Test Work software, which manages the pre-defined measurement protocol, controls the testbench and calls the Zahner software to perform electrochemical measurements as detailed in the section 4.1.1. In the Table 4.1 operating conditions are given.

Table 4.1: Measurement conditions

Parameter	Value
Active area of the cell	$16.1 cm^2$
Pressure	$1 atm$
Temperature	$700°C$
Volumetric flow on the air side	$1400\, ml/min$
Volumetric flow on the fuel side	$193 - 660\, ml/min$
Current EC mode/FC mode	$-1 A/cm^2$ / $1 A/cm^2$

The EIS measurements are taken in a galvanostatic operation, with a current amplitude that results in an amplitude of $30mV \cdot A_{cell}$. Galvanostatic operation means that a current value is set and voltage amplitude is registered as a response signal. EIS settings are compiled in the Table 4.2. The integration time determines how long data is recorded for each data point. The longer the integration time, the less noise. The total integration time is the time needed to record the whole spectrum. Number of periods is the amount of full response oscillations measured at each measured frequency. Points per decade are the number of frequency points measured within one decade (for example one decade: $1Hz \rightarrow 10Hz$, a tenfold increase in frequency).

Table 4.2: Settings for EIS. The difference between the parameters in low and high frequencies stems from the significant difference in orders of magnitude of the signal frequency. Low frequencies use less points per decade to reduce the total integration time, because one period already takes longer to record. But more periods are used to improve the measurement quality.

Parameter	Value
Frequency range	$100mHz - 0.1MHz$
Integration time	10 sec
Number of periods low frequencies/high frequencies	30/15
Points per decade low frequencies/high frequencies	8/15

4.1.1 Measurement protocol

The control of the experiment is scripted with Fuel Work. It allows to operate the test bench and call the FRA Zahner software to conduct measurements. The cell is operated according to Elcogen Solid Oxide Fuel Cell User Manual [22].

At first, total flows are defined at fuel and air side. On the fuel side the maximum flow of the gas composition is $660ml/min$, on the air side it is $1400ml/min$, however later on during gas variations these flows are adjusted. Before coming in contact in the cell, the gasses are preheated to avoid thermal shock. To the oxygen side air is supplied, while the fuel side is supplied with safety gas with composition of $5\%H_2$ and $95\%N_2$. In those conditions a gradual heat up to 700°C begins. Once this cell temperature is reached, the cell is left for a six hour wait time to seal the fuel and air atmospheres separate from each other.
After sealing, cell reduction is started. To reduce NiO of the fuel electrode to electron conducting Ni the flow of hydrogen is gradually increased, from the concentration of 10% all the way up to 100% in two hour increments.
At a fuel gas composition of $100\%H_2$ the OCV is recorded. The cell is considered stable and the reduction complete, when the OCV variation is not greater than $+/-5mV/3h$. Afterwards, gas or temperature variation for cell characterization are conducted. For this study gas composition variations are conducted at temperatures of $600°C$, $650°C$ and $700°C$. Once all the results are recorded, a shut down procedure is initiated. It entails the re-opening of safety gas valve to avoid reoxidation of Ni and shut off of the fuel gasses as well as cell cool down.

Chapter 5

Results and discussion

This chapter presents the results obtained from the experiments and the model, focusing on validation, TNV operation and overpotentials distribution.
The first sections compare experimental measurements with simulation results to assess the validity of the model, including I/U curves, gas composition analysis, and electrochemical impedance spectroscopy. This is followed by model-based investigations under thermoneutral conditions, offering a detailed view of the spatial changes of overpotentials, heat sources, and current density in the cell.

5.1 Model validation

In order to prove that the model's results are in line with experimental cases, a validation with experimental data is conducted. For the comparison, model results are plotted against experimental data measured for single cell.
First, the results of gas conversion are compared, then the experimental I/U curves and lastly results from EIS measurements are analyzed, fitted and resistances from this experimental data are compared with the ones simulated in the model.

5.1.1 Gas composition and utilization

To gain insight into this cell's gas conversion and verify model predictions, gas composition measurements on the fuel side are performed using a MS. This section outlines the model results, experimental setup, challenges encountered, particularly related to water condensation and gas leakage, and the methods used to obtain reliable gas composition data under given operating conditions.

Gas composition along the cell in the model

In the model, the gas species along the length of the cell can be plotted. The distribution of each species and their molar fraction is heavily dependent on the operating conditions. In Table 5.1 the set operating conditions are shown. These are the default operating conditions for electrolysis mode in the model and one of the operating points for the low volumetric flows for the experimentally investigated cell.
In electrolysis mode, the electrochemical reaction of splitting steam takes place. In Figure 5.1,

the cell is fed a highly humidified gas mixture of H_2O and H_2. Along the cell, the H_2O concentration decreases, while on the fuel side H_2 and O_2 on the air side increase.

Table 5.1: Operating conditions in the cell model

Parameter	Value
Active area of the cell	16.1 cm^2
Temperature	700°C
Pressure	1 atm
Volume flow fuel side	193 ml/min / 2 = 96.6 ml/min
Volume flow air side	96.6 ml/min · 2 = 238 ml/min
Inlet gas composition fuel side	x_{H_2O} = 0.9, x_{H_2} = 0.1
Inlet gas composition air side	Air
Operation	Potentiostatic
Operating voltage	TNV = 1.2725 V

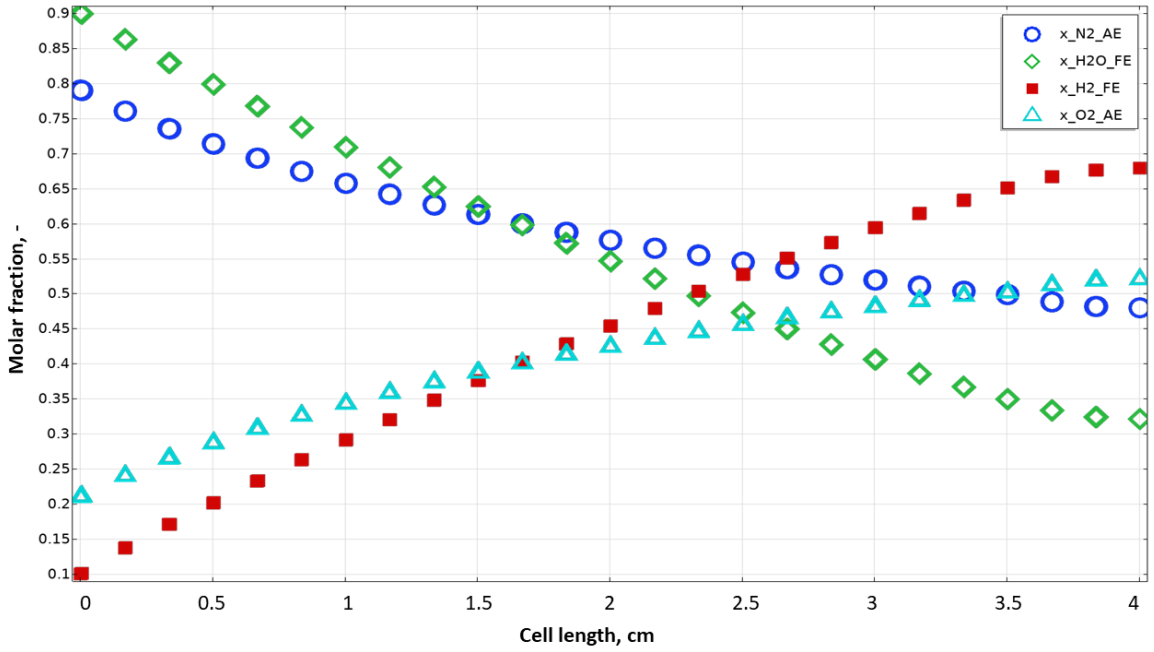

Figure 5.1: Molar fractions in the gas channels along the length of the cell are changing as the reaction progresses. In EC mode (shown here), the content of H_2O on the fuel side diminished (green curve), while the H_2 increases (red curve). On the air side, more O_2 appears (light blue curve), as a result of the reaction. Plot generated in COMSOL.

Mass spectrometer measurement setup

Gas composition in the cell can be monitored using MS, which is implemented into the test bench setup, as introduced in Chapter 4. While the inlet gas composition on both the fuel and air sides is set via the testbench software and mass flow controllers, the gas composition along the length of the cell and at the outlet remains unknown. Gaining insight into this spatial variation is of particular interest, as it enables the determination of local fuel conversion in the cell and provides a more accurate estimate of the electrochemical reaction's progress.

The initially used five-point measurement cell holder was found to be excessively leaky, making it impossible to get reliable measurement data. Unfortunately, the necessary modifications to improve gas tightness would require significant time and were thus considered beyond the scope of this project.
Despite this limitation, it remains relevant to investigate overall fuel utilization in the cell by comparing the gas composition at the outlet with model predictions, thus demonstrating viability of the method. Consequently, the five-point holder was replaced with a standard cell holder (without the modification of five measurement points), and measurements were taken at the fuel outlet. The new setup is shown in the Figure 5.2, with the Figure 5.2a depicting the insulated oven and the cell holder and Figure 5.2b illustrating the connection between the testbench and MS.

A practical issue arose with the layout of the fuel exhaust. The ceramic outlet from the cell leads upwards, out the oven and initially before descending, ran unheated parallel to the oven. This did not fully prevent condensation of water droplets and water accumulation in the exhaust line. These droplet were sucked into the MS line, as the spectrometer operates slightly under the atmospheric pressure. Although the capillary line to the MS is heated to prevent condensation, the heating is insufficient to evaporate pre-formed water droplets. This led to noise in MS data and pressure fluctuations.
To alleviate this problem, the fuel line was directed downwards right after exiting the oven, instead of going parallel. The MS line is connected via a three-way swagelok part with a valve and tilted upwards from the fuel exhaust line, so that it is less likely for the droplets to follow the path to the MS.

(a) Cell holder in the oven with a mounted cell. **(b)** Fuel outlet and the new measuring point for the MS

Figure 5.2: Changed experimental setup

For accurate MS measurements, calibration of the spectrometer at a given pressure is required. This allows to compensate for background noise signals. It is done by measuring at 100% concentration of each gas at the supply lines, to avoid cell holder influences, and subtracting the measured presence of any other gas. Then, for each gas mixture, correction factors are determined. They are measured with a dummy-cell mounted in the testbench. For each mixture a relative gas is chosen, it is the gas that has the highest concentration in a given mixture. Based on the expected gas composition relative to the chosen gas and measured gas composition correction factors are calculated. A protocol according to which the calibration is carried out is attached in the Appendix A, in the Figure A.3.

Despite the described improvements, the setup remains unsuitable for measurements involving high humidity gas compositions (above 35% water content), as water still tends to accumulate in the outlet. Therefore, reliable data can currently only be obtained under low-humidity operating conditions more suitable for FC mode, as shown in the following section.

Mass spectrometer results

To collect the data, a known gas composition is set at the inlet either under OCV conditions or for galvanostatic operation (with a defined current density) and the corresponding outlet composition is recorded.
In the first test, the gas composition is set to 10% H_2O and 90% H_2 for the low volumetric flow of H_2 = 193 ml/min and O_2 = 9 ml/min. The data is collected for the OCV and four current loads and plotted in the Figure 5.3.

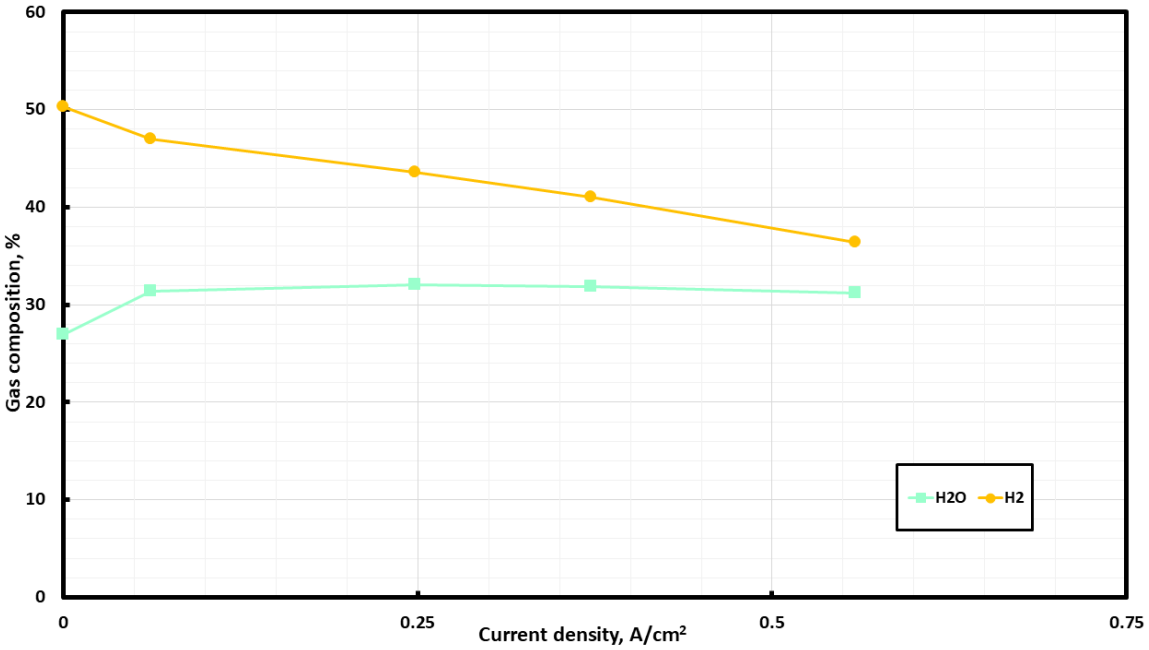

Figure 5.3: H_2 and H_2O fractions in the gas composition at the fuel outlet measured by MS with increasing current density load. Flows: H_2 = 193 ml and O_2 = 9 ml

The expected outlet gas composition at OCV (current density = 0 A/cm^2) is 10% H_2O and 90% H_2. On the plot however this is not the case, at 0 A/cm^2 the gas composition equals to 27% H_2O and 51% H_2. The measured OCV is read as OCV = 1.01 V. From this OCV it is possible to calculate back to p_{H_2O} using Nernst voltage Equation 2.3. From the Nernst voltage equation, the water content is in almost perfect agreement with the one measured by MS. The results is 29% H_2O. This means that currently the cell has some amount of air leaking into the set up. The oxygen from air is reacting with the excess hydrogen, creating additional steam.

The amount of leakage can be estimated with a stochiometric calculation (Equation 5.1), by looking at the volumetric flows and gas composition. In the equation, x is the unknown amount of oxygen leakage. Assuming air composition of 79% N_2 and 21% O_2 the amount of unwanted

air getting into the system is 88.6 ml, from which 18.6 ml is O_2 and 69.9 ml is N_2.

$$\frac{9\,ml + x}{193\,ml + x} = 29\% \tag{5.1}$$

This leaves one more unexplained issue with the plot. According to the Equation 3.6 the more current is delivered to the cell, the more moles should take part in the electrochemical reaction. This is independent of the cell performance. A worse performing cell also abides this dependency, it will just need more driving force (overpotential) to achieve the same conversion.
According to this, the slope of the plot should be constant and the dependency itself linear. This is not what is seen on the plot. The reason for this is the setup's weak ability to measure in humidities above 35%. Above this level, droplets start forming in the outlet making the gas measurement unreliable.

To be able to check this hypothesis volumetric flows on the fuel side are increased, so that gas composition can be measured in even higher loads. The gas composition at the inlet remains the same, but the flows now are: H_2 = 400 ml/min and O_2 = 20 ml/min. The result of this test are plotted in Figure 5.4.
As expected the water content profile plateaus around 35%, further some water droplets start appearing in the measurement. The leakage calculated from OCV = 1.03 V is the same as the leakage calculated in the previous test, further solidifying the suspicion that the MS in this setup is unable to measure in higher humidification.

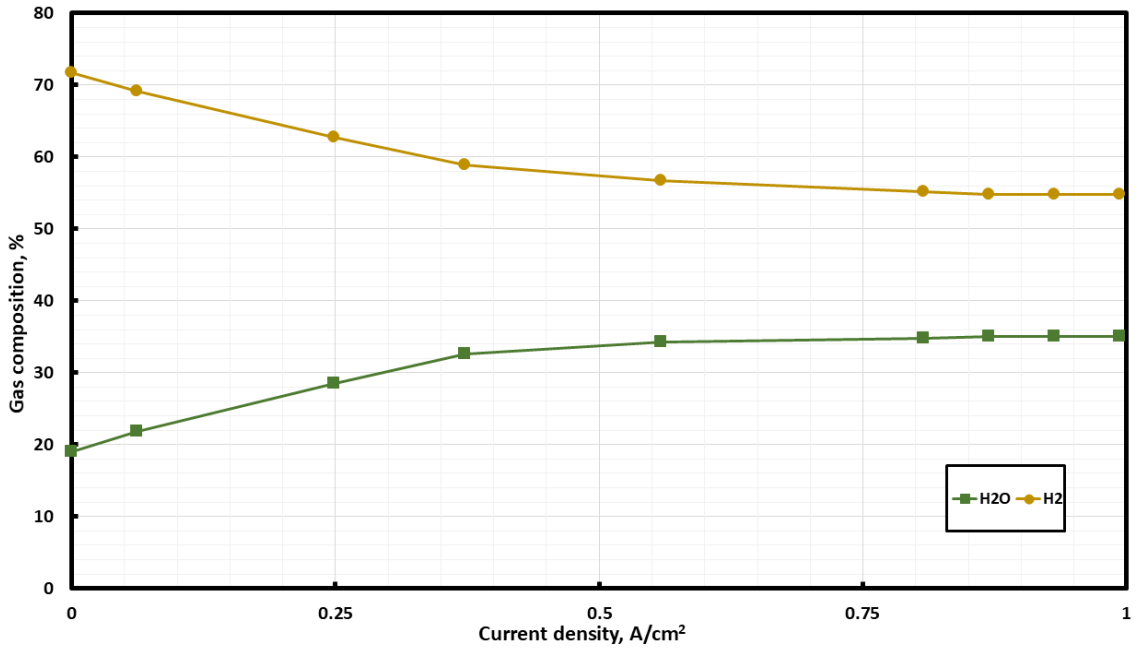

Figure 5.4: H_2 and H_2O fractions in the gas composition at the fuel outlet measured my MS. Flows: H_2 = 400 ml/min and O_2 = 20 ml/min

One more test was conducted at even higher flow, however at that flow, the influence of load on gas conversion is barely a fraction of a percent. Instead it is more interesting to see the theoretical slopes for this middle flow, shown in Figure 5.4. Using the Equation 3.6, repeated below for convenience and clarity, for each load it is possible to calculate the number of moles that will

react under that load, and based on that obtain the gas composition.

$$\dot{n}_i = \frac{-j_{ct}}{n_{e^-} \cdot F} \tag{5.2}$$

The results of the calculation are shown in the Figure 5.5 with dashed lines. For loads under 0.5 A/cm^2 the theoretical and experimentally measured gas compositions have similar slopes. For the hydrogen measurement even the values of gas composition align, both lines laying of top of each other. However, at loads above 0.5 A/cm^2 for which steam content exceeds or nears 35%, the alignment falls short. As expected, the measured lines are staying constant, as this is the limit which can be currently measured, while theoretical lines are continuing on the same trajectories.

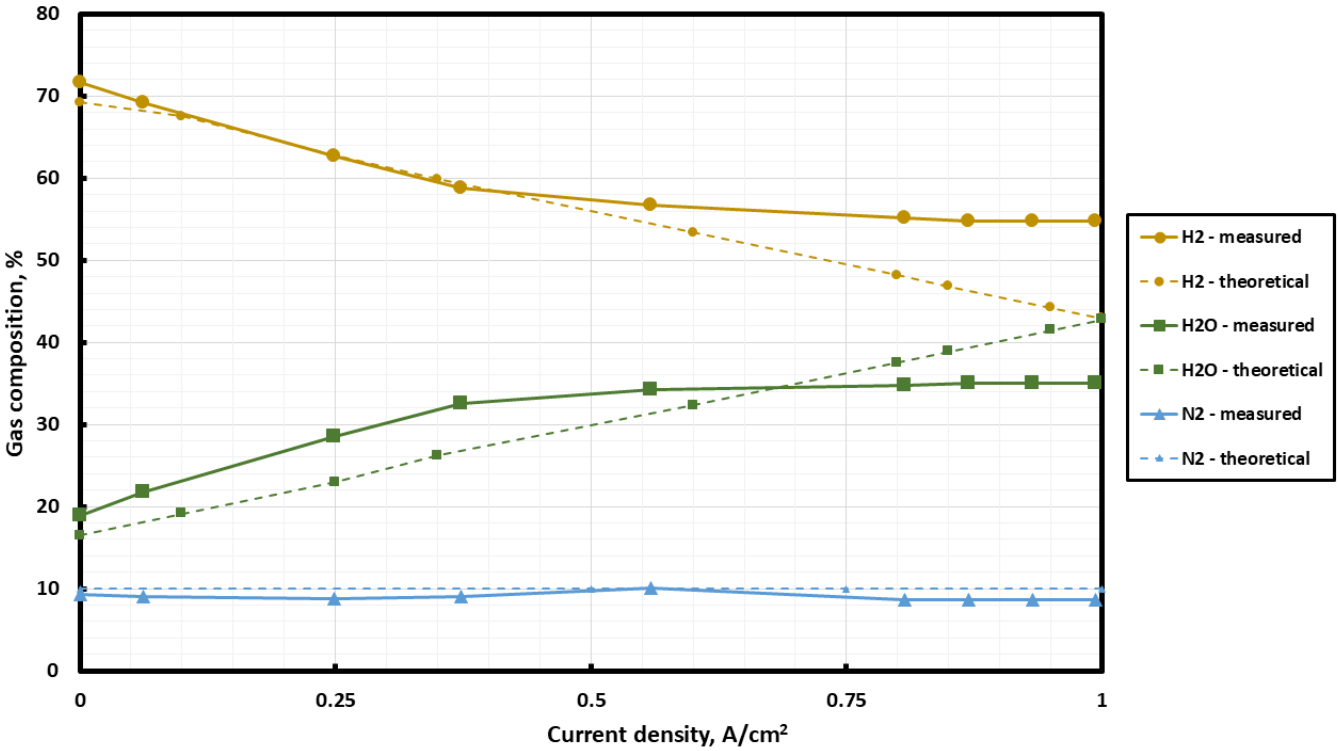

Figure 5.5: H_2 and H_2O fractions in the gas composition at the fuel outlet measured by MS and calculated theoretically. Flows: H_2 = 400 ml/min and O_2 = 20 ml/min and additionally accounted 88.6 ml of air leakage.

Comparison with model results

The COMSOL model also simulates fuel cell mode operation under galvanostatic conditions. For each current load, the model provides the outlet gas composition, which is calculated as the average molar fraction of each species across all outlet boundaries. The results are shown in Figure 5.6 alongside the measured and theoretical data.

The model captures the expected trend: with increasing current density, the hydrogen content in the outlet gas decreases while the steam content increases. However, the slopes for both H_2 and H_2O are steeper in the model than in the experimental and theoretical results, indicating that the model slightly overestimates gas conversion under the given operating conditions. For

hydrogen, the deviation between model and theoretical values is approximately 4%, while for steam it is around 10%.
Unlike the experimental setup, the model also cannot operate at OCV, so the comparison starts from the first current load.

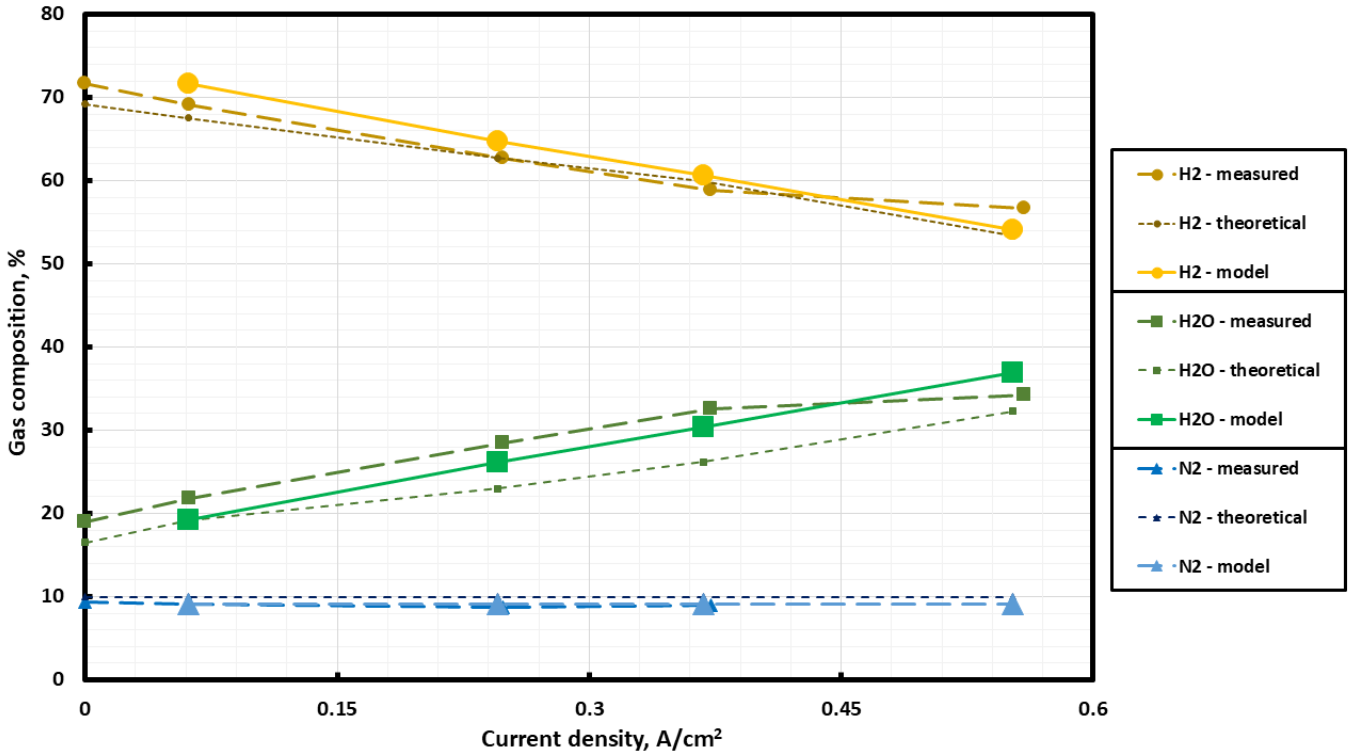

Figure 5.6: H_2 and H_2O fractions in the gas composition at the fuel outlet measured by MS and calculated theoretically compared to the results form the COMSOL model. Flows: H_2 = 400 ml/min and O_2 = 20 ml/min and additionally accounted 18.6 ml/min of oxygen leakage. The relative errors between dataset are plotted in Figure C.12

To further quantify the level of electrochemical conversion, gas conversion for hydrogen and steam is calculated. It is defined as the ratio of moles reacted to moles supplied, based on Equation 5.3. The results of this calculation are summarized in the Table 5.2.

$$X_i = \frac{n_{i,\text{in}} - n_{i,\text{out}}}{n_{i,\text{in}}} \tag{5.3}$$

Table 5.2: Calculated gas conversion for H_2 and H_2O at different current densities, based on experimental, theoretical, and model results.

J_{op} (A/cm^2)	EXPERIMENTAL		THEORETICAL		MODEL	
	H_2	H_2O	H_2	H_2O	H_2	H_2O
0.00	0.00	0.00	0.00	0.00	–	–
0.06	0.04	-0.32	0.02	-0.16	0.04	-0.17
0.25	0.09	-0.72	0.09	-0.39	0.16	-0.66
0.37	0.15	-0.97	0.13	-0.58	0.24	-0.99
0.55	0.18	-1.07	0.23	-0.95	0.33	-1.38

The gas conversion values derived from the experiment, theory, and model are all in close agreement at lower current densities, where steam content stays is below 35%. At higher loads, deviations appear primarily due to measurement limitations and model simplifications. Still, the overall alignment confirms that the model realistically reproduces the gas-phase behavior under fuel cell mode operation with leakage included.

5.1.2 *I/U* curves

To validate the developed model for this project, *I/U* curves obtained experimentally are compared to simulated data under two distinct operating regimes with vastly different inlet gas compositions on the fuel side. In both cases, the fuel side flow is fixed at 193 ml/min and the air side flow at 1400 ml/min. For the operation with fuel side inlet composition of 90% H_2O and 10% H_2 the name 'EC operating points' is used. For the second case with lower humidification, e.g fuel side inlet composition of 10% H_2O and 90% H_2, the name 'FC operating points' is used. The validation results are shown in Figure 5.7 for EC operating point and in Figure 5.8 for FC operating point.

The experimental data in both modes display the expected behavior of solid oxide cells, characterized by activation losses at low current densities, ohmic losses across across the full range, and concentration overpotentials becoming significant at higher current densities. The model reproduces the general shape and slope of the experimental *I/U* curves accurately, indicating that the fundamental physics are well captured. Nevertheless, the model does not converge across the entire voltage range for all operating points, particularly under FC conditions.

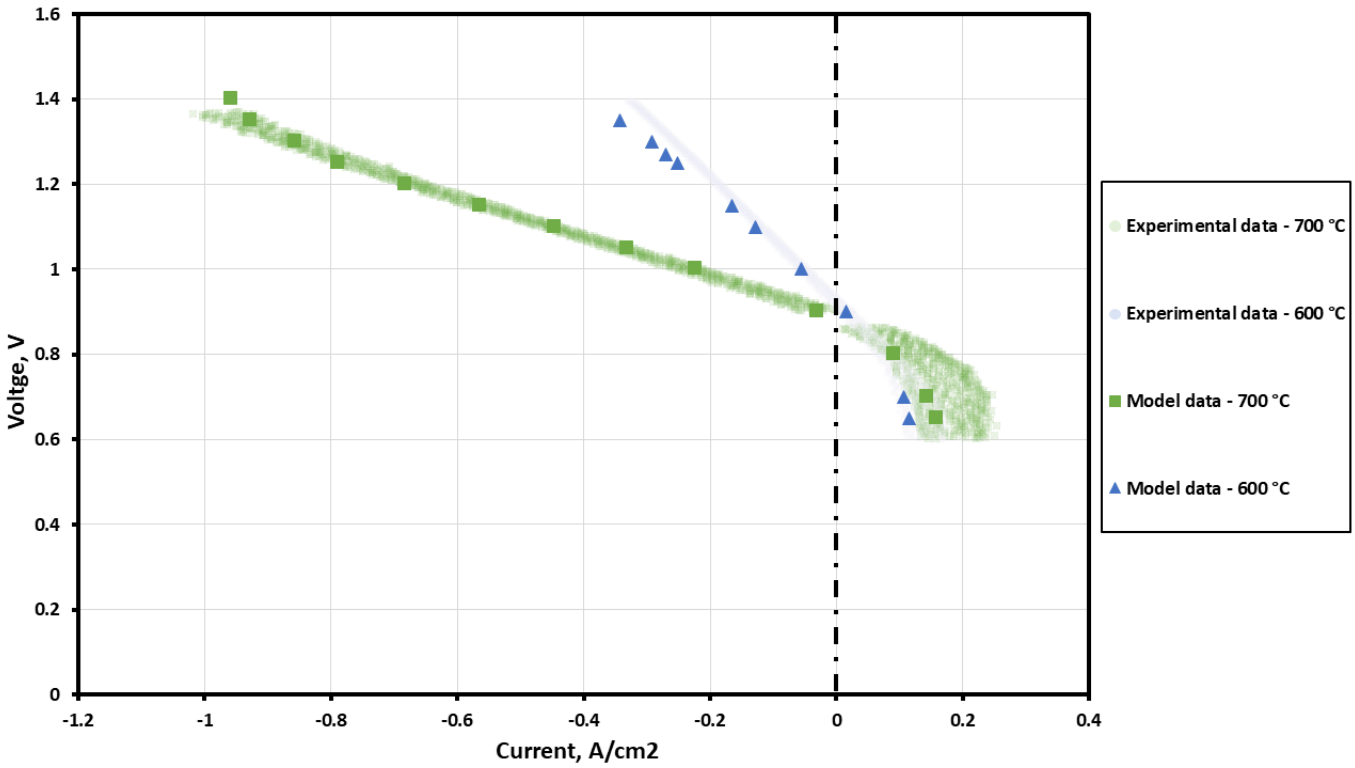

Figure 5.7: *I/U* curve of the experimental and model measurements. The operating conditions for this measurement are the default settings descried in Table Table 5.1, with inlet gas composition on the fuel side of 90% H_2O and 10% H_2. These high humidification conditions are described as **'EC operating points'**.

For EC operating points in the Figure 5.7 the model generally agrees well with the experimental data. The largest deviation is observed at higher current densities, where the model overestimates the cell performance. This tendency is more pronounced in the lower temperature of 600° C, which could be happening due to excess heating in the model, which ´boosts the predicted performance.

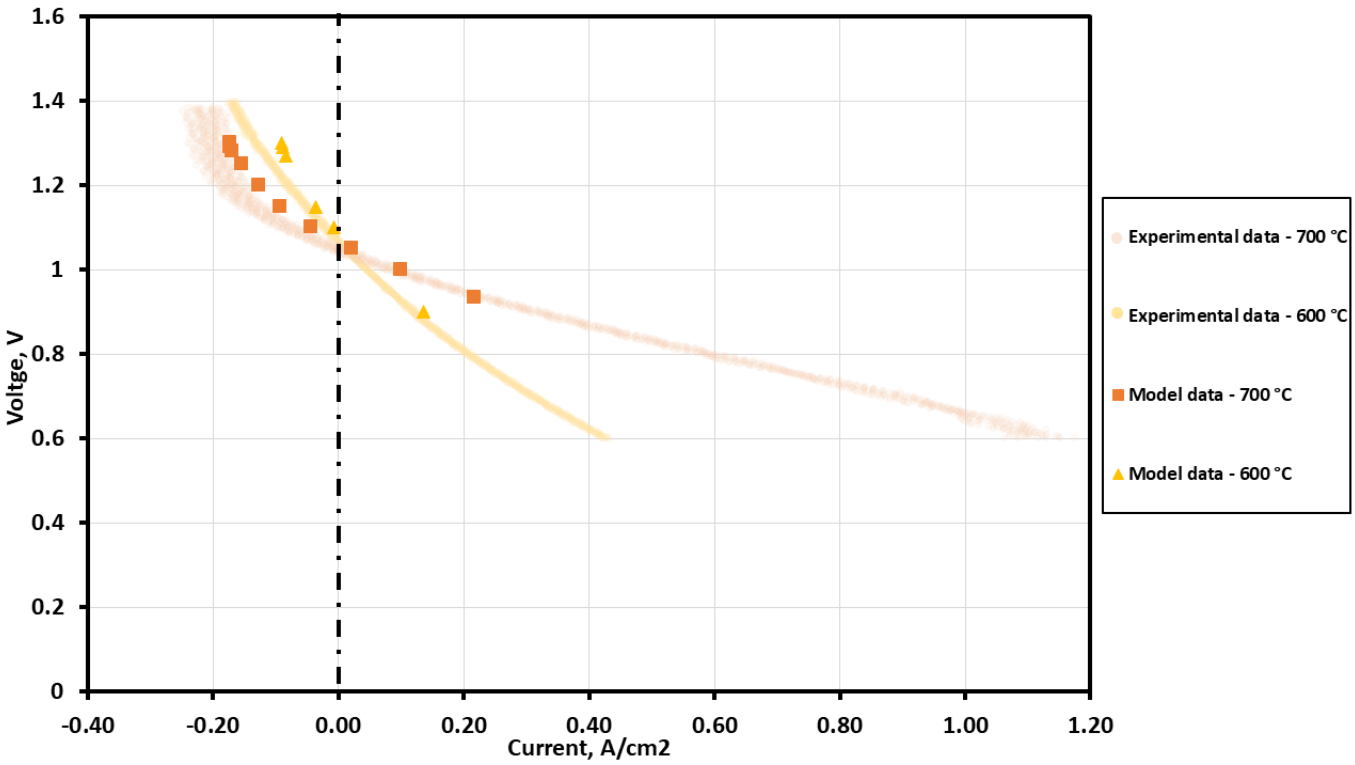

Figure 5.8: *I/U* curve of the experimental and model measurements. The operating conditions for this measurement are the default settings descried in Table Table 5.1, with inlet gas composition on the fuel side of 10% H_2O and 90% H_2. These low humidification conditions are described as **'FC operating points'**.

In the FC operating mode, Figure 5.8, the model captures the trend of the experimental data. In the FC mode only a limited number of simulation points could be computed due to convergence issues. For the FC operating points, the model underestimates the performance, by predicting lower current densities for higher voltages. And for some EC operating points at 600°C, the model overestimated the performance, by predicting lower current densities for lower voltages. This can be happening because of the gas conversion loss and adverse gas composition for EC mode in the these operating conditions.

Despite these limitations, the model exhibits strong qualitative agreement with the experimental data and captures key trends across temperature and operational regimes. These validation results support the use of the model for further analysis of overpotential distributions and gas conversion behavior in the cell.

5.1.3 EIS spectra

Electrochemical impedance spectrum for the EC operating point is shown as Nyquist plots measured at 700°C, as introduced in Chapter 2. General information regarding gas variation protocol

and EIS measurement parameters can be found in Chapter 4.
The results are analyzed using both Nyquist plot and ECM fitting, calculated with the DearEIS Python package [23]. DearEIS is a Python package for processing, analyzing, and visualizing impedance spectra. It offers a possibility to conduct Kramers-Kronig linearity test, the results of which are shown in Appendix F. The findings about resistances in the real cell are compared to the ones simulated in the model.

There are two relevant operating points investigated: EC with high steam content (90% H_2O, 10% H_2) and FC with high hydrogen content (10% H_2O, 90% H_2). With both settings the cell can actually operate in both modes, as the cell allows for reversible operation, however, for simplicity of distinguishing gas composition the one with more steam (90% H_2O) is named EC operating point and the one with less steam FC operating point. The fuel-side total flow is 193 ml/min, while the air-side flow is 1400 ml/min. These conditions are the same as those used for *I/U* curve validation (Figure 5.7, Figure 5.8) and MS measurements (Figure 5.6). They are therefore essential benchmarks for comparison with the COMSOL model.

The model is not set up to operate at OCV, but for measurements with load certain contributions from the voltage range extender (challenging to account for in the model as they are AC current frequency dependent) appear, making those measurements unsuitable for the comparison with model results. It is therefore decided to interpolate model results to OCV voltage. Its is done by fitting each type of loss calculated in the model with a linear regression, or with a second order polynomial. The approach to this calculation can be found in Appendix G. The total loss, read out from Figure 5.9 in these experimental results, is compared to the one calculated in the model. The results of this comparison can be found in the Table 5.3 along side a plotted EIS spectra of the EC/FC operating points under loads in Figure G.2.

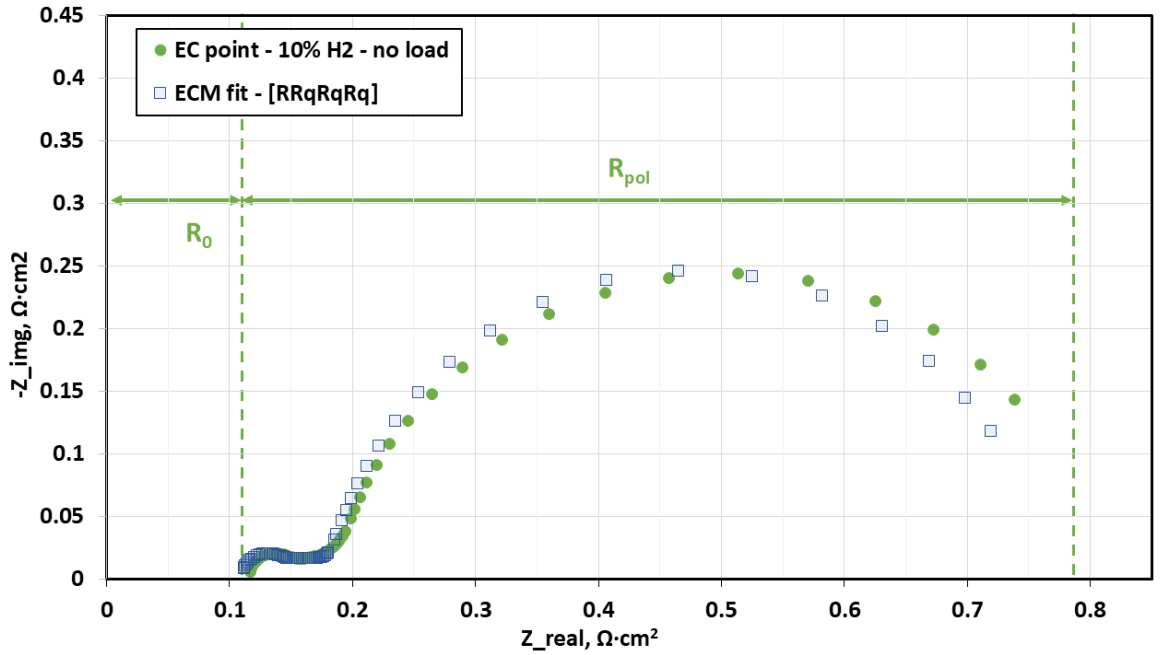

Figure 5.9: EC operating point at OCV measurement

This EIS spectrum is fitted with an ECM circuit consisting of four elements in decreasing order

of frequency [RRqRqRq]. There is one resistor, R, to model the ohmic resistance. There are three Rq elements to model the semi circles.
The R_0 and R_{pol} from the ECM elements are equal to 0.11 $\Omega \cdot cm^2$ and 0.67 $\Omega \cdot cm^2$.

Table 5.3: The polarization and ohmic resistance comparison for the EC operating point at 700°C at OCV, between data from the ECM fit of the experimental measurements and calculated by the interpolated model results.

Resistance	Experimental	Model
Polarization resistance, R_{pol}	0.67 $\Omega \cdot cm^2$	0.6877 $\Omega \cdot cm^2$
Ohmic loss, R_0	0.11 $\Omega \cdot cm^2$	0.1420 $\Omega \cdot cm^2$
Total cell resistance, $R_{pol} + R_0$	0.78 $\Omega \cdot cm^2$	0.8298 $\Omega \cdot cm^2$

The polarization resistance in the model reflects the one of the real cell accurately. That means for this operating point, η_{act}, η_{diff} and gas conversion loss are accurately captured in the model. The ohmic resistance is higher in the model than in the experimental results for OCV. Consequently, the total resistance is also overestimated by 5% when adding both types of resistances.
In principle, it should be possible to conduct such comparison for measurements under loads as well. Due to the yet unquantified, frequency dependent current contribution from the voltage range extender connected to the circuit of FRA and the cell in parallel, the measurements under load are unfeasible to be compared with the steady state model.

5.2 Operation at thermoneutral voltage in the model

In the Section 2.2 the TNV is introduced. It is explained in detail that, in the case of thermoneutral operation, it is not necessary to supply any external heating (or cooling) to the cell.
As operation of the cell at TNV is the goal for technical application, it is of interest to investigate the resulting distributions of conditions, e.g. temperature and overpotentials, along the cell. It is expected that the heat balance equals zero, but it is not known if that is also the case at every position in the cell, due to the contacting in the cell and the reaction progression. This non-isothermal spatially resolved model allows to see local changes of temperature and other variables. Since the temperature directly influences cell resistance and overpotentials, and since overpotentials are linked to several degradation mechanisms, local temperature variations can cause uneven cell degradation, which in turn reduces lifetime [13]. Upper thresholds for the temperature gradient along a cell in a stack suggested in literature range from 5 to 8 $^\circ C/cm$. [24]. Additionally temperature gradients from inlet to outlet of a cell can reach up to about 100K for SOFC operation in 700 or 800 $^\circ$ C [25].
The approach to modeling the temperature distribution in the cell in discussed in the Section 3.2.4. The temperature, T, is a direct result of solving the heat balance Equation 3.17. Plots of T along and across the cell are shown in the following figures: Figure 5.10, Figure 5.11. A 3D plot of the temperature distribution generated in COMSOL can be found in Appendix C, Figure C.5. In the diagrams below there are two datasets plotted: in orange, a rounded cell voltage of 1.3 V is taken as TNV and in blue the exact thermodynamically calculated from enthalpy of 1.2725 V. All the other operating conditions are kept at default, as listed in the Table 5.1.

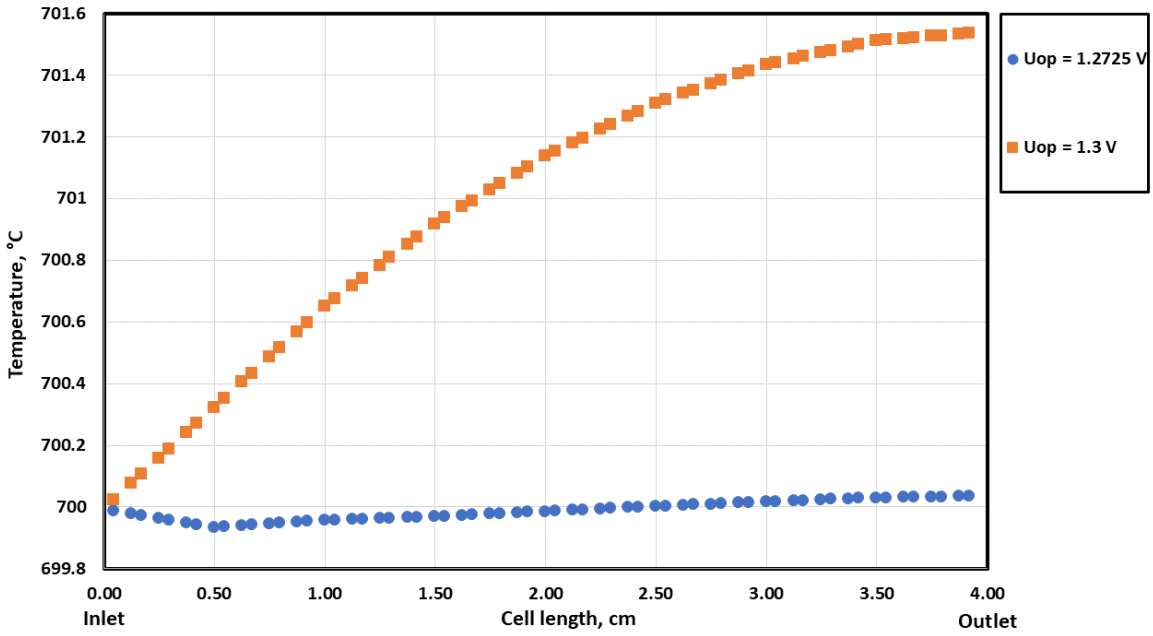

Figure 5.10: Temperature profile along the cell for a 700° C operation. The profile is exported from a cut-line led from the inlet to the outlet of the cell. The line is placed in the symmetric middle of the cell model on the boundary between electrolyte and GDC layer.

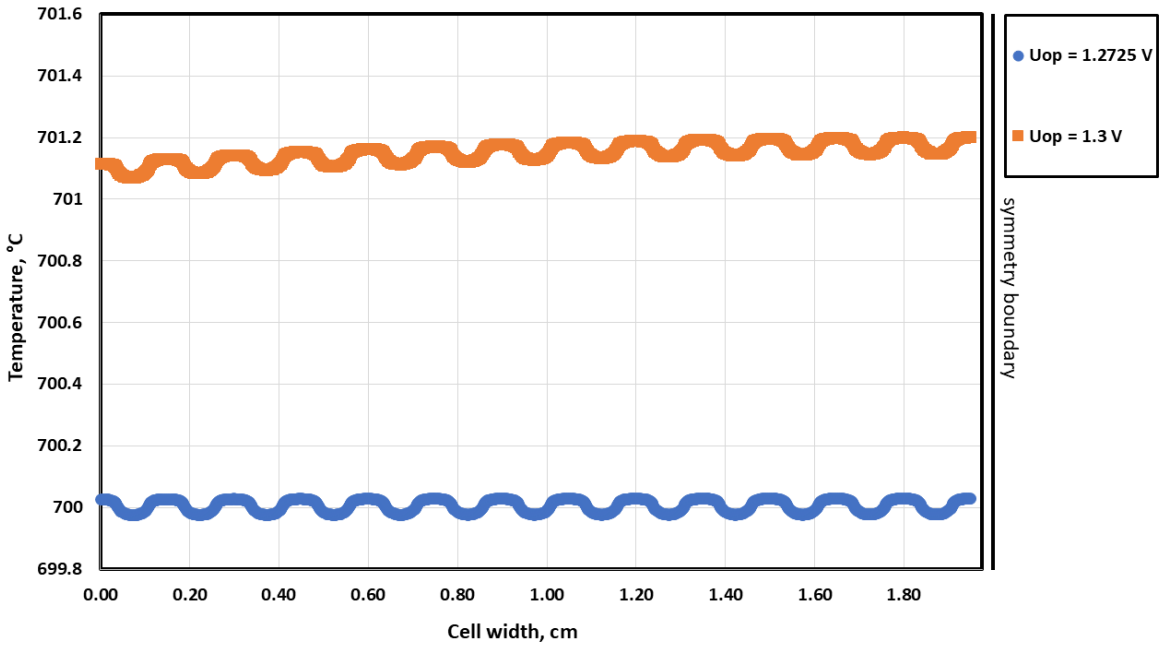

Figure 5.11: Temperature profile across the cell for a 700° C operation. The profile is exported from a cut-line led from the left to the right wall of the cell. The line is placed in the symmetric middle of the length of the cell model on the boundary between electrolyte and GDC layer.

For a operating voltage of 1.3 V the temperature increases along the cell by about 1.5°C, which is more in-depth explained later in this section. The temperature change is small and stays in the range indicated as acceptable in literature for the operation to be described as thermoneutral [26]. The blue line is the TNV though, as it stays at a plateau of 700°C. There is a dip in tem-

perature near the inlet of the cell, as the reaction has started progressing there already, but the counterbalancing heat from overpotentials is not high enough yet, which is shown in the further plots.

Across the cell the temperature is distributed in a periodical manner. The 'waves' are resulting from the metal interconnector contacting with the air electrode. In the areas corresponding to the interconnector rib the temperature is 0.05 $^{\circ}C$ higher, than in areas corresponding to gas channels. This effect, of current flowing through those areas and causing additional heating through resistance, is called contact resistance and that leads to joule/ohmic heating. Additionally, there is also an insignificant increase in temperature of 0.1 $^{\circ}C$ for the 1.3 V operation across the cell towards the middle of the cell. That can be caused by a boundary condition at the outside wall of the cell at position at x=0 in Figure 5.11 (the one without symmetry boundary). Along that wall, heat dissipation to the surroundings is applied. If the the cell model is the exact same temperature as the surroundings (700$^{\circ}C$), naturally no dissipation will occur. However, since there is a minute temperature difference between cell and the environment, some heat might be dissipating along that wall, causing this small gradient across the cell. For the operation at 1.2725 V there is no temperature change towards the symmetry boundary.

Why is the temperature changing at all?

The temperature changes in the cell are all dependent on the heat balance Equation 3.17. On the right hand side of the equation there are source terms, each calculated as either heat sink or source. These terms are plotted along the cell in the Figure 5.12.

The heat stemming from overcoming activation energy barriers is dependent on activation overpotential of the electrochemical reaction at each electrode. Activation heat in the AE, $Q_{act,AE}$, is significantly lower than activation heat on the FE, $Q_{act,AE}$. That is because the reaction on AE has lower activation overpotential (Figure 5.16) and according to Equation 3.21 the lower the η_{act} the lower will the released heat be.
As can be seen, the values of **reaction heat** $Q_{\mathbf{reaction}}$ are negative, indicating that the reaction is endothermic. The system must absorb heat to proceed, as this energy is required to break the chemical bonds in water. ΔS_{tot} increases, as the reaction yields one mole of H_2 and half a mole of O_2 from one mole of H_2O. This increase in the number of gas-phase molecules increases the system's degrees of freedom, thereby contributing to a net increase in entropy.
The ohmic heat, $Q_{\mathbf{ohmic}}$ in the model, stems from ohmic overpotential in the electrolyte and GDC barrier layer. The current going through a material encounters resistance through collisions with atoms of the material and generates heat. This heat is otherwise called joule/ohmic heating and depends on the ionic conductivity of the material.
The contact heat, $Q_{contact}$, is the one that is the results of the periodic distribution of the current density across the cell. It can be seen in the Figure 5.12, that it is a major contribution towards cell heating - on average 68.8% of the total heat released in the cell.
The energy dissipation to the surrounding only occurs when the cell temperature varies from the temperature of the surroundings (700$^{\circ}C$) and is included in the model, but not in the plot as for TNV operation it equals 0. For other operating voltages the contribution is very small, as the cell is insulated (insulation boundary condition) and temperature difference from surroundings is usually not that high.

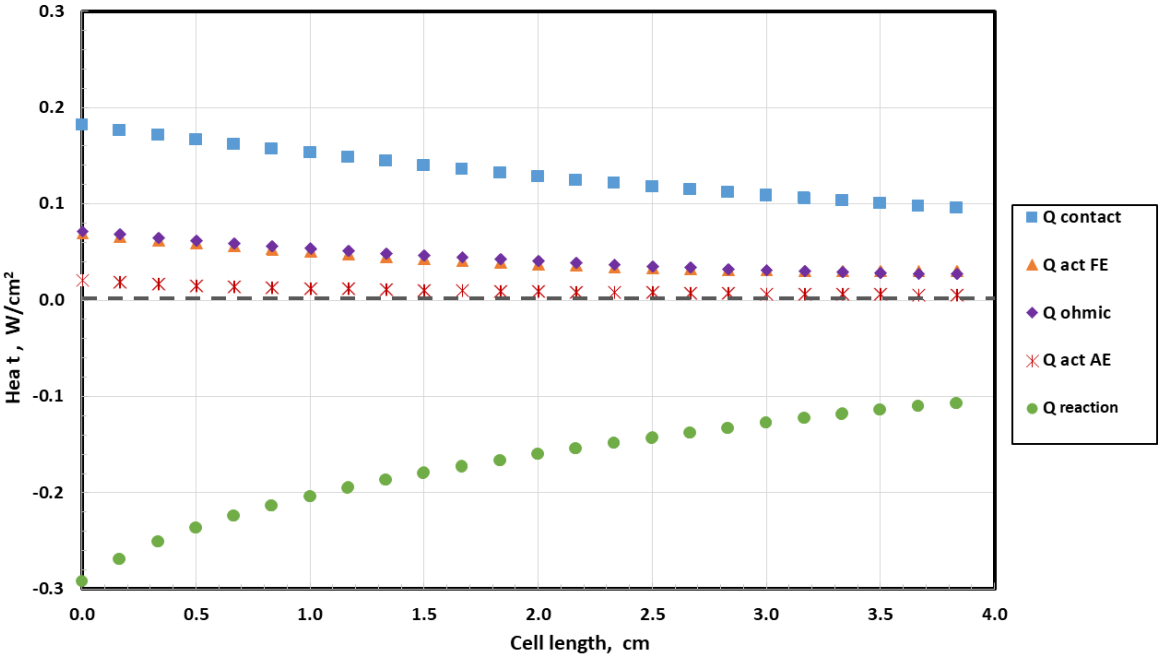

Figure 5.12: Heat sources and sinks in the cell at TNV = 1.2725 and 700°C. The main source of heat in the cell model is contacting heat. The other sources are comparable, while the reaction causes the only and major heat sink.

The values of heat sources and sinks shown in the plot are given in units of W/cm^2, representing local heat flux densities on the surfaces where they are defined. This spatial resolution makes it possible to visualize how heat is generated or absorbed along the length of the cell. In contrast, the values listed in Table 5.4 are the results of surface integrations performed over the respective boundaries. These integrations yield total heat contributions in Watts, corresponding to the net value associated with each heat source or sink across the entire boundary surface. This difference in units arises because integration sums up the heat contributions over an area, while the plots display local intensity values.

For an ideal thermoneutral operation the heat balance for the entire cell is equal to zero, meaning that overall there is no net heat change. It can be seen in the Table 5.4, that at $U_{op} = 1.2725\ V$ in the first column, the balance does equal zero. Which was also the expectation based on the temperature profiles along and across the cell shown earlier.
For the $U_{op} = 1.3\ V$ the temperature along the cell increases by approximately 1.5 $°C$, meaning that excess heat is produced, thus this balance shows a positive value, as shown in the second column of the table.
In literature however, the temperature difference of 2°C between inlet and outlet of the cell is deemed close enough to the real thermoneutral operation [26]. That is why TNV is often rounded up to $U_{op} = 1.3\ V$. This number is also more convenient and universal without many decimals, but some accuracy is lost in the results.

The heat balance becomes positive at higher operating voltages because the heat sources increase more rapidly than the heat sink $Q_{reaction}$. As shown in Equation 3.20, Q_{reaction} depends on the total entropy change ΔS_{tot}, the temperature T, and the charge transfer current density $j_{ct,AE}$. As discussed earlier, in electrolysis mode, the total entropy change ΔS_{tot} becomes less negative (i.e., its absolute value decreases). Similarly, $j_{ct,AE}$ also has negative values in EC mode but increases

along the cell length (again, becoming less negative). The temperature T is always positive and increases along the cell. When all three factors are multiplied, Q_{reaction} remains negative, but its magnitude decreases along the cell.

Table 5.4: Compilation of surface integrated heat sinks and sources

Heat sink/source	$U_{op} = 1.2725\ V$	$U_{op} = 1.30\ V$
$Q_{contact}$	0.51 W	0.73 W
$Q_{act,FE}$	0.31 W	0.42 W
$Q_{act,AE}$	0.07 W	0.10 W
Q_{ohmic}	0.37 W	0.52 W
$Q_{reaction}$	-1.25 W	-1.63 W
Balance	0.00 **W**	0.14 **W**

Current density in TNV operation

In EC mode the electronic current flows in the cell from the air side to the fuel side and is sensitive to local overpotentials. A cross-section of the model is shown in Figure 5.13.As shown in Figure 5.13, regions near the contact points exhibit higher temperatures. The local current density is elevated, because the contact area is smaller and current is concentrated there—which, combined with heightened contact resistance, leads to local heating. Above the gas channels, the current density in the through-plane direction is visibly lower. This difference results from the current only being transported through the MIC. Transportation through MIC requires the current to pass through a narrower cross-section, half the width of the space in the electrode. Notably, at the corners where the MIC ribs meet the fuel channels, the electronic current density shows steep gradients. This sharp increase occurs because the vertically incoming current from the electrode must 'squeeze' into a narrow zone and redirect horizontally into the MIC rib.

In the electrolyte layer and the GDC barrier, electronic current does not flow. The distribution shown in Figure 5.13b represents the ionic current, which is plotted on a separate scale ranging from -0.65 A/cm^2 to -0.69 A/cm^2. The ionic current is higher in the regions beneath the gas channels and decreases beneath the contact ribs. This is because on the electrode-electrolyte boundaries underneath the contacting ribs, the concentration of moles ready to react is actually lower than underneath the channels. And the less moles of a reactant react locally, the less current is going to flow in the vicinity of such area.

This behavior is driven by the concentration gradient: underneath the channels, oxygen molecules can easily travel through the AE toward the gas channels to "clear" the path. Under the contacting ribs, the molecules must travel a longer distance within the AE toward the gas channel, which takes more time and leads to local transport limitations—resulting in what could be described as 'choking'. Thanks to efficient porous microstructure of the electrode the diffusion overpotential in those areas does not vary significantly between rib and channel areas. In the C two plots showing oxygen molar fraction distribution from the bottom to the top of the AE are attached (Figure C.7 and Figure C.8). From these plots it can be deduced, that the diffusion overpotential cannot be high, as there is barely any difference between molar fractions of oxygen in the electrode-electrolyte boundary and top of the AE.

The activation overpotential is also affected by the accumulation of reaction products near the electrolyte–electrode interfaces. When the transport rate of these products is slower than the reaction rate, they build up at the reaction sites. This buildup reduces the number of moles that can participate in the reaction, resulting in a lower local current density, as described by Equation 3.6. In such regions, the activation overpotential is lower because fewer moles are reacting, and therefore less driving force (voltage) is required. According to Le Chatelier's principle, the accumulation of products shifts the local equilibrium, further hindering the reaction and reinforcing the drop in local current density.

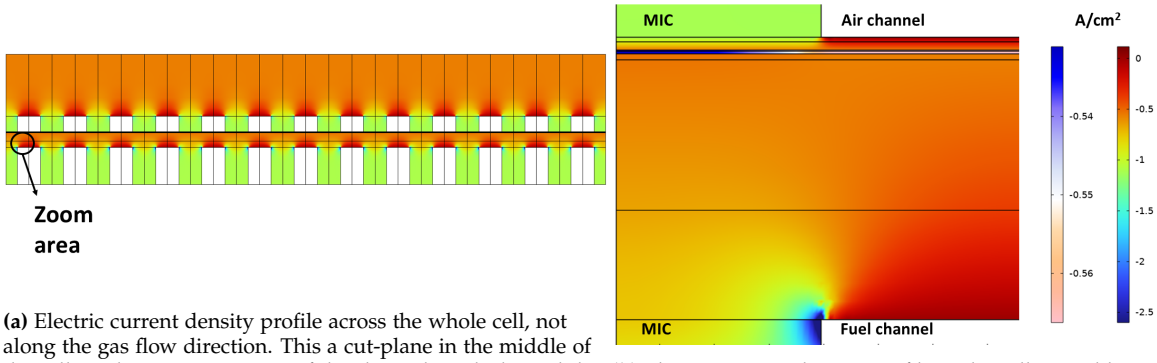

(a) Electric current density profile across the whole cell, not along the gas flow direction. This a cut-plane in the middle of the cell, so that a cross section of the channels and ribs and the current density distribution is visible. The is a wide shot of the entire cross section, with details zoomed in on the plot on the right.

(b) Electric current density profile in the cell assembly - zoomed in. Here a close up on the electrodes and electrolyte is visible with steep gradients on the fuel side and ionic current distribution in the electrolyte and GDC layer.

Figure 5.13: Electric current density profile in a through plane - plots generated in COMSOL

5.3 Overpotentials

In this section investigations regrading overpotentials in the cell are shown. The activation and concentration (diffusion losses + gas conversion losses) overpotentials are considered along the cell with supporting 2D plots generated in COMSOL. Further conclusions about these overpotentials across the cell are also drawn based on scatter plots across the cells.
The ohmic overpotential is discussed somewhat separately. The focus is on the calculation method and increasing the robustness of the model as well as examination of the ionic conductivities.

5.3.1 Gas conversion losses

To understand the distribution of overpotentials in a SOC operating in electrolysis mode, it is helpful to first examine the behavior of the Nernst voltage, U_N, along the cell. As the gas composition evolves due to ongoing reactions, the local Nernst voltage changes accordingly, as described by Equation 2.3. In potentiostatic operation, the applied operating voltage, U_{op}, remains constant. In the model, a contact resistance between ribs and electrodes is quantified by η_{cont}, as introduced in 3.5, the ohmic loss contribution, stemming from the electronic current, is calculated as a left over difference between U_{N} calculated from the Nernst equation and as a sum of U_{N} and overpotentials. **The difference between U_{op} and $U_{\text{N, inlet}}$ represents the total**

overpotential (driving force) of the reaction which results in a certain current that is dependent of the properties of the cell.

The difference between $U_{\text{N, inlet}}$ and U_N at any given point in the cell reflects gas conversion losses, which arise from the change in gas composition along the cell. While $U_{\text{N, inlet}}$ is calculated under inlet conditions and serves as a reference point, the local Nernst voltage accounts for local gas partial pressures and therefore varies spatially. A plot of all these voltages is shown in Figure 5.14, where the differences between them are depicted. **The difference between U_{op} and U_{N}, excluding the total ohmic loss, represents the changing sum of activation and diffusion overpotentials.** It is also visible when looking at Equation 5.4

$$U_{\text{op}} = U_{\text{N}} + \eta_{act} + \eta_{diff} + \text{ohmic losses} \tag{5.4}$$

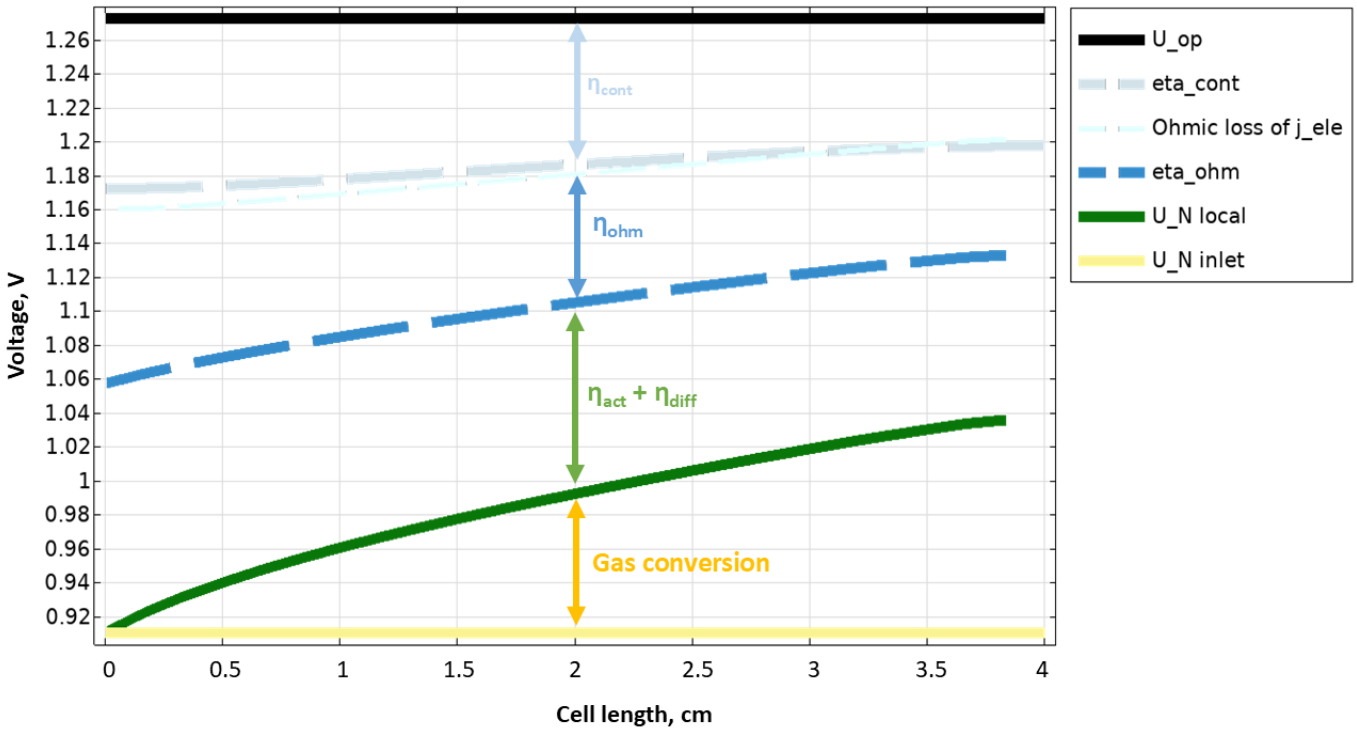

Figure 5.14: Various voltage values along the cell: operating voltage (black at the top), voltage loss resulting from contact resistance (thick light blue dashed), voltage loss resulting from stack material resitivities (thin light blue dashed), voltage loss from ohmic overpotential in the electrolyte and GDC (blue dashed), Nernst voltage (dark green solid), Nernst voltage at the inlet conditions (yellow solid) and calculated Nernst voltage, using the 5.4 in order to double-check the integrity of the model. Plot generated in COMSOL.

By subtracting U_N from U_{op}, the sum of the total overpotential excluding gas conversion is obtained. This sum is also shown in the Figure 5.15, with the black curve. Sum of overpotentials can also be calculated by simply adding all η together, which is also shown in the plot as the gray curve. The sum of the overpotentials is highest at the inlet of the cell and gradually decreases toward the outlet.

In the simulated cell, the inlet gas composition consists of 90% H_2O and 10% H_2, resulting in

a local Nernst voltage of approximately 0.91 V at the inlet, on the electrode-electrolyte boundary. As the gas is converted along the cell, the hydrogen content increases, and the local Nernst voltage rises to about 1.05 V. When the local Nernst voltage increases, the difference $U_{\text{op}} - U_N$ diminishes. If this difference becomes smaller, so does the total overpotential sum. In this way, the gas conversion losses effectively govern the trend of the activation and diffusion overpotentials, suppressing their expected rise. These two overpotentials are mainly affected, as the total ohmic losses (η_{cont} + η_{ohm} + ohmic loss from j_{ele}) are not dependent on gas composition. They are however dependent on the current density, therefore subtle change of total cell resistance in the cell is also visible in the graph.

Around 0.015 m in the cell, the gas composition changes in such a way that on the fuel side of the cell, there is more hydrogen than steam. The electrolysis still continues, since the applied operating voltage U_{op} remains significantly higher than U_N and even more so than the U_{rev}, described in 2.4. This local change can be observed when looking at the diffusion overpotential distribution on the fuel side later on in the Figure 5.17.

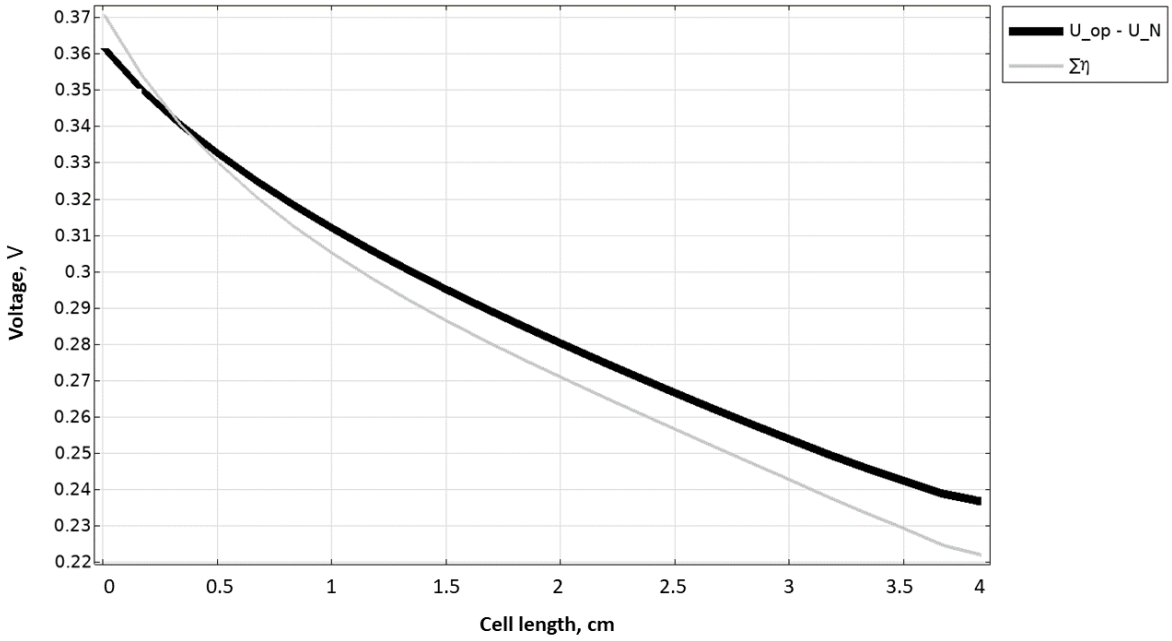

Figure 5.15: Sum of overpotentials calculated in two possible ways. The sum of η is positive as this is he absolute value. This way the sum of η can be easily compared with the the voltage difference, based on the equation 5.4. Plot generated in COMSOL.

The distribution of overpotentials closely follows the trends observed in the voltage profiles: the total overpotential is largest at the inlet of the cell and progressively decreases (becomes less negative) towards the outlet. In electrolysis mode, overpotentials are the driving force for the electrochemical reaction. For potentiostatic operation voltage must be applied to overcome the thermodynamic barriers, and the greater the overpotential, the more molecules can be converted, resulting in higher current density, as described by Equation 3.6.

In the simulated cell, the current density is highest at the inlet, indicating that most of the steam splitting reactions occur in that region. This correlates with a larger activation overpotential near

the inlet: a higher reaction rate requires overcoming greater kinetic barriers, resulting in higher local activation losses. A closer look at the distribution of the current density along the cell is taken in the Figure 5.23.
The diffusion overpotential remains relatively small throughout the cell, which is attributed to efficient design of the porous microstructure in the electrodes and relatively thin AE.
At the outlet, the combined activation, diffusion and ohmic overpotentials are further reduced due to gas conversion effects. As water is consumed and hydrogen accumulates, the local Nernst voltage increases, decreasing the available driving force ($U_{\text{op}} - U_N$) and thus lowering the available overpotentials, thus the driving force for the electrochemical reaction.

5.3.2 Activation overpotential

The activation overpotential is defined on the electrode-electrolyte boundary on both AE (Equation D.4) and FE (Equation D.3). An overview of this overpotential profile is provided in the Figure 5.16.

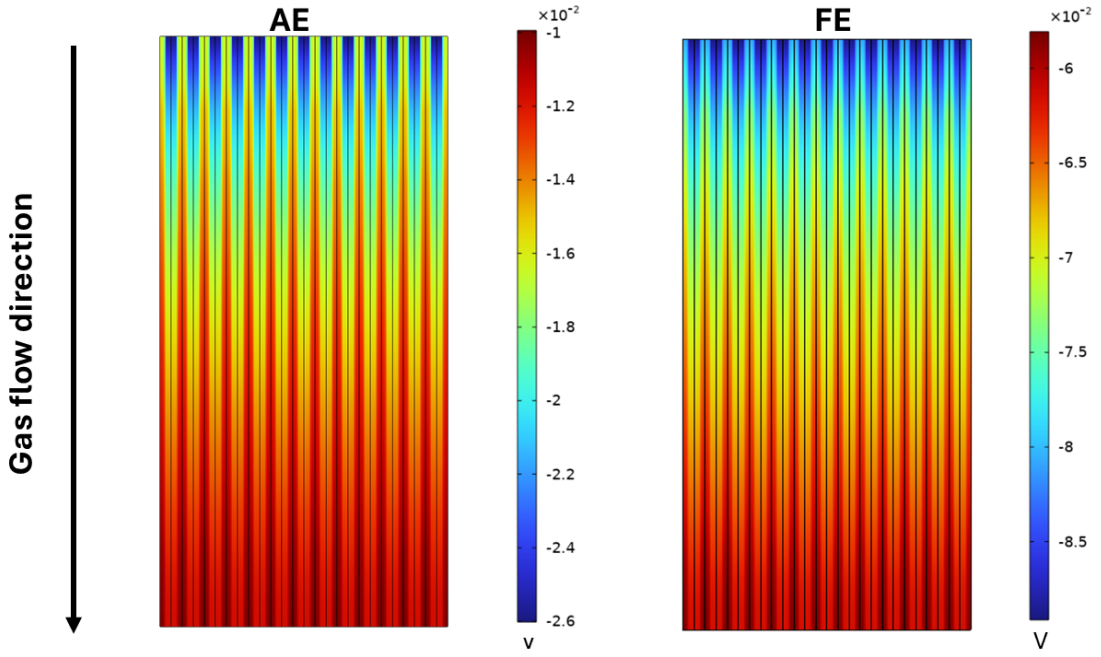

Figure 5.16: Activation overpotential on AE-electrolyte boundary (left) and FE-electrolyte boundary (right). Plot generated in COMSOL.

In this plot it can be seen that the overpotential has about 4 times lower values on the air side, than on the fuel side. The activation overpotential is lower on the air side compared to the fuel side because of the more favorable reaction kinetics. Activation overpotential indicates how much energy is spared on the process from the total overpotential budget of $U_{op} - U_{N,inlet}$ or $U_{op} - U_N$ as introduced above.

The overpotential is decreasing along the cell, because the current density is decreasing along the cell, meaning less and less electrochemical reactions are occurring. If less electrochemical reactions are occurring, that means less energy is required to overcome the activation energy of those reactions.

It can also be seen, that as predicted in the section above, the contacting ribs do cause changes in the overpotential profile. Across the cell the activation overpotential for both electrodes is distributed periodically, as already discussed. For more exact values, Figure C.9 is provided in the C.

5.3.3 Diffusion overpotential

The diffusion overpotential is defined on the electrode-electrolyte boundaries as well. This overpotential is related to the ratio between molar fraction of species on the electrode-electrolyte boundary and on top of the air electrode. For FE it is defined with Equation D.5 and for AE with Equation D.6. An overview, similarly as above is shown in a 2D plot Figure 5.17.

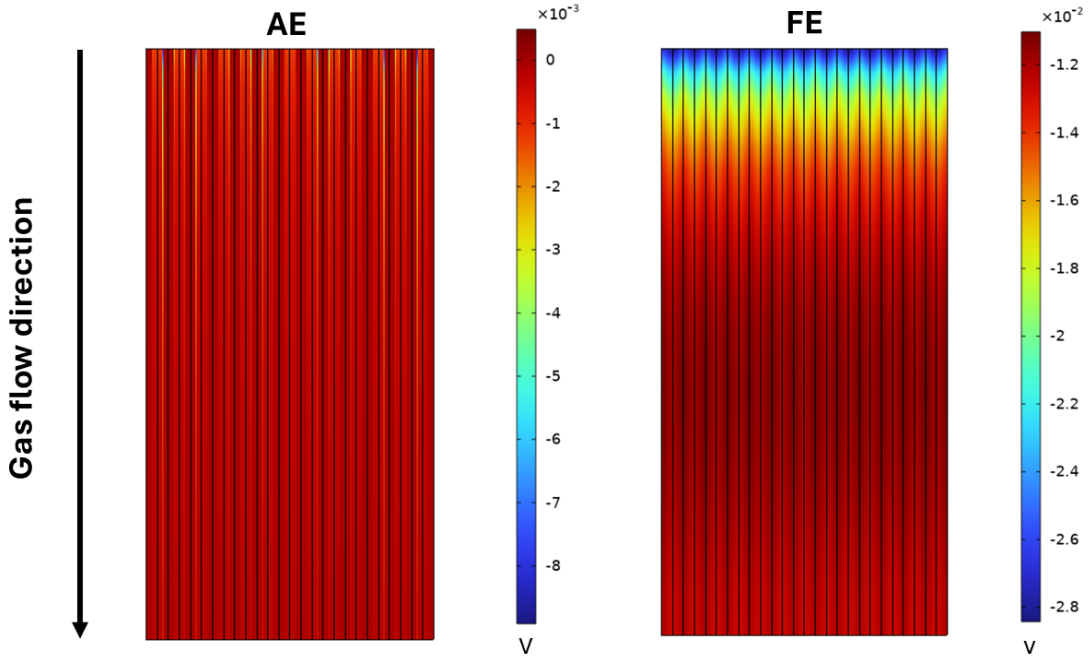

Figure 5.17: Diffusion overpotential on AE-electrolyte boundary (left) and FE-electrolyte boundary (right). Plot generated in COMSOL.

The diffusion overpotential is the indicator of the species ability to travel through the electrode. The more porous, less tortuous the electrode is the more efficiently the species is able to travel though it. It is also heavily dependent on the electrode thickness. If the gradient between the bottom and top of the electrode is small, the diffusion overpotential is also small.

It is mentioned in the sections above that for this simulated cell, the gradients on the air side are actually very low, as shown in Figure C.7 and Figure C.8 in Appendix C. That is due to a small thickness of the AE. At the inlet especially, at the boundaries of rib and channels steep gradients occur. That is due to the large difference in oxygen molar fraction underneath the ribs or channels and is potentially a numerical artifact.

On the fuel side, the diffusion overpotential is more complex than on the air side, as H_2O molecules diffuse toward the electrode–electrolyte interface, while H_2 molecules move in the opposite direction, away from it. In comparison to the AE, FE is around 10 time thicker, which

automatically means higher diffusion overpotential.
A higher diffusion overpotential is observed at the inlet, where the gas composition is 90% H_2O and 10% H_2. As the electrochemical reaction proceeds, a lot of H_2 is generated and H_2O is consumed, which creates steeper concentration gradients between the gas channel and the reaction zone. This steep gradient — characterized by a lower H_2O concentration and higher H_2 concentration at the bottom of the electrode compared to the top — results in a large diffusion overpotential.

As the gas composition evolves along the cell, diffusion gradually compensates for these gradients, and the difference between bulk and interface gas fractions becomes smaller. Consequently, the concentration overpotential stabilizes. Around 0.015 m of the cell length, in the middle of the cell, a shift occurs: the local composition at the reaction sites becomes more H_2-rich than H_2O-rich. This is the point where the fuel gas composition becomes richer in H_2. The reversed gradient reduces the driving force for H_2 diffusion away from the interface and H_2O diffusion toward it, resulting in a visible drop in diffusion overpotential. After this point, the composition gradient flattens, and the diffusion overpotential becomes approximately constant again toward the outlet. The diffusion overpotential along the cell is also influenced by the current density changes along the cell.

5.3.4 Ohmic overpotential

The ohmic overpotential arises in a real cell due to charge transport resistances. It includes contributions from both ionic and electronic charge transport; however, the electronic contribution is significantly smaller, due to the significantly higher electronic conductivity of the materials of the investigated cell and stack components. This overpotential scales linearly with the current and can be expressed as the sum of individual ohmic losses from each layer of the cell, as described in Equation 5.5. In the model at TNV in 700°C, the ohmic overpotential constitutes 31.7% of the entire loss caused by the ohmic resistances.

$$\eta_{ohm} = \sum_{\text{layer}} \left(j_{ct} \cdot ASR_{\text{layer}} \right) \tag{5.5}$$

Each layer's ohmic loss is defined by its area-specific resistance (ASR), which is calculated according to Equation 5.6. ASR is given in units of $\Omega \cdot m^2$ and defined as the voltage drop across the layer divided by the current density.

$$ASR = \frac{\phi_1 - \phi_2}{j} \tag{5.6}$$

In this model, the electric potential ϕ is calculated using Equations 3.2 and 3.3, introduced earlier in the section on charge transport 3.2.1. It can be seen that material conductivity, $\sigma_{ele/ion}$ plays an important role in those equations. The conductivity of each material (and thus domain and layer) is defined through empirical, temperature-dependent expressions. Higher temperatures improve ionic and electronic conductivity, thus reducing the potential drop across a given layer for a constant current density and consequently lowering the ASR.
However, for the material combination of the investigated cell an additional challenge arises due to the formation of an interdiffusion (ID) layer at the GDC barrier layer-electrolyte interface. This layer forms due to species migration between the adjacent materials and typically exhibits significantly reduced conductivity compared to either bulk GDC or electrolyte [27]. Since this

layer has an unknown composition, empirical equations for the bulk conductivities of each material fail to accurately capture its contribution to resistance.
To address this, a conductivity that includes the ID layer and experimental set up inductance can be determined experimentally. Impedance spectroscopy under open-circuit conditions with temperature variation is used, and the equivalent circuit is fitted to extract the ohmic resistance R_{ohm}, which mainly consists of contributions from GDC, the electrolyte, and the ID layer. The experimental conductivity is then modeled by Equation 5.7. In this expression the conductivities of ID, GDC and electrolyte are combined.

$$\sigma = \left(l_{\text{ely}} + l_{\text{AE}}\right) \cdot \left(\frac{T}{B_{\text{ohm}}} \cdot \exp\left(\frac{E_{\text{act,ohm}}}{RT}\right)\right)^{-1} \tag{5.7}$$

Here, T is the temperature in Kelvin, $E_{act,ohm}$ is the activation energy, and B_{ohm} is a material-specific constant in [S·K/m^2]. From fitting the experimentally determined resistances to 5.7, the parameters $B_{ohm} = 6.41 \cdot 10^{12}\ SK/m^2$ and $E_{act,ohm} = 92.6 \cdot 10^3\ J/mol$ are determined.

To isolate the resistance of the ID layer, the model subtracts the bulk resistance of the pure electrolyte and barrier layer (calculated from empirical conductivities of YSZ and GDC) from the total experimentally derived resistance of the cell which includes the ID layer resistance. This gives the additional resistance mainly attributed to the interdiffusion region, but also influences from the experimental investigation like test bench artifacts of influences of electronic current flow. A schematic explanation is shown in Figure 5.18.

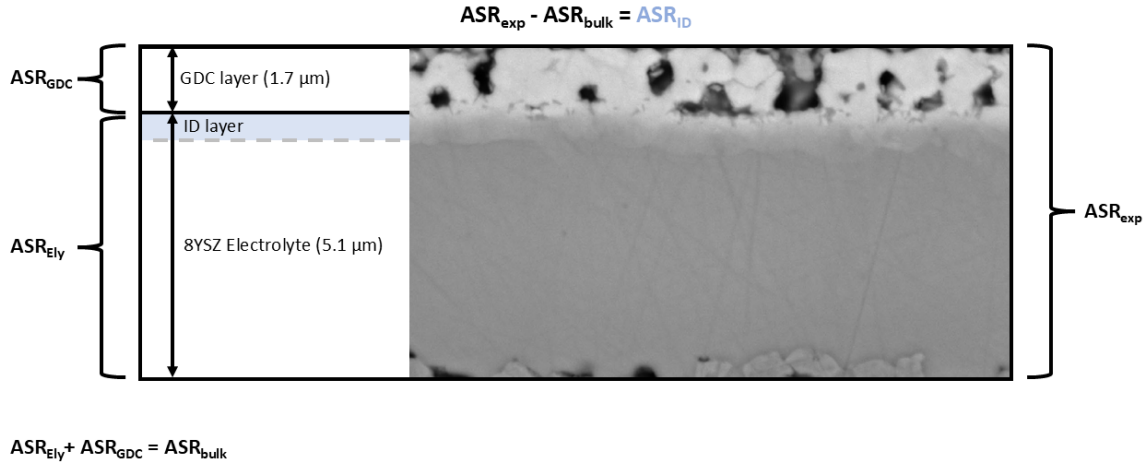

Figure 5.18: The concept of calculating ASR_{ID} illustrated with a scanning electron microscope (SEM) picture of the investigated cell. The ASR of the interdiffusion layer is determined by subtracting the electrolyte and GDC layer resistances from the experimental measured total resistance.

The ASR of the ID layer is implemented in the model as a temperature-dependent variable added at the electrolyte-GDC interface in form of additional surface resistance. The resulting resistance is in agreement with values measured by J. Szasz in [27] at 800 °C. Its temperature dependence is fitted with a second order polynomial, as shown in Figure 5.19 and implemented in the model as

such. It becomes evident that models using bulk conductivities alone underestimate the ohmic resistance of the cell by 72%. Once the ID layer is included, the simulation more closely matches experimental results reducing the deviation by 70%, down to 2.2%.

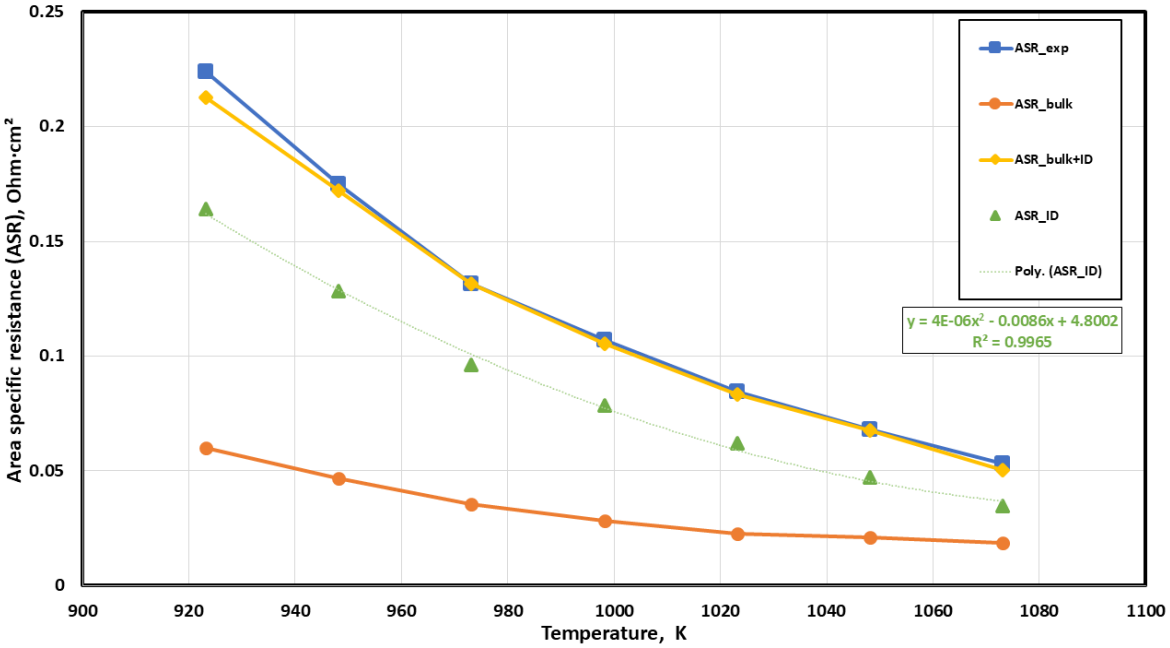

Figure 5.19: Dependency of the ASR on temperature for different layers and calculation approaches. The dotted line indicates the derived expression for resistance attributed to the interdiffusion layer (Figure 5.18).

To further show the impact of the different approaches to consider the ohmic resistance of the cell, thicknesses of the electrolyte (default 5 μm) and GDC (2 μm) are varied. This is done for both the experimentally derived and bulk+ID models. Figure 5.20 shows the results. The model using empirical data tends to overestimate resistance due to the scaling of the ID layer thickness, while the bulk+ID approach reflects more realistic behavior, as ID is only defined as a surface resistance.

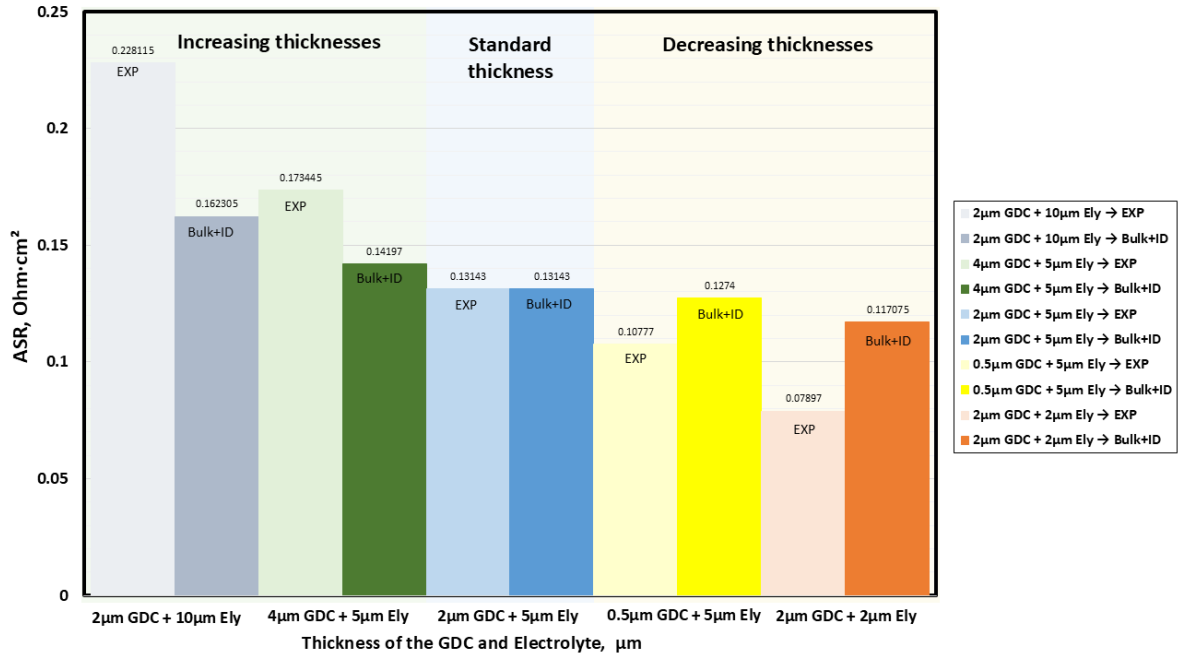

Figure 5.20: Comparison of total ohmic area-specific resistance (ASR) for varying electrolyte and GDC layer thicknesses using two modeling approaches. The experimental model scales the ID layer with total thickness, leading to overestimated resistance at high thicknesses, the Bulk+ID approach treats ID as a fixed surface resistance, capturing more realistic trends.

From the Figure 5.20 it can be concluded, that while investigating the impact of the ohmic overpotential on total cell performance for different layer thicknesses, bulk and interdiffusion layer have to be considered independently. Between both approaches, large differences from the standard assumed thickness occur. Deviations of up to 83% in ohmic ASR are calculated when halving the GDC thickness, between the experimental assessment and the bulk+ID approach. The average difference between those two approaches is 75%, which aligns well with the values seen for the Figure 5.19.

5.3.5 Summary

To summarize the investigations conducted in the model, it is of interest to examine the contribution of each overpotential still under thermoneutral voltage conditions. A pie chart in Figure 5.21 visualizes the share of each calculated overpotential based on the voltage breakdown shown in Figure 5.14 keeping the same color scheme. These values are computed as integrals over the respective boundaries where the overpotentials are defined, providing a view of the overall loss distribution in the entire cell.
The result confirms that gas conversion loss constitutes the largest contribution to total polarization losses under TNV operation. This finding is consistent with the Nernst voltage profile shown earlier in Figure 5.14, which increases steadily along the cell length due to the evolving gas composition, simultaneously reducing the effective driving force for the reaction towards the outlet. The local contributions of the overpotentials at inlet and outlet are found in Figure 5.22.

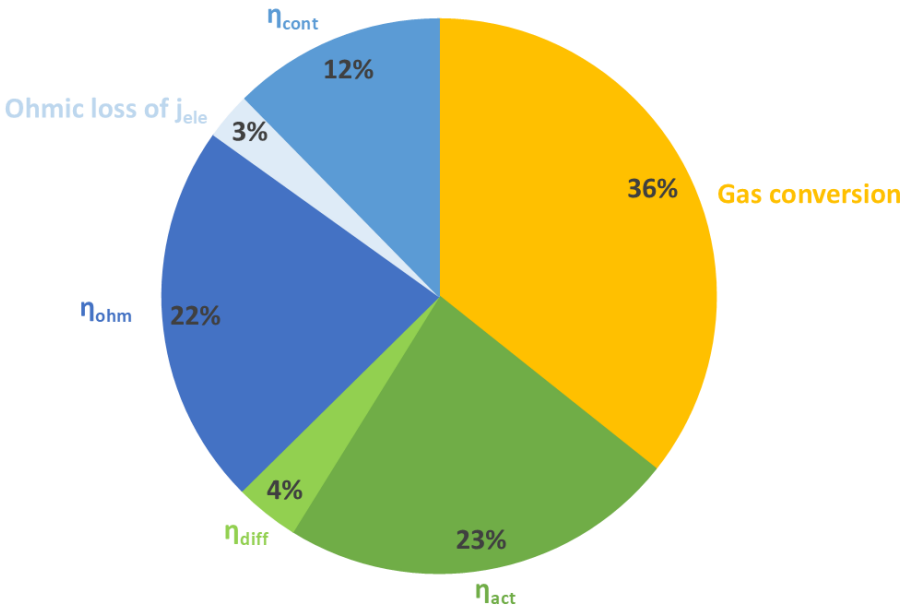

Figure 5.21: Average contribution of each overpotential to the total overpotential of the cell at TNV calculated in the model, based on the Figure 5.14.

(a) At the inlet gas conversion loss does not exist, as no gas is converted yet. The contribution to the total overpotential from activation and diffusion is at 39% and 28% constitutes of ohmic losses.

(b) At the outlet gas conversion loss has the biggest share among overpotentials at 34%, reducing the contribution from activation and diffusion to 26%. The ohmic losses do not change as drastically.

Figure 5.22: Local - inlet and outlet - contributions of each overpotential at TNV in 700°C.

The simulated data reflects this behavior, as shown in 2D plots in Figure 5.16 and Figure 5.17: diffusion overpotential is highest at the inlet, where the reactant (steam) concentration is the greatest, and gradually decreases towards the outlet. Activation overpotentials follow a similar trend, as expected from the Butler–Volmer formulation, with the largest values near the inlet where current density is highest.

In contrast, ohmic losses remain relatively constant along the cell and are governed mainly by the electrolyte and barrier layer properties. The gas composition variation on either side of the cell does not bear much influence on the ohmic overpotential. Ohmic overpotential however scales exponentially with current density, that is why some change along the cell is visible. Sharp increase of ohmic overpotential is also observed for the operation under loads in comparison to other measurements at OCV . The inclusion of an interdiffusion layer should improve

accuracy of the modeled resistance, avoiding unrealistic over- or underestimations that occur when relying solely on bulk conductivity assumptions.

Finally, once all overpotential contributions are understood, it is time to return to the current density distribution along the cell. A plot of this distribution is presented in Figure 5.23. Previous sections have already established theoretical expectations: current density should be highest at the fuel inlet, where overpotentials are largest, and should decline smoothly toward the outlet as the available reactants are depleted and the Nernst potential increases. This trend is confirmed by the model. The gradient in current density along the cell corresponds closely with the electrochemical driving forces discussed throughout this chapter.
Additionally, the periodic pattern across the cell, previously presented in Figure 5.13, reflects the influence of metallic interconnect rib geometry and localized contact resistances.

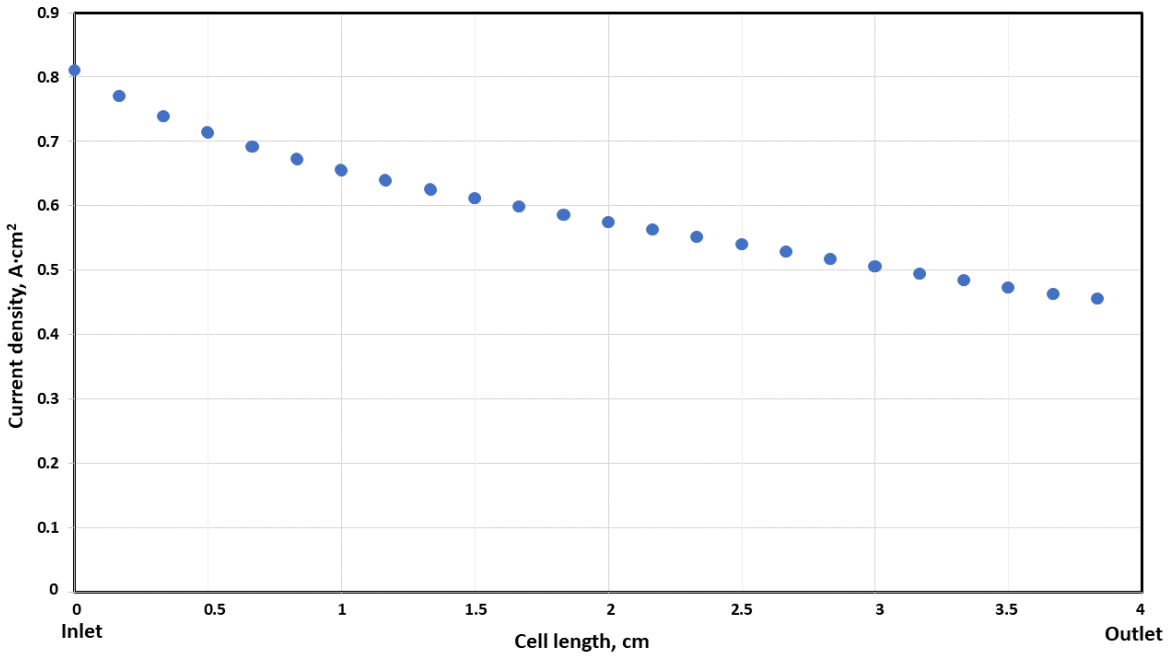

Figure 5.23: Current density along the cell decreases, according to the expectations based on the observed overpotential distribution.

In summary, the TNV simulations offer a comprehensive view of how local overpotentials and current density change along and across the cell. The model successfully captures the dependencies between gas composition, reaction kinetics, and spatial losses, confirming theoretical predictions and reinforcing the importance of spatially resolved modeling for the investigations of overpotentials in SOCs.

Chapter 6

Conclusion

In this project the distribution of overpotentials in a high-temperature solid oxide cell using a combination of modeling and experimental approaches is investigated. A multiphysical 3D finite element stack layer cell model, implemented in COMSOL Multiphysics, is applied to capture the relevant electrochemical reactions, species, charge and heat transport inside the cell. Additionally, experimental validation is conducted via current-voltage curve measurements, electrochemical impedance spectroscopy and mass spectrometry.

The model seems to accurately capture the expected electrochemical behavior of the investigated cell, including the diffusion, heat generation, and variations of overpotentials. Validation against experimental *I/U* data demonstrates good agreement across both fuel cell and electrolysis operating modes.

Gas composition measurements with the mass spectrometer confirm fuel utilization and composition evolution along the cell. Despite challenges regarding water condensation and leakage, the experimental trends match the model predictions at moderate humidification levels. In the model, oxygen leakage is added on the fuel side to reproduce the real gas composition and provides a realistic outlet gas composition, validated quantitatively through reverse calculation of local Nernst voltages.
The method was intended to enable spatially resolved gas conversion analysis to link local composition to current density, but due to insufficient sealing, only outlet measurements could be demonstrated.

The cell is additionally characterized using electrochemical impedance spectroscopy, with experimental results validated through Kramer-Kronig relations. Through an exemplary analysis of an EIS spectra, some conclusions about overpotentials of the investigated cell are drawn. Polarization effects are less prominent and cannot be clearly separated within the scope of this work. Therefore, quantitative analysis focuses on ohmic and total resistances. These values are compared to those predicted by the model, enabling further validation.

As operating the electrolysis cell at the thermoneutral voltage poses advantages in terms of overall efficiency, investigation of the spatial distributions of overpotentials in the cell is mainly conducted for this voltage. While the cell temperature remains stable at 700°C for the TNV of 1.2725 V, local heating effects still occur. Contact resistance, and thus heating, between the air electrode and interconnector ribs introduces periodic temperature fluctuations across the cell

width. These fluctuations are not significant in the scale of the entire cell, but in comparison to any other heat source they have the highest impact. Spatial gradients in current density and activation overpotential develop, particularly near the rib-channel boundaries, due to two times smaller contacting surface. This means current density is twice as high under the ribs, causing these temperature fluctuations through contact heating. This insight highlights the role of geometry and contacting in thermal management and degradation of the cell.

The overpotential distribution is studied in terms of activation, ohmic, and concentration contributions. Different approaches to represent the ohmic overpotential are implemented and compared. Ohmic overpotential is evaluated using an empirical expression for the experimentally (by varying the operating temperature) determined cell resistance, an approach using bulk conductivities of single layers, and a method relating both approaches to incorporate the interdiffusion layer resistance more accurately is proposed. This combined approach should improve the accuracy of the model when investigating the impact of different electrolyte or barrier layer thicknesses. Concentration overpotential is shown to be dominated by gas conversion losses, particularly at the outlet. At the outlet the gas conversion is 36% of all overpotentials. The simulation confirms that the current density distribution is governed by overpotential gradients, with the highest electrochemical activity occurring near the inlet.

Overall, the results demonstrate that the model reproduces the behavior of the cell. It enables analysis of localized phenomena such as contact resistance heating, activation overpotential, and the impact of gas composition evolution. Combined with experimental data, the model provides a strong support as a tool in the optimization of SOECs. The insights gained here inform design choices for cell architecture, operational strategies, and stack integration under thermoneutral conditions or chosen EC-FC operating points.

6.1 Future work

Several ideas for future work emerge from the limitations encountered and the potential extensions of this project. The first priority is to improve the gas outlet line configuration in the experimental setup. In its current form, the orientation of the ceramic outlet promotes condensation and accumulation of water droplets further down the fuel exhaust line, which compromises mass spectrometry measurements and also leaves artifacts in EIS measurements due to abrupt pressure changes, especially at high humidification. This issue could be mitigated either by actively heating the outlet line or by redesigning its configuration to minimize exposure to unheated zones between the oven and the spectrometer interface.

Another critical step involves completing the sealing of the five-point measurement cell holder. This holder was originally intended for spatially resolved gas analysis along the cell length, but the current leakage issues prevent the collection of reliable data. Improving in this area includes applying a ceramic-based glaze/glue as well as introducing a thin layer of gold plating at interfaces of ceramic tubes leading out of the cell holder. Once these improvements are implemented, the mass spectrometer setup can be restored back to its full five-point functionality, allowing for in operando gas composition measurement along the cell—a crucial step for validating gas conversion behavior in the model.

In addition, further electrochemical characterization of the cell would improve the understanding of the experimental data. Beyond the qualitative analysis of impedance spectra conducted here, future work could include comprehensive evaluation of more EIS spectra and their corresponding DRTs and equivalent circuit models. This would allow individual polarization processes to be quantified separately, enabling even more in-depth comparison between experimental measurements and the model.

From the modeling perspective, there are also some possible future investigations. First is the experimental variation of electrolyte thickness to validate the implemented approach for ohmic resistance with the inclusion of the interdiffusion layer and separate bulk conductivities of electrolyte and GDC layer.
Additionally, expanding the model geometry from a single cell to a short stack would allow investigation of likely differences between each layer of the stack. This includes analyzing how inlet gas compositions change across individual layers, influencing gas conversion, temperature profiles, and current distributions.

References

[1] Helge Ingolf Geisler. "Finite Element Method (FEM) Model and Performance Analysis of Solid Oxide Fuel Cells". PhD thesis. Karlsruher Institut für Technologie, Fakultät für Elektrotechnik und Informationstechnik, 2018.

[2] André Leonide. "SOFC Modelling and Parameter Identification by means of Impedance Spectroscopy". PhD thesis. Karlsruher Institut für Technologie, Fakultät für Elektrotechnik und Informationstechnik, 2010.

[3] Niklas Russner. "Modellgestützte Analyse des Stackbetriebs von Festoxidzellen". PhD thesis. Chemieingenieurwesen und Verfahrenstechnik des Karlsruher Instituts für Technologie (KIT), 2021.

[4] Ogemdi Chinwendu Anika, Somtochukwu Godfrey Nnabuife, and Abdulrauf Bello. "Prospects of low and zero-carbon renewable fuels in 1.5-degree net zero emission actualisation by 2050: A critical review". In: *Carbon Capture Science and Technology* (2022).

[5] Samuel Araya et al. "Power-to-X: Technology overview, possibilities and challenges". In: *AAU* (2022).

[6] Samuel Araya et al. "A Review of The Methanol Economy: The Fuel Cell Route". In: *Energies* (2020).

[7] Tom Smolinka et al. *Electrochemical Power Sources: Fundamentals, Systems, and Applications, Chapter 4 - The history of water electrolysis from its beginnings to the present*. Elsevier, 2022.

[8] Marius Muller et al. "High Temperature Solid Oxide Electrolysis - Technology and Modelling". In: *Chemie Ingenieur Technik* (2023).

[9] Ryan O'Hayre et al. *Fuel Cell Fundamentals*. John Wiley and Sons, 2016.

[10] Personal notes, Lecture 6 Fuel Conversion, Vincenzo Liso, Summer Semester 2024.

[11] Diana María Amaya Dueñas. "Perovskite chromite-based fuel electrode for solid oxide cells (SOCs): towards the understanding of the electrochemical performance". PhD thesis. Institut für Gebäudeenergetik, Thermotechnik und Energiespeicherung der Universität Stuttgart, 2023.

[12] S. Korneychuk et al. "In-situ TEM reduction of a solid oxide cell with NiO/YSZ fuel electrode". In: *Journal of Power Sources* (2025).

[13] M.B. Mogensen, Thermodynamics of High Temperature H2O and CO2 Electrolysis, Figshare, 2020, `https://doi.org/10.6084/m9.figshare.12652322.`.

[14] Dino Klotz, André Weber, and Ellen Ivers-Tiffée. "Practical Guidelines for Reliable Electrochemical Characterization of Solid Oxide Fuel Cells". In: *Electrochimica Acta* (2016).

[15] Andrzej Lasia. *Definition of Impedance and Impedance of Electrical Circuits. In: Electrochemical Impedance Spectroscopy and its Applications*. Springer, New York, NY, 2014.

[16] H. Schichlein et al. "Deconvolution of electrochemical impedance spectra for the identification of electrode reaction mechanisms in solid oxide fuel cells". In: *Journal of Applied Electrochemistry* (2002).

[17] A. Leonide, Y. Apel, and E. Ivers-Tiffée. "SOFC Modeling and Parameter Identification by Means of Impedance Spectroscopy". In: *Journal of The Electrochemical Society* (2009).

[18] COMSOL documentation, accessed 02.12.2024: `https://www.comsol.com/multiphysics/convection-diffusion-equation`.

[19] Jichang Liu and James Wei. "Knudsen diffusion in channels and networks". In: *Chemical Engineering Science* (2013).

[20] *Hiden HPR-20 R&D for Advanced Research*. `https://www.hidenanalytical.com/wp-content/uploads/2021/12/HPR-20-RD-2021-.pdf`, Accessed: 07.04.2025.

[21] Edmond de Hoffmann and Vincent Stroobant. *Mass Spectrometry: Principles and Applications*. Wiley, 2001.

[22] *Elcogen Solid Oxide Fuel Cell User Manual, Version 2.2021*. https://www.elcogen.com/wp-content/uploads/2022/10/Elcogen-User-Manual-2910202170-1.pdf, Accessed: 30.03.2025.

[23] Ville Yrjänä. "DearEIS - A GUI program for analyzing impedance spectra". In: *Journal of Open Source Software* (2022).

[24] Theis Løye Skafte et al. "Electrothermally balanced operation of solid oxide electrolysis cells". In: *Journal of Power Sources* (2022).

[25] M. Peksen. "3D thermomechanical behaviour of solid oxide fuel cells operating in different environments". In: *International Journal of Hydrogen Energy* (2013).

[26] Yingqi Liu et al. "Numerical Study of H2 Production and Thermal Stress for Solid Oxide Electrolysis Cells with Various Ribs/Channels". In: *Energies* (2024).

[27] Julian Tibor Szasz. "Charakterisierung und Modellentwicklung von Natur und Funktionalität der Kathoden/Elektrolyt Grenzfläche von Hochtemperatur-Brennstoffzellen (SOFC)". PhD thesis. Karlsruher Institut für Technologie, Fakultät für Technologie, Werkstoffe der Elektrotechnik, 2018.

[28] *Hiden HPR-20 R&D for Advanced Research*. https://www.hidenanalytical.com/wp-content/uploads/2020/08/Hiden-Article_LMUK_JULY_20.pdf, Accessed: 07.04.2025. Published in Labmate UK & Ireland July 2020.

[29] COMSOL documentation, Accessed 18.09.2024: https://www.comsol.com/multiphysics/finite-element-method.

[30] Ismail Celik et al. "Procedure of estimation and Reporting of Uncertainty Due to Discretization in CFD Applications". In: *Journal of Fluids Engineering* (2008).

[31] Jean-Claude Njodzefon et al. "Kinetic Studies on State of the Art Solid Oxide Cells: A Comparison between Hydrogen/Steam and Reformate Fuels". In: *Journal of The Electrochemical Society* (2016).

Appendix A

Appendix: Mass Spectrometry

As mentioned in the Section 4 some of the MS components need a more in-depth presentation that might not be as relevant to understanding the general principle of experimental measurements in this work. However they provide a good understanding and a supplement, to the short introduction paragraph in the aforementioned section 4. In this section a brief description of the MS setup is provided as well as a detailed explanation of ionization assisted by a figure and the working principle of a MS setup.

In the Figure A.1a a technical drawing of a Gas analysis system by Hiden Analytical, model HDR-20 R&D setup is shown. This technical drawing can be found in the manual of the device setup. The important components are pointed out in the figure. The bench-top measurement setup contains a spectrometer, capillary heated inlet unit, a scroll pump and a mobile cart. Real time mass analysis and ion detection require high vacuum (pressure $\leq 10^{-5} mbar$) generated by the pump to transfer ions from atmospheric-pressure environment in the oven to mass analyzer region in the spectrometer.

In the Figure the A.1b there is a photo of the spectrometer itself from [28]. It is rotated the same way, in a way that the user interfaces can be seen. The capillary inlet can be seen in white material. The ionizer, mass filer and detector are packed in an assembly called analyzer gauge head, appearing as metal tube in the photo. Further shown in the Figure A.2b.

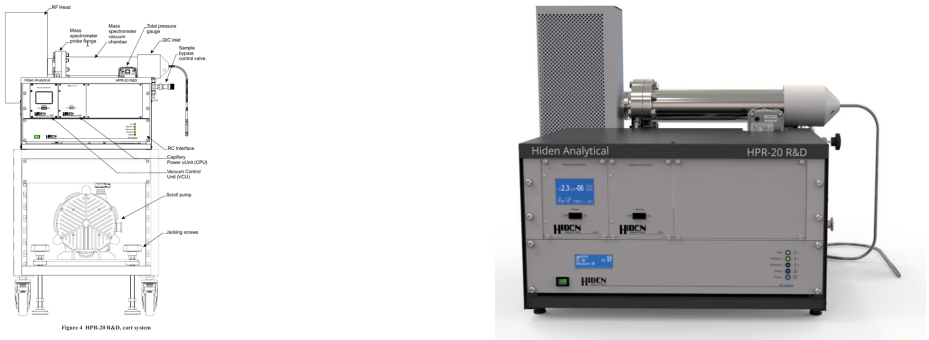

(a) Technical drawing of the MS setup from the device's manual

(b) Side view

Figure A.1: Mass spectrometer manufactured by Hiden Analytical from [28]

The ionization method has been introduced earlier, but its mechanism is more clearly illustrated in Figure A.2a. Gas-phase molecules enter a chamber where they are subjected to electron impact

from a heated filament. The resulting cations are then guided by extraction optics toward the mass filter.

The overall structure of the gauge head is shown in Figure A.2b. After ionization, the positively charged species are directed into the mass filter, which is often a quadrupole system. This configuration consists of two pairs of parallel metal rods, evenly spaced, with opposing electrical potentials applied. The quadrupole is widely favored in MS systems for its rapid scanning capability and broad dynamic range. Opposing pairs of rods have both a DC voltage and an alternating frequency of voltage applied to them. This creates a dynamic electric field. During each step of each frequency scan, only ions with a specific m/Q (mass to charge) value remain stable within the field and reach the detector, while others are destabilized, causing them to collide with the rods and become neutralized.

Finally, the ions reach the detector. One commonly employed type is the Faraday cup, which is a grounded conductive collector paired with a suppressor electrode to minimize errors. As the ions impact the cup, they transfer their charge to the metal, and the resulting current is then accurately measured. [28]

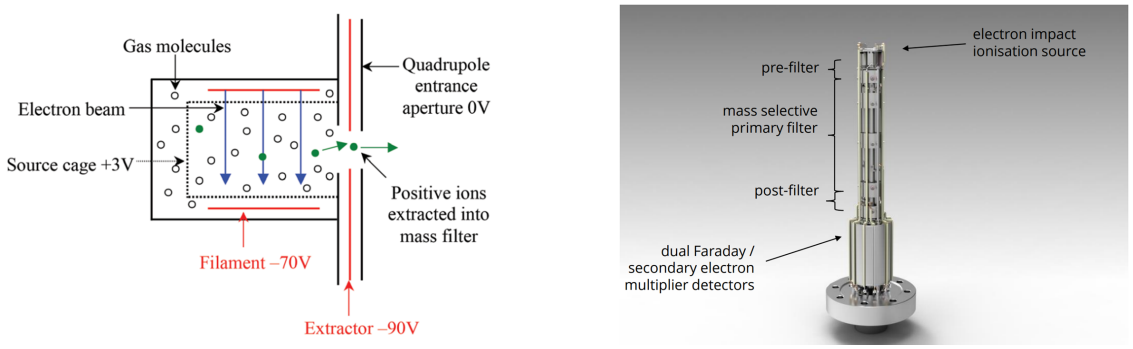

(a) Electron impact ionization

(b) Analyzer gauge head

Figure A.2: Figures from the Hiden Analitycal website [28]

A.1 Calibration protocol

Background partial pressures	N2	H2	O2	H2O	total pressure	cycles	V flow
100% N2	-	2.93E-09	3.75E-10	1.69E-08	2.80E-06	1600	500 ml
100 % H2	2.63E-08	-	7.45E-10	8.98E-08	3.14E-05	400 (water could probably go down more)	300 ml
100% O2	9.11E-09	3.80E-09	-	1.22E-07	1.65E-06	350 (water could probably go more down)	300 ml
100% steam (H2+O2)	1.18E-08	3.32E-07	1.18E-08	-	2.42E-06	100 (lot of noise)	500 ml (H2: 496ml, O2: 250ml)
100% steam (H2+O2) figuring out the flow	1.15E-08	5.43E-08	2.05E-08	-	2.42E-06	50 (little to no changes)	(H2: 490ml, O2: 250ml)
Callibration factors - N2 relative	N2	H2	O2	H2O	total pressure	cycles	V flow
90% N2 / 10% H2	RS factor: 1 before RS: 52.38	RS factor: 8.18 before RS: 47.62	-	-	4.17E-06	20	300
70% N2 / 30% H2	RS factor: 1 before RS: 23.21	RS factor: 7.72 before RS: 76.78	-	-	8.72E-06	15	300
70% N2 / 30% H2O	RS factor: 1 before RS: 75.81	-	-	RS factor: 0.744 before RS: 24.18	2.00E-06	20	300 (210N2, 90H2, 45O2)
70% N2 / 30% O2	RS factor: 1 before RS: 75.87	-	RS factor: 0,742 before RS: 24.12	-	1.76E-06	20	300
60% N2/ 20% H2 / 20%H2O	RS factor: 1 before RS: 25.61	RS factor: 7.88 before RS: 67.27	-	RS factor: 0.834 before RS: 7.12	6.50E-06	17	300 (180N2, 120H2, 30O2)
Callibration factors - H2 relative	N2	H2	O2	H2O	total pressure	cycles	V flow
70% H2 / 30% N2	RS factor: 0.142 before RS: 5.74	RS factor: 1 before RS: 94.25	-	-	2.36E-05	20	300
90% H2 / 10% N2	RS factor: 0.142 before RS: 1.55	RS factor: 1 before RS: 98.5	-	-	2.36E-05	20	300
70% H2 / 30% H2O	-	RS factor: 1 before RS: 94.95	-	RS factor: 0.124 before RS: 5.04	2.00E-05	30	300
90% H2 / 10% H2O	-	RS factor: 1 before RS: 98.5	-	RS factor: 0.134 before RS: 1.46	2.62E-05	20	300
60% H2 / 20% N2 / 20%H2O	RS factor: 0.202 before RS: 5.98	RS factor: 1 before RS: 88.95	-	RS factor: 0.171 before RS: 5.06	1.00E-05	30	300 (60N2, 180H2, 30O2)
Callibration factors - O2 relative	N2	H2	O2	H2O	total pressure	cycles	V flow
70% O2/ 30% H2O	-	-	RS factor: 1 before RS: 71.44	RS factor: 0.932 before RS: 28.55	1.64E-06	50	300 (90H2, 255 O2)
90% O2/ 10% H2O	-	-	RS factor: 1 before RS: 92.19	RS factor: 0.762 before RS: 7.80	1.58E-06	10	300 (30H2, 285 O2)
70% O2 / 30% N2	RS factor: 1.34 before RS: 36.42	-	RS factor: 1 before RS: 63.57	-	1.61E-06	30	300
Callibration factors - H2O relative	N2	H2	O2	H2O	total pressure	cycles	V flow
70% H2O/ 30% H2	-	RS factor: 9.53 before RS: 80.33	-	RS factor: 1 before RS: 19.67	1.10E-05	30	300 (300 H2 , 105 O2)
90% H2O / 10% H2	-	RS factor: 11.5 before RS: 56.12	-	RS factor: 1 before RS: 43.87	6.00E-06	150 (i was talking with Marius)	300 (300H2, 135 O2)
70% H2O/ 30% N2	RS factor: 1.27 before RS: 35.2	-	-	RS factor: 1 before RS: 64.8	2.30E-06	30	300
90% H2O/ 10% N2	RS factor: 1.29 before RS: 87.5	-	-	RS factor: 1 before RS: 12.5	2.58E-06	20	300
70% H2O/ 30% O2	-	-	RS factor: 0.97 before RS: 29.37	RS factor: 1 before RS: 70.62	1.97E-06	50	300(210H2, 195O2)
90% H2O/ 10% O2	-	-	RS factor: 0.936 before RS: 9.42	RS factor: 1 before RS: 90.58			300(270H2, 165O2)
60% H2O/ 20% H2/ 20% N2	RS factor: 1.18 before RS: 8.7	RS factor: 9.38 before RS: 69.16	-	RS factor: 1 before RS: 22.12	7.36E-06	20	300 (60N2, 240H2, 90O2)

Figure A.3: Calibration protocol with RS values (calibration factors).

Appendix B

Appendix: Finite Element Method

B.1 Finite Element Method

The model utilized in this work is described mathematically using partial differential equations. Differential equations include expressions that determine a small change in a dependent variable with respect to a change in an independent variable. When a differential equation is expressed in terms of the derivatives of more than one independent variable, it is referred to as a partial differential equation (PDE). These types of equations unless in a simple case are not possible to solve analytically.
To provide the solution, discretization methods need to be used. These discretization methods approximate the PDEs with numerical model equations. The solution to the numerical model equations are an approximation of the exact solution to the PDEs. The finite element method (FEM) is a numerical method used to compute such approximations [29].
For each element in the mesh, a set of PDEs is solved and passed onto the elements in the vicinity. This is a so called 'divide-and-conquer' approach, where instead of solving for a whole system, equations are solved for smaller domains and assessed together to produce an overall result.

B.1.1 Weak formulation

The explanation will be provided with an example of the temperature distribution in a heat sink based on the step-by-step derivation in COMSOL documentation [29]. The PDE that needs solution in the Ω domain is Equation B.1.

$$\nabla \cdot (-k\nabla T) = g(T, \mathbf{x}) \quad \text{in } \Omega \tag{B.1}$$

For this equation boundary conditions (temperatures at boundaries) need to be defined. In the next step, both sides of the Equation B.1 need to be multiplied by φ, which symbolizes a test function, as shown in Equation B.2. The following operation is to intgerate over the domain.

$$\int_\Omega \nabla \cdot (-k\nabla T)\, \varphi \, dV = \int_\Omega g\varphi \, dV \tag{B.2}$$

The weak formulation is obtained by requiring B.2 to hold for all test functions instead of B.1 for all points in Ω. It is done by applying integration by parts to move the derivatives off the temperature and onto the test function. The approximate solution is expressed as a linear

combination of a set of basis functions φ weighted with T_i coefficients (B.3). The integrals are only non-zero in small regions, where the basis and test functions overlap contributing to the solution.

$$T_h(x) = \sum_i T_i \varphi(x) \tag{B.3}$$

Further the Equation B.3 needs to be discretized with i elements to obtain a system of equations in which the unknown is i amount of T_i coefficients. The search for a solution gets reduced to the calculation of the coefficients T_i from a linear system of equations in a matrix form (B.4).

$$AT_h = b \tag{B.4}$$

A is the stiffness matrix containing gradients of the test and basis functions, T_h is a vector of unknowns and b represents the force of source term. This linear system of equations can be solved numerically for T_i approximation. With known values of the coefficients and basis functions it is now possible to obtain a result for the entire domain from the Equation B.3.

Appendix C

Appendix: Model Geometry

C.1 Explanation of the model geometry

In the Figure C.3 the FE and AE are highlighted according to the legend. The inlet and outlet are indicated with arrows. The purpose of this figure is to ease the understanding of the geometry, as due to its repetitiveness it could be challenging to comprehend where relevant domains are.

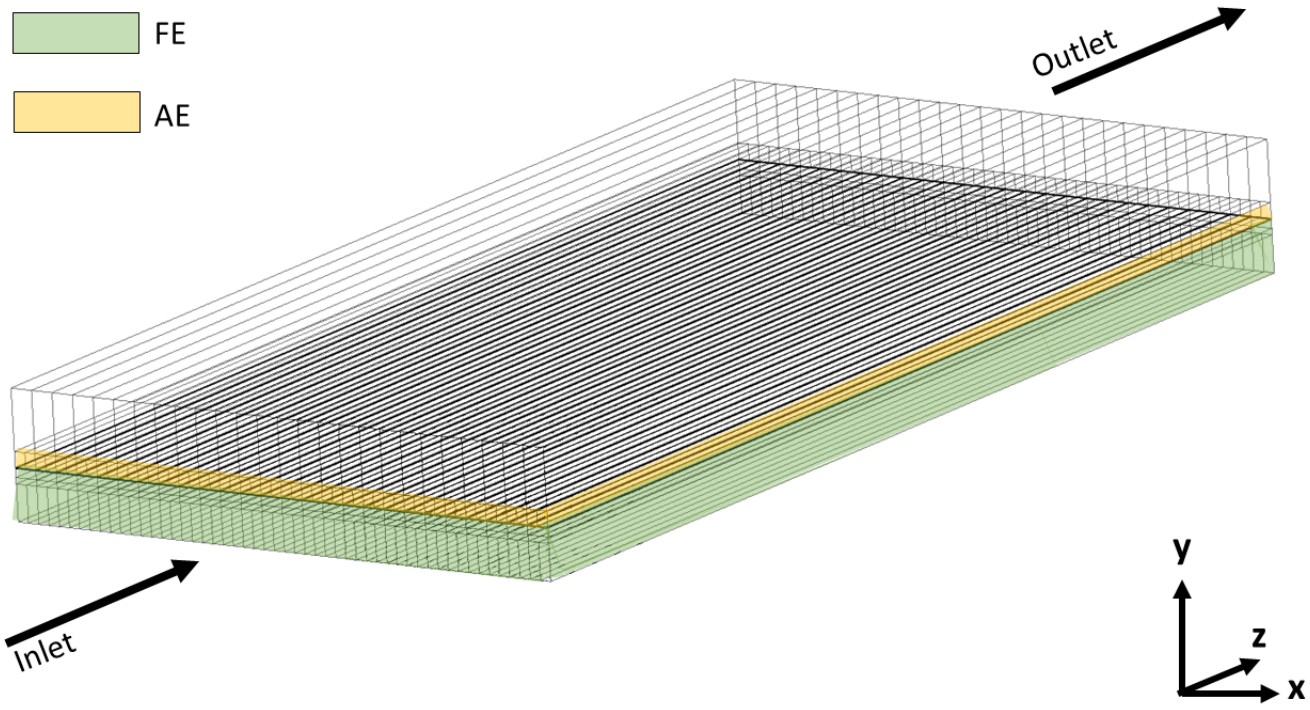

Figure C.1: Additional explanation of the domains in the geometry

C.2 Mesh and Grid Independence Study

Meshing plays a crucial role in the accuracy and efficiency of FEM simulations, particularly for 3D geometries. An effective meshing strategy involves creating a sufficiently dense mesh in regions where sharp gradients are expected—such as near boundaries or interfaces—while

maintaining a coarser mesh in less critical areas to reduce computational load. In this model, a structured mesh is applied. Higher mesh density is used within the cell assembly and in the vicinity of no-slip boundary walls inside the gas channels. To improve control over mesh quality and distribution, the overall geometry is divided into smaller subdomains following the divide-and-conquer approach. Each subdomain is then meshed independently. This meshing strategy is illustrated in Figure C.2 and Figure C.3.

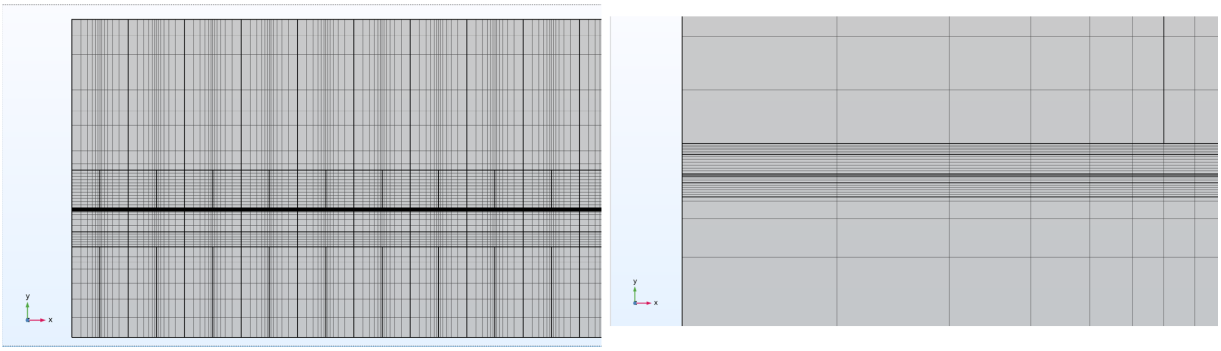

(a) Meshing strategy along the inlet of the cell. Mesh is denser near to walls to capture the steeper gradients in those regions.

(b) Zoomed in meshing strategy in the cell layer too thin to see on the picture C.2a

Figure C.2: Meshing strategy

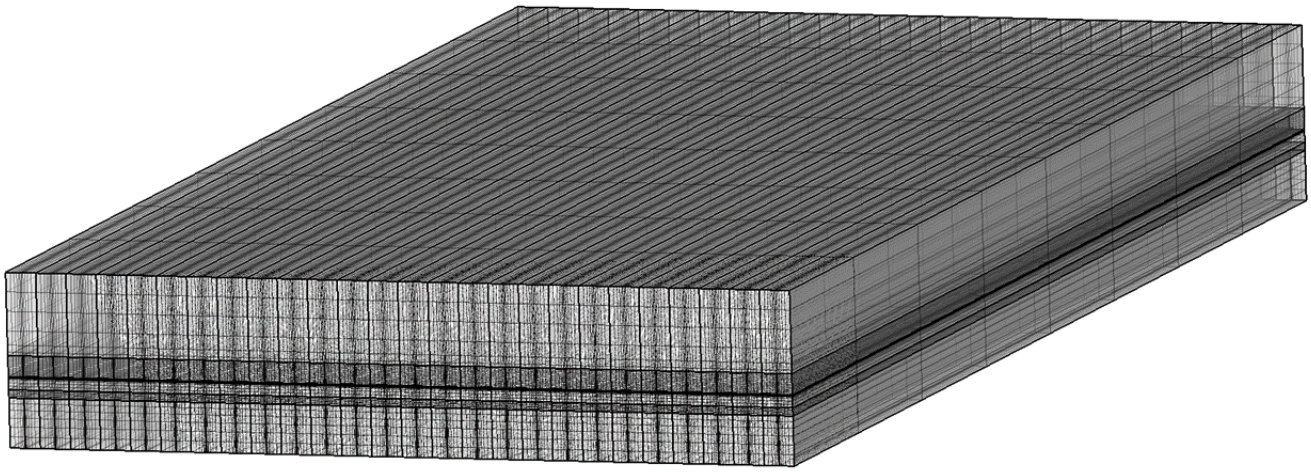

Figure C.3: Mesh of the entire geometry

To ensure the reliability and accuracy of results obtained from a 3D computational model, it is essential to assess the impact of discretization error through a Grid Convergence Index (GCI) study. This type of mesh refinement analysis demonstrates whether the simulation results are independent of the chosen grid resolution. The procedure follows the methodology outlined in

[30], where three systematically refined meshes — coarse, medium, and fine — are compared. The GCI quantifies the relationship between the characteristic grid size and the variation in a selected solution variable. When the GCI value falls below 1%, it can be reasonably concluded that the solution has reached grid independence, meaning the numerical results are no longer significantly influenced by further mesh refinement.
The results of the study are presented in the Figure C.4. The one the left axis an arbitrarily chosen value - electrical current density is plotted with a blue line and green markers. The right axis computation time of models with each of the meshes is shown. This data in the figure is plotted with orange line. The plot suggests that the medium mesh is the most optimal out of the three tested grids. The computation time of that model is exponentially shorter for a medium mesh model and the result is close to the fine mesh one.

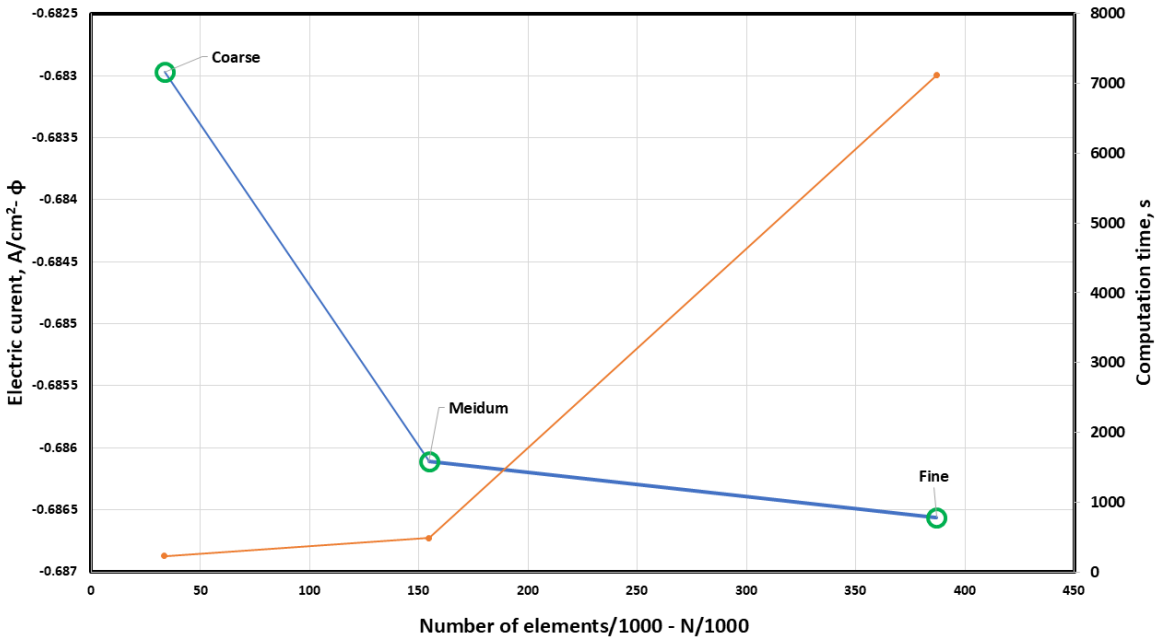

Figure C.4: Results of the GCI study. With the blue line on the plot the arbitrary variable - in this case current density is shown. In orange, the computation time is plotted.

The parameters from the GCI calculation are shown in the Table Table C.1. The calculations are done using a simple python script with a *for* loop as fixed point iterator. Even though the plot suggests that the medium mesh is suitable to use, after a more careful analysis it can be found that the relative errors between coarse and medium mesh is barely 0.1%. The acceptable GCI is 1% meaning that probably the medium mesh could be optimized to be coarser saving up computational resources. It can also be seen by the value of the refinement ratio, r, as the suggest in the [30] value is 1.3. For this study however it equals $r_{c-m} = 1.6622$, which is higher. It also suggest that the medium mesh could probably have a reduced number of elements. Mesh studies however are not the focus of this work, therefore as the medium mesh is in fact suitable to use it is chosen for further calculations.

Table C.1: GCI parameters. N denotes the number of domain elements, h is the grid size, p is the estimated order of convergence. ϕ_{ext} is the extrapolated solution. e is the relative error and GCI is the grid convergence index between mesh levels. The subscripts **c,m,f** mean coarse, medium and fine.

GCI study parameters	Values
N_{coarse}	33696
N_{medium}	154752
N_{fine}	386880
h_{coarse}	4.31117E-03
N_{medium}	2.59364E-03
N_{fine}	1.91101E-03
r_{c-m}	1.6622
r_{m-f}	1.3572
p	3.8232
ϕ_{ext}	-0.686357
e_{c-m}	0.46%
e_{c-m}	0.07%
GCI_{c-m}	0.1%
GCI_{c-m}	0.04%

C.3 Additional plots of chosen of the results

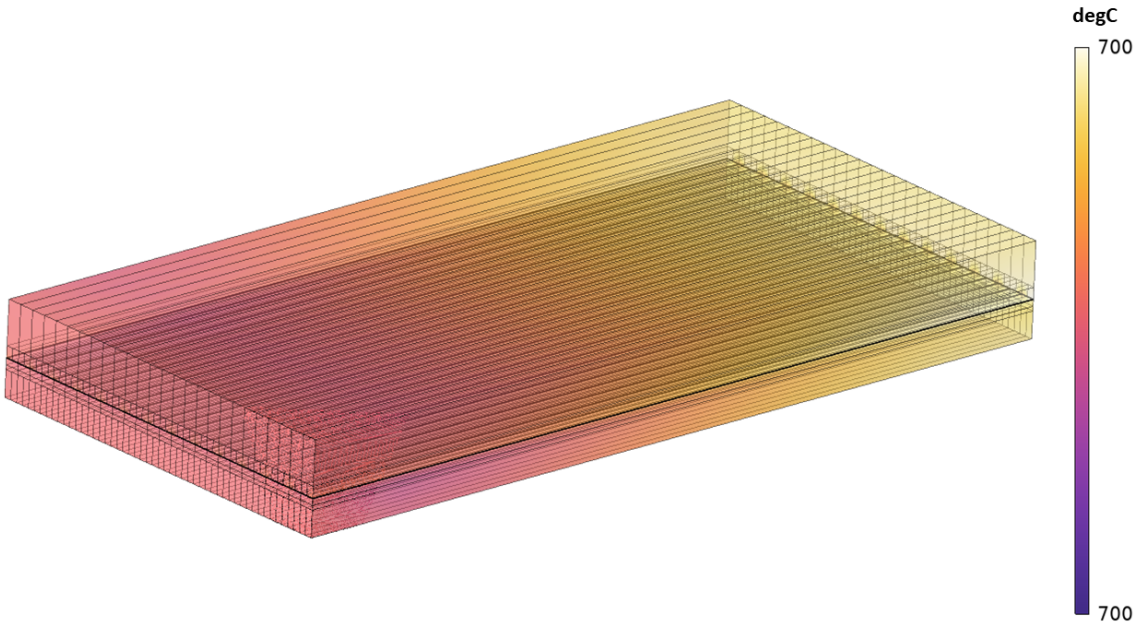

Figure C.5: Temperature profile in the cell for TNV. 3D plot generated in COMSOL

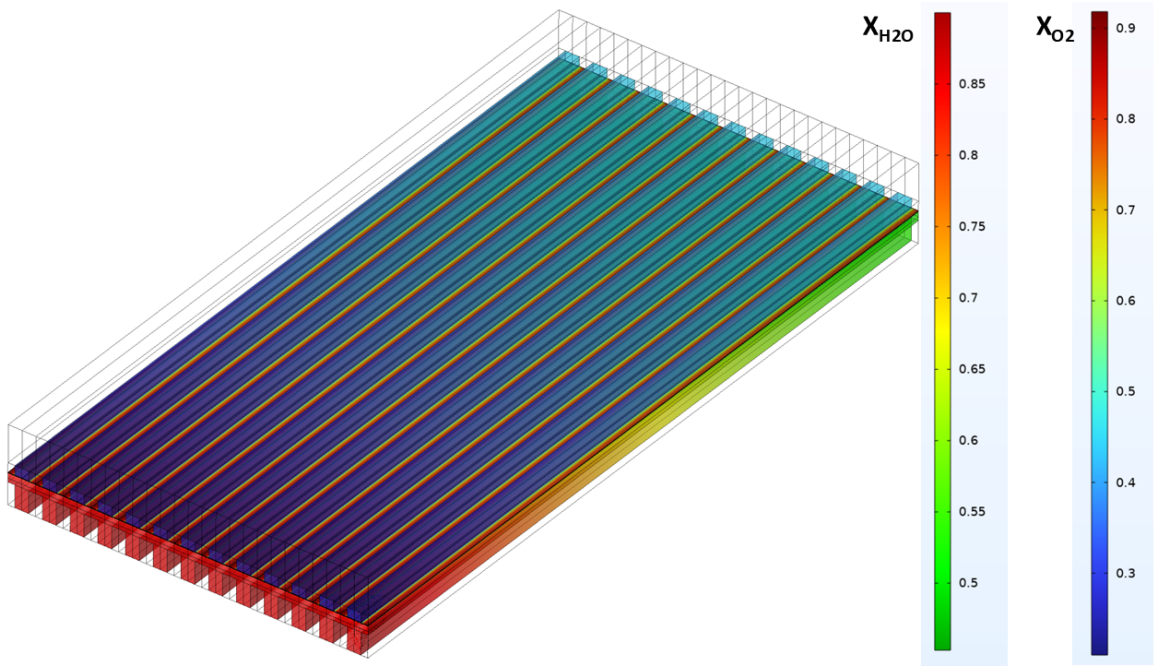

Figure C.6: Species distribution along in the cell. On the bottom - molar fraction of H_2O and on the top - molar fraction of O_2. 3D plot generated in COMSOL

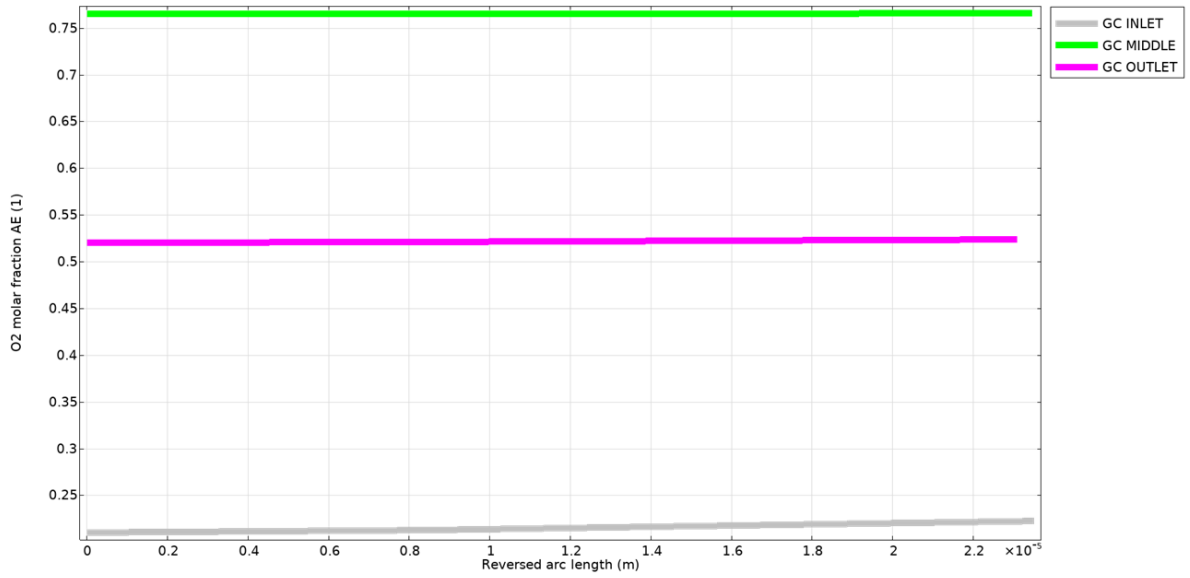

Figure C.7: The profile of oxygen from bottom of the air electrode to the top of the air electrode in the gas channel region. The bottom of the electrode is the electrode-electrolyte boundary, and the top of the electrode is the electrode- gas channel boundary. The profile is taken at the inlet, middle and outlet of the cell. Plot generated in COMSOL

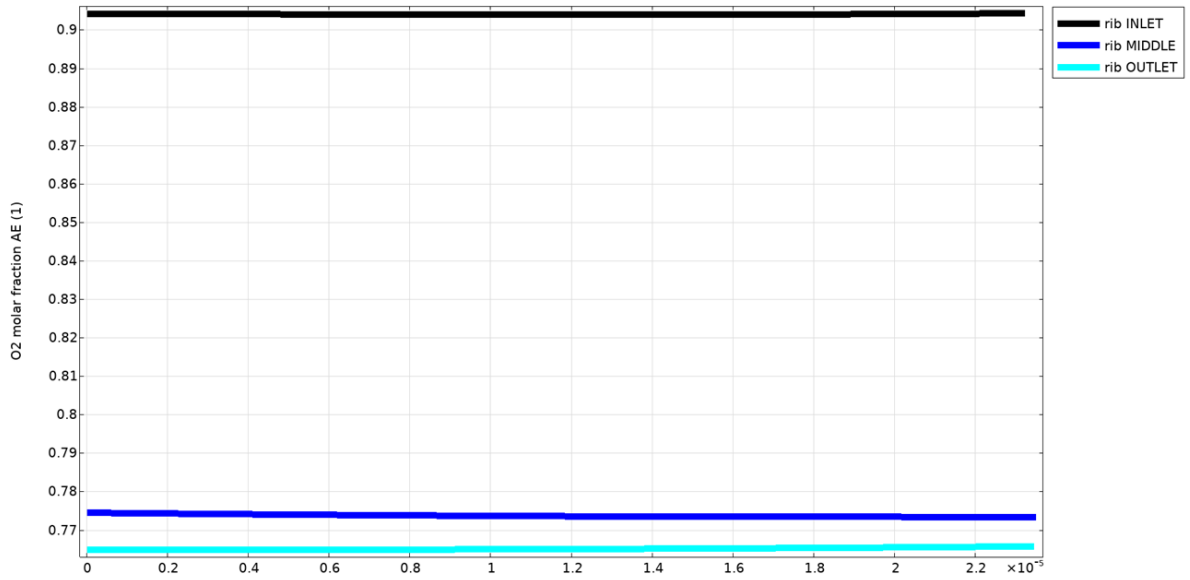

Figure C.8: The profile of oxygen from bottom of the air electrode to the top of the air electrode in the rib region. The bottom of the electrode is the electrode-electrolyte boundary, and the top of the electrode is the electrode-MIC rib boundary. The profile is taken at the inlet, middle and outlet of the cell. Plot generated in COMSOL

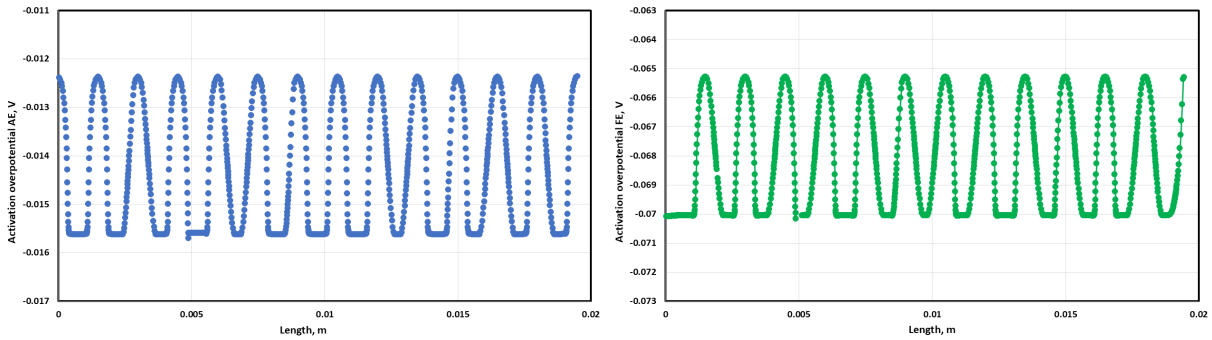

(a) Activation overpotential across the cell on the air side **(b)** Activation overpotential across the cell on the fuel side

Figure C.9: Activation overpotentials across the cell

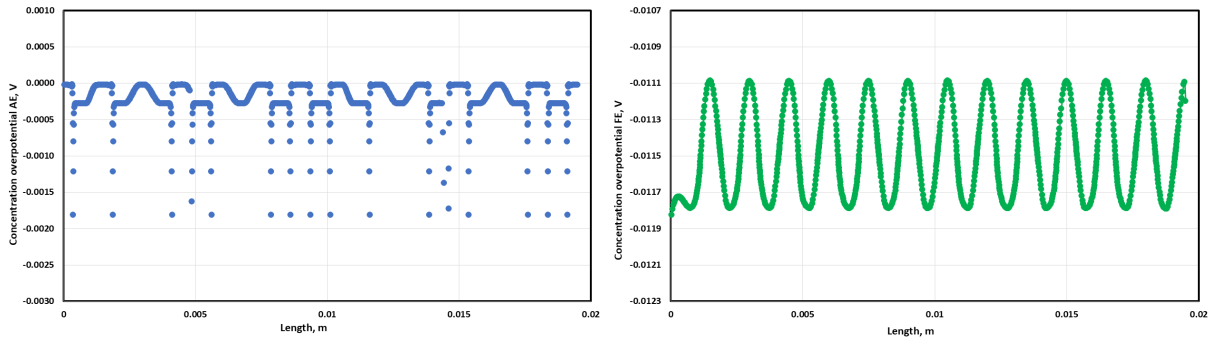

(a) Concentration overpotential across the cell on the air side **(b)** Concentration overpotential across the cell on the fuel side

Figure C.10: Concentration overpotentials across the cell

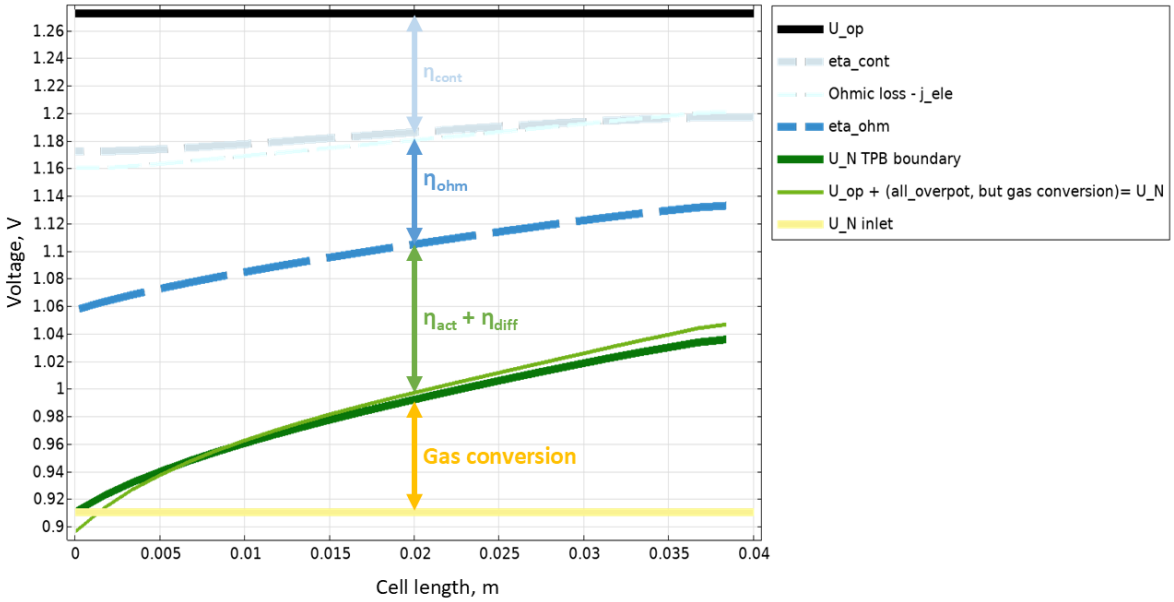

Figure C.11: Call back to the figure Figure 5.14, but with additional checking for local U_N calculation. The thin green line on this plot instead of being calculated from the Nernst voltage formula in Equation 2.3 is calculated as shown on the plot according to the Equation 5.4.

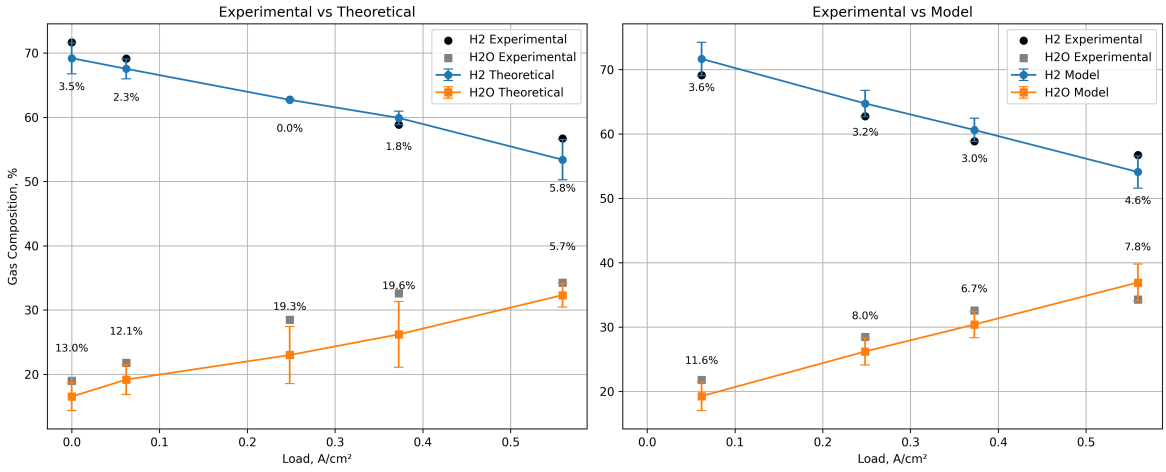

Figure C.12: In Figure 5.6 it can be seen that there are some differences in values calculated theoretically with Faraday law and the ones from the model. To quantify this difference relative errors are calculated between theoretical data set and model data set in relative to the experimentally measured data and plotted as error bars. It can be seen that both approached perform very well in predicting the H_2 contribution. The Faraday approach has larger errors in comparison to model, when it comes to H_2O contribution. That is because the model is able to account for more nuances when it comes to simulation the behavior of each species in the cell.

Appendix D

Appendix: Electrochemical coefficients

The dimensionless parameters for Butler-Volmer equation a, b and c, as well as exchange current densities and charge transfer coefficients are defined through experimental data analysis. An instruction on how to conduct such experiment complete with gas variations can be found in [2].
The overpotentials are calculated based on the current output of the model at given location.
The entropies of reactants and a total entropy are calculated based on their thermodynamic functions and species balance.

Exchange current densities, j_0 $[A/m^2]$

$$j_{0,FE} = \gamma_{FE} \cdot {x_{H2,FE}}^a \cdot {x_{H2O,FE}}^b \cdot exp(-E_{act,FE}/RT) \tag{D.1}$$
$$j_{0,AE} = \gamma_{AE} \cdot {x_{O2,AE}}^m \cdot exp(-E_{act,AE}/RT) \tag{D.2}$$

Overpotentials η $[V]$

$$\eta_{act,FE} = \frac{RT}{2F} \cdot log\left(\frac{x_{H_2O}}{x_{H_2}}\right) + \phi_{el} - \phi_{ion} \tag{D.3}$$
$$\eta_{act,AE} = \frac{-\Delta G_0}{2F} + \frac{RT}{4F} \cdot log|x_{O_2}| - \phi_{el} + \phi_{ion} \tag{D.4}$$
$$\eta_{con,FE} = \frac{RT}{2F} \cdot log\left(\frac{x_{H_2O} \cdot x_{H_2,bulk}}{x_{H_2O,\,bulk} \cdot x_{H_2}}\right) \tag{D.5}$$
$$\eta_{con,AE} = \frac{RT}{4F} \cdot log\left(\frac{x_{O_2,\,bulk}}{x_{O_2}}\right) \tag{D.6}$$
$$\eta_{ohm} = \phi_{ion,FE\ TPB} - \phi_{ion,AE\ TPB} \tag{D.7}$$
$$\tag{D.8}$$

Entropies S $[J/\ molK]$
Reaction entropy is denoted with ΔS_{tot} in Equation D.9. Entropy at operating conditions is denoted with Δ_{ST} in Equation D.13. Reaction entropy at standard conditions is denoted with ΔS_0 in equation D.14. Specific entropies for each species are calculated with changing temperature, taking into consideration changing molar fractions and specific heats. Their entropies and standard conditions are: $S_{H_2O,0} = 188.8J/\ molK$, $S_{H_2,0} = 130.7J/\ molK$, $S_{O_2,0} = 205.1J/\ molK$

$$\Delta S_{tot} = \Delta S_0 + \Delta S_T - R \cdot log\left(\frac{x_{H_2O,TPB\ FE}}{\sqrt{x_{O_2,TPB\ AE}} \cdot x_{H_2,TPB\ FE}}\right) \tag{D.9}$$

$$S_{H2O} = S0_{H_2O} + cp_{H_2O} M_{H_2O} \cdot log\left(\frac{T}{T_{ref}}\right) - R \cdot log(x_{H_2O,TPB\ FE}) \tag{D.10}$$

$$S_{H2} = S0_{H_2} + cp_{H_2} M_{H_2} \cdot log\left(\frac{T}{T_{ref}}\right) - R \cdot log(x_{H_2,TPB\ FE}) \tag{D.11}$$

$$S_{O2} = S0_{O_2} + cp_{O_2} M_{O_2} \cdot log\left(\frac{T}{T_{ref}}\right) - R \cdot log(x_{O_2,TPB\ AE}) \tag{D.12}$$

$$\Delta S_T = cp_{H_2O} M_{H_2O} \cdot log\left(\frac{T}{T_{ref}}\right) - cp_{H_2} M_{H_2} \cdot log\left(\frac{T}{T_{ref}}\right) - 0.5 \cdot cp_{O_2} M_{O_2} \cdot log\left(\frac{T}{T_{ref}}\right) \tag{D.13}$$

$$\Delta S_0 = S_{0,H_2O} - S_{0,H_2} - 0.5 \cdot S_{0,O_2} \tag{D.14}$$

Gibbs free energy at operating point $[J/\ molK]$

$$G_{0,op} = -239694 + 18.76 \cdot T_{op,dim} \cdot log(T_{op,dim}) - 9.25 \cdot T_{op,dim} \tag{D.15}$$

Appendix E

Appendix: Microstructure

This appendix is dedicated to storing relevant information about the microstructure of the investigated cell porous layers used in the model based on an analytical report. As well as some material parameters of the cell holder that are crucial in the model.

E.1 Analytical report of the microstructure

A sample cell was analyzed to investigate its microstructure and composition. One part of the sample was embedded in a conductive resin for cross-sectional imaging. Different regions of the cell, including the FE, FE support, AE, and contact layer, were analyzed.
This analysis and measurements were conducted by the CR/ANA2 department of Robert Bosch GmbH. The conclusions about the cell compositions and layer thicknesses and material analysis were delivered in a report form.
Based on these measurements thickness of each cell layer was determined. Pore sized were estimated and porosities calculated based on that estimation.

In the Figure E.1 a scan of the FE layer is presented, but it is also possible to see the electrolyte. FE is the structure on the bottom of the picture, electrolyte on the top. The light phase in the picture are pores and the dark phase the ceramic in the cer-met material. The anode shows a homogeneous pore structure with fine pores and particles close to the electrolyte, while further away from the electrolyte (bottom of the picture), the structure is more coarse.

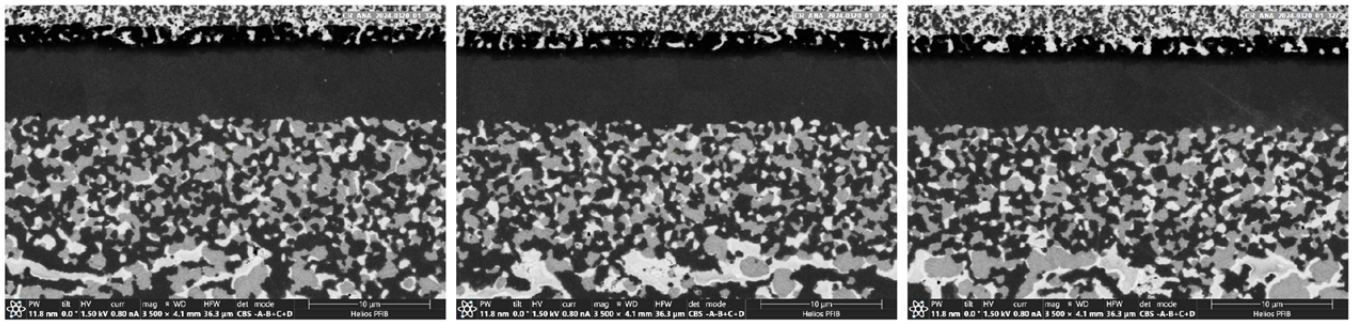

Figure E.1: Fuel electrode

In the Figure E.2 electrolyte and GDC layer are visible. The tight layer in the middle is the electrolyte while the more porous layer above is the GDC.

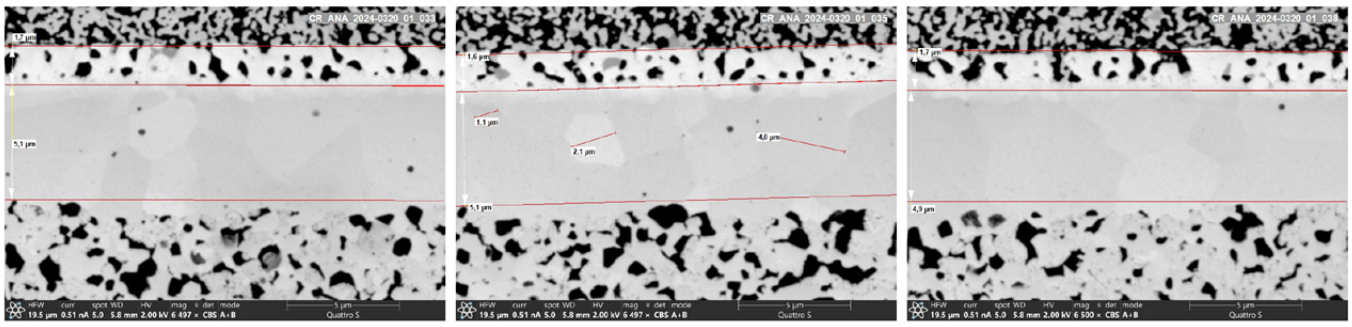

Figure E.2: Electrolyte and GDC barrier layer

In the Figure E.3 there are scans of AE layers. The AE substrate layer and the AE functional layer exhibit two different structures. The AE functional layer (bottom of the picture) shows a nearly homogeneous structure. The substrate layer (top of the picture) has smaller particle and pore sizes. Near the surface, large pores and structural defects (cracks and pore clusters) are present.

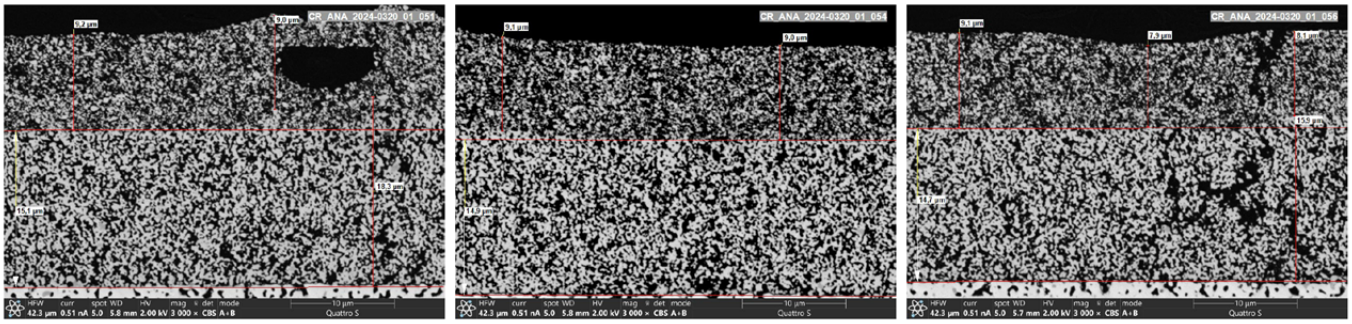

Figure E.3: Air electrode

E.2 Material parameters in the model

MIC	
Parameter	**Expression/Value**
σ_{el}	$4.5 \cdot 10^6 \quad [S/m]$
σ_{ion}	$0 \quad [S/m]$
ρ	$7700 \quad [kg/m^3]$
λ	$24 \quad [W/(mK)]$
Cp	$660 \quad [J/(kgK)]$

Air in gas channel	
Parameter	**Expression/Value**
ψ_{air}	ϕ_{air}/τ_{air}
k	$(1.5/2)^{2/8} \quad [m^2]$
ρ	$(p \cdot M_{air})/RT$
λ	$(\lambda_{O_2}/(1+(x_{N_{2,AE}}/x_{O_{2,AE}})\cdot\Phi_{O_2-N_2})) + (\lambda_{N_2}/(1+(x_{O_{2,AE}}/x_{N_{2,AE}})\cdot\Phi_{N_2-O_2}))$
Cp	$(w_{O_2,AE}\cdot Cp_{O_2} + w_{N_2,AE}\cdot Cp_{N_2})$
R_{air}	R/M_{air}
p	p_{atm}
$\Phi_{O_2-N_2}$	$((1+\sqrt{\eta_{O_2}/\eta_{N_2}}\cdot([M_{N_2}/M_{O_2}]^{0.25})^2/\sqrt{8\cdot(1+(M_{O_2}/M_{N_2})}$
$\Phi_{N_2-O_2}$	$(1+\sqrt{\eta_{N_2}/\eta_{O_2}}\cdot([M_{O_2}/M_{N_2}]^{0.25})^2/\sqrt{8\cdot(1+(M_{N_2}/M_{O_2})}$

AE substrate	
Parameter	**Expression/Value**
ψ_{solid}	$\phi_{solid}/\tau_{solid}$
σ_{el}	$(4860.1 - 2.98\cdot T_{dim})\ [S/cm]\cdot\psi_{solid}$
σ_{ion}	$(1.31\cdot10^4\cdot exp(-11274/T_{dim}))\ [S/cm]\cdot\psi_{solid}$
ρ	$rho_{air}\cdot\phi_{gas} + 6310\ [kg/m^3]\cdot\phi_{solid} +$
λ	$0.25\cdot(3\cdot\psi_{gas}-1)\cdot\lambda_{air} + (3\cdot\psi_{solid}-1)\cdot 3.94 \quad [W/(mK)] + \sqrt{((3\cdot\psi_{solid})\cdot\lambda_{air} + (3\cdot(\psi_{solid}-1)\cdot 3.94\ [W/(mK)])^2 + 8\cdot\lambda_{air}\cdot 3.94\ [W/(mK)]}$
Cp	$(799\ [J/(kgK)]\cdot 6310\ [kg/m^3]\cdot\phi_{solid} + Cp_{air}\cdot\rho_{air}\cdot\phi_{gas})/\rho$

AE functional	
Parameter	**Expression/Value**
ψ_{solid}	$\phi_{solid}/\tau_{solid}$
σ_{el}	$(4860.1 - 2.98\cdot T_{dim})\ [S/cm]\cdot\psi_{solid}$
σ_{ion}	$(1.31\cdot10^4\cdot exp(-11274/T_{dim}))\ [S/cm]\cdot\psi_{solid}$
ρ	$rho_{air}\cdot\phi_{gas} + 6310\ [kg/m^3]\cdot\phi_{solid} +$
λ	$0.25\cdot(3\cdot\psi_{gas}-1)\cdot\lambda_{air} + (3\cdot\psi_{solid}-1)\cdot 3.94 \quad [W/(mK)] + \sqrt{((3\cdot\psi_{solid})\cdot\lambda_{air} + (3\cdot(\psi_{solid}-1)\cdot 3.94\ [W/(mK)])^2 + 8\cdot\lambda_{air}\cdot 3.94\ [W/(mK)]}$
Cp	$(799\ [J/(kgK)]\cdot 6310\ [kg/m^3]\cdot\phi_{solid} + Cp_{air}\cdot\rho_{air}\cdot\phi_{gas})/\rho$

GDC barrier	
Parameter	**Expression/Value**
σ_{el}	$(3.46\cdot10^9/T_{dim})\cdot exp(-28779/T_{dim})\cdot(p_{O_2,AE}/1\ [atm])^{-0.25} \quad [S/cm]$
σ_{ion}	$(1.09\cdot10^5/T_{dim})\cdot exp(-7426.9/T_{dim})\cdot(1+\Delta_{CGO}/0.05) \quad [S/cm]$
ρ	$7210 \quad [kg/m^3]$
λ	$0.98 \quad [W/(mK)]$
Cp	$521 \quad [J/(kgK)]$
p	$c_{AE}\cdot RT$

YSZ electrolyte	
Parameter	**Expression/Value**
σ_{el}	$0 \quad [S/m]$
σ_{ion}	$(9.794 \cdot 10^{-5} \cdot T_{dim}^2 - 0.1697 \cdot T_{dim} + 7416) \quad [S/m]$
ρ	$5938 \quad [kg/m^3]$
λ	$2.1 \quad [W/(mK)]$
Cp	$636 \quad [J/(kgK)]$

FE functional	
Parameter	**Expression/Value**
ψ_{el}	ϕ_{el}/τ_{el}
ψ_{ion}	ϕ_{ion}/τ_{ion}
σ_{el}	$(7 \cdot 10^7 \cdot T_{dim}^{-0.508}) \quad [S/m] \cdot \psi_{el}$
σ_{ion}	$(9.794 \cdot 10^{-5} \cdot T_{dim}^2 - 0.1697 \cdot T_{dim} + 7416) \quad [S/m] \cdot \psi_{ion}$
ρ	$8850 \cdot \phi_{el} + 5938 \cdot \phi_{ion} + \rho_{fuel} \cdot \phi_{gas} \quad [kg/m^3]$
λ	$(5.545 - 2.036 \cdot (\lambda_{fuel}/(1\ [W/(mK)]))^2 + 2.694 \cdot (\lambda_{fuel}/(1[W/(mK)]))) * 1[W/(mK)]$
Cp	$(549 \cdot 8850 + 636 \cdot 5938 + Cp_{fuel} \cdot \rho_{fuel})/\rho$

FE substrate	
Parameter	**Expression/Value**
ψ_{ion}	$1 - \psi_{gas} - \psi_{el}$
ψ_{el}	ψ_{el}/τ_{el}
ψ_{ion}	ψ_{ion}/τ_{ion}
σ_{el}	$(7 \cdot 10^7 \cdot T_{dim}^{-0.508}) \quad [S/m] \cdot \psi_{el}$
σ_{ion}	$(9.794 \cdot 10^{-5} \cdot T_{dim}^2 - 0.1697 \cdot T_{dim} + 7416) \quad [S/m] \cdot \psi_{ion}$
ρ	$8850 \cdot \phi_{el} + 5938 \cdot \phi_{ion} + \rho_{fuel} \cdot \phi_{gas} \quad [kg/m^3]$
λ	$(5.545 - 2.036 \cdot (\lambda_{fuel}/(1\ [W/(mK)]))^2 + 2.694 \cdot (\lambda_{fuel}/(1[W/(mK)]))) * 1[W/(mK)]$
Cp	$(549 \cdot 8850 + 636 \cdot 5938 + Cp_{fuel} \cdot \rho_{fuel})/\rho$

Ni contacting layer	
Parameter	**Expression/Value**
ψ_x	ψ_{gas}/τ_x
ψ_y	ψ_{gas}/τ_y
k	$(0.3\ [mm] \cdot 0.5)^{2/8}$
σ_{el}	$(7 \cdot 10^7 \cdot T_{dim}^{-0.508}) \cdot \psi_{solid} \quad [S/m]$
σ_{ion}	$0 \quad [S/m]$
ρ	$8850 \cdot (1 - \psi_{solid}) + \rho_{fuel} \cdot \phi_{gas} \quad [kg/m^3]$
λ	$(66.2] + \lambda_{fuel})/2 \quad [W/(mK)$
Cp	$(549 \cdot 8850 \cdot \phi_{solid} + Cp_{fuel} \cdot \rho_{fuel} \cdot \phi_{gas})/\rho \quad [J/(kgK)]$

Fuel mixtures in gas channel	
Parameter	**Expression/Value**
k	$1^{2/8} \quad [m^2]$
ρ	$p \cdot M_{fuel}/RT$
λ	$(x_{H_2,FE} \cdot \lambda_{H_2}/(x_{H_2O,FE} \cdot \Phi_{H_2-H_2O} + x_{N_2,FE} \cdot \Phi_{H_2-N_2}) + (x_{H_2O,FE} * \cdot \lambda_{H_2O}/(x_{H_2,FE} \cdot \Phi_{H_2O-H_2} + x_{N_2,FE} \cdot \Phi_{H_2O-N_2}) + (x_{N_2,FE} \cdot \lambda_{N_2}/x_{H_2,FE} \cdot \Phi_{N_2-H_2} + x_{H_2O,FE} \cdot \Phi_{H_2-H_2O})$
Cp	$w_{H_2} \cdot Cp_{H_2} + w_{H_2O} \cdot Cp_{H_2O} + w_{N_2} \cdot Cp_{N_2}$
R_{fuel}	R/M_{fuel}
p	p_{atm}
$\Phi_{H_2-H_2O}$	$((1 + \sqrt{\eta_{H_2}/\eta_{H_2O}} \cdot ([M_{H_2O}/M_{H_2}]^{0.25})^2)/\sqrt{8 \cdot (1 + (M_{H_2}/M_{H_2O})}$
$\Phi_{H_2-N_2}$	$((1 + \sqrt{\eta_{H_2}/\eta_{N_2}} \cdot ([M_{N_2}/M_{H_2}]^{0.25})^2)/\sqrt{8 \cdot (1 + (M_{H_2}/M_{N_2})}$
$\Phi_{H_2O-H_2}$	$((1 + \sqrt{\eta_{H_2O}/\eta_{H_2}} \cdot ([M_{H_2}/M_{H_2O}]^{0.25})^2)/\sqrt{8 \cdot (1 + (M_{H_2O}/M_{H_2})}$
$\Phi_{H_2O-N_2}$	$((1 + \sqrt{\eta_{H_2O}/\eta_{N_2}} \cdot ([M_{N_2}/M_{H_2O}]^{0.25})^2)/\sqrt{8 \cdot (1 + (M_{H_2O}/M_{N_2})}$
$\Phi_{N_2-H_2}$	$((1 + \sqrt{\eta_{N_2}/\eta_{H_2}} \cdot ([M_{H_2}/M_{N_2}]^{0.25})^2)/\sqrt{8 \cdot (1 + (M_{N_2}/M_{H_2})}$

Heat conductivities	
λ_{H_2}	$0.00065 + 0.000767 \cdot T_{dim} + (-0.00000068705) \cdot T_{dim}^2 + 0.00000000050651 \cdot T_{dim}^3 + (-1.3854 \cdot 10^{-13})) \cdot T_{dim}^4 \quad [W/(mK)]$
λ_{H_2O}	$0.00985662 + (-0.000007301)) \cdot T_{dim} + 0.000000150213 \cdot T_{dim}^2 + (-6.93495 \cdot 10^{-11})) \cdot T_{dim}^3 + (1.38865 \cdot 10^{-14})) \cdot T_{dim}^4 \quad [W/(mK)]$
λ_{N_2}	$0.00683232 + 0.0000694038 \cdot T_{dim} + (-0.0000000175067)) \cdot T_{dim}^2 + (1.05678 \cdot 10^{-11})) \cdot T_{dim}^3 + (-3.44998 \cdot 10^{-15})) \cdot T_{dim}^4 \quad [W/(mK)]$
λ_{O_2}	$0.00518436 + 0.0000673456 \cdot T_{dim} + 0.0000000171345 \cdot T_{dim}^2 + (-0.000000000029421)) \cdot T_{dim}^3 + (1.02427 \cdot 10^{-14})) \cdot T_{dim}^4 \quad [W/(mK)]$

Specific heats	
Cp_{H_2}	$13973.4 + 1.256 \cdot T_{dim} + (-0.000892) \cdot T_{dim}^2 + 0.00000066 \cdot T_{dim}^3 + (-0.000000229)) \cdot T_{dim}^{-2} \quad [J/(kgK)]$
Cp_{H_2O}	$2276.28 + (-2.15444) \cdot T_{dim} + 0.00448909 \cdot T_{dim}^2 + (-0.0000031526)) \cdot T_{dim}^3 + 8.333331 \cdot 10^{-10} \cdot T_{dim}^4 \quad [J/(kgK)]$
Cp_{N_2}	$1152.67 + (-0.752701) \cdot T_{dim} + 0.00160418 \cdot T_{dim}^2 + (-0.00000109594) \cdot T_{dim}^3 + 0.000000000259629 \cdot T_{dim}^4 \quad [J/(kgK)]$
Cp_{O_2}	$968.07 + (-0.693956) \cdot T_{dim} + 0.0023989 \cdot T_{dim}^2 + (-0.00000239707) \cdot T_{dim}^3 + 0.000000000814754 \cdot T_{dim}^4 \quad [J/(kgK)]$

Viscosities	
η_{H_2}	$0.0000018024 + 0.000000027174 \cdot T_{dim} + -0.000000000013395 \cdot T_{dim}^2 + 5.85 \cdot 10^{-15} \cdot T_{dim}^3 + (-1.04 \cdot 10^{-18}) \cdot T_{dim}^4 \quad [Pa \cdot s]$
η_{H_2O}	$0.00000237183 + 0.00000000958814 \cdot T_{dim} + 6.24661 \cdot 10^{-11} \cdot T_{dim}^2 + (-5.13493 \cdot 10^{-14}) \cdot T_{dim}^3 + 1.45102 \cdot 10^{-17} \cdot T_{dim}^4 \quad [Pa \cdot s]$
η_{N_2}	$0.00000193821 + 0.000000064154 \cdot T_{dim} + (-4.19383 \cdot 10^{-11}) \cdot T_{dim}^2 + 2.25321 \cdot 10^{-14} \cdot T_{dim}^3 + (-5.10056 \cdot 10^{-18}) \cdot T_{dim}^4 \quad [Pa \cdot s]$
η_{O_2}	$0.000000901365 + 0.0000000811935 \cdot T_{dim} + (-5.95702 \cdot 10^{-11}) \cdot T_{dim}^2 + 3.5739 \cdot 10^{-14} \cdot T_{dim}^3 + (-9.18689 \cdot 10^{-18}) \cdot T_{dim}^4 \quad [Pa \cdot s]$

Appendix F

Appendix: Kramers-Kronig relations

F.1 Kramers-Kronig relations

The Kramers-Kronig (K-K) relations are fundamental mathematical expressions that establish a connection between the real and imaginary components of a complex frequency-dependent function, such as impedance. In the context of EIS, they enable the estimation of the imaginary part of the impedance $Z''(\omega)$ from the known real part $Z'(\omega)$ over a given frequency range—and vice versa—as shown in Equations F.1 and F.2. These transformations are defined over the frequency domain from zero to infinity and are used to verify whether the measured impedance data are self-consistent.

The K-K relations are particularly important for validating the internal consistency of EIS data. If the measured real and imaginary parts of the impedance are not consistent with each other according to these relations, it may indicate experimental errors, such as noise, drift, or non-ideal measurement conditions. However, while compliance with the K-K relations is necessary for a valid linear system, it is not sufficient to confirm linearity. This is because the K-K test is not highly sensitive to subtle nonlinear behavior. Therefore, linearity is often verified independently by checking whether the impedance remains constant when varying the amplitude of the excitation signal. In this project, EIS parameters are chosen as suggest by D. Klotz in [14].

$$Z''(\omega) = -\left(\frac{2\omega}{\pi}\right)\int_0^\infty \frac{Z'(x) - Z'(\omega)}{x^2 - \omega^2}\,dx \qquad Z''(\omega) \text{ from measured } Z'(\omega) \tag{F.1}$$

$$Z'(\omega) - Z'(\infty) = \frac{2}{\pi}\int_0^\infty \frac{xZ''(x) - \omega Z''(\omega)}{x^2 - \omega^2}\,dx \qquad Z'(\omega) \text{ from measured } Z''(\omega) \tag{F.2}$$

In practical terms, EIS experimental data are collected across a given frequency spectrum. To assess data quality, the K-K compliance module in DearEIS (a non-commercial software) is used [23]. This tool calculates the residuals between the measured and K-K reconstructed impedance values. Large residuals indicate poor compliance with the K-K relations, suggesting that the data may be unreliable and should not be used for further interpretation. Common causes of non-compliance include improper measurement settings such as excessive excitation amplitude, insufficient integration time, or system drift during acquisition.

The validity of the K-K test relies on four essential assumptions. If all are fulfilled and the data

still fail the K-K test, the measurement is likely flawed.

- **Causality**
  The system must be causal, meaning the response (current) occurs only after the stimulus (voltage) is applied.
- **Linearity**
  The response must obey the principle of superposition: the output should scale linearly with the input and not contain higher harmonics or mixed frequencies.
- **Stability**
  The system must remain unchanged over the measurement period. Time-dependent changes, such as degradation or thermal drift, violate this condition.
- **Finiteness**
  The impedance must remain finite across all frequencies, including at $\omega \to 0$ and $\omega \to \infty$. Divergent behavior would render the K-K integrals invalid.

F.2 Kramers-Kronig test for EIS data

The Kramers-Kronig test is conducted with a Python tool for EIS data analysis called DearEIS [23]. Each dataset's quality is checked with this test, before being used for further analysis. Per D. Klotz recommendation, only datasets with the lowest residuals laying between are taken into consideration [14].
Here one of the results for the test that is used as a reference in all gas variations. This data set is called "Ref 50-50-air" and serves as a benchmark for comparison in all gas variations.

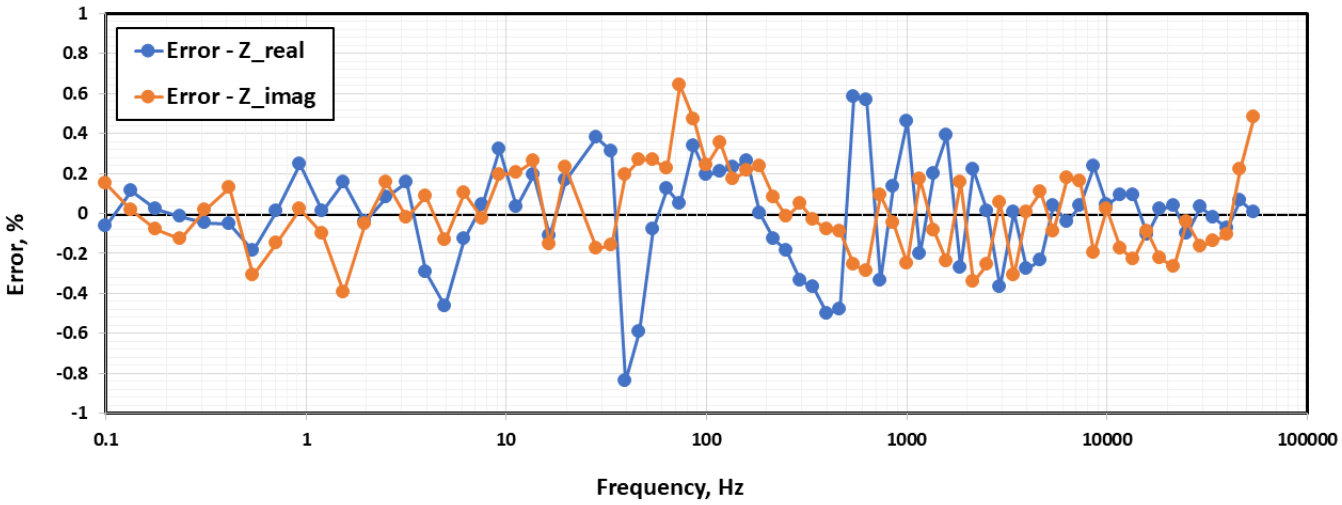

Figure F.1: Calculated residuals from K-K test lay between -1% and 1% meaning that this dataset valid.

Figure F.1 is exported dataset from DearEIS and plotted illustrate the distribution of residuals for the real and imaginary part of EIS measurements. In general it can be seen that for majority of the frequency range the residuals ar smaller than 0.5%. This indicates good compliance with K-K relations, meaning good quality of the dataset.

The reconstructed values fitted to the experimental values are shown in Figure F.2. The fit matches the experimental data very well, without showing unexpected behavior. An imperfection can be seen in the middle of the frequency range, but when looking at the plot above in Figure F.1 it ca be seen that this artifact carries still less than 1% error.

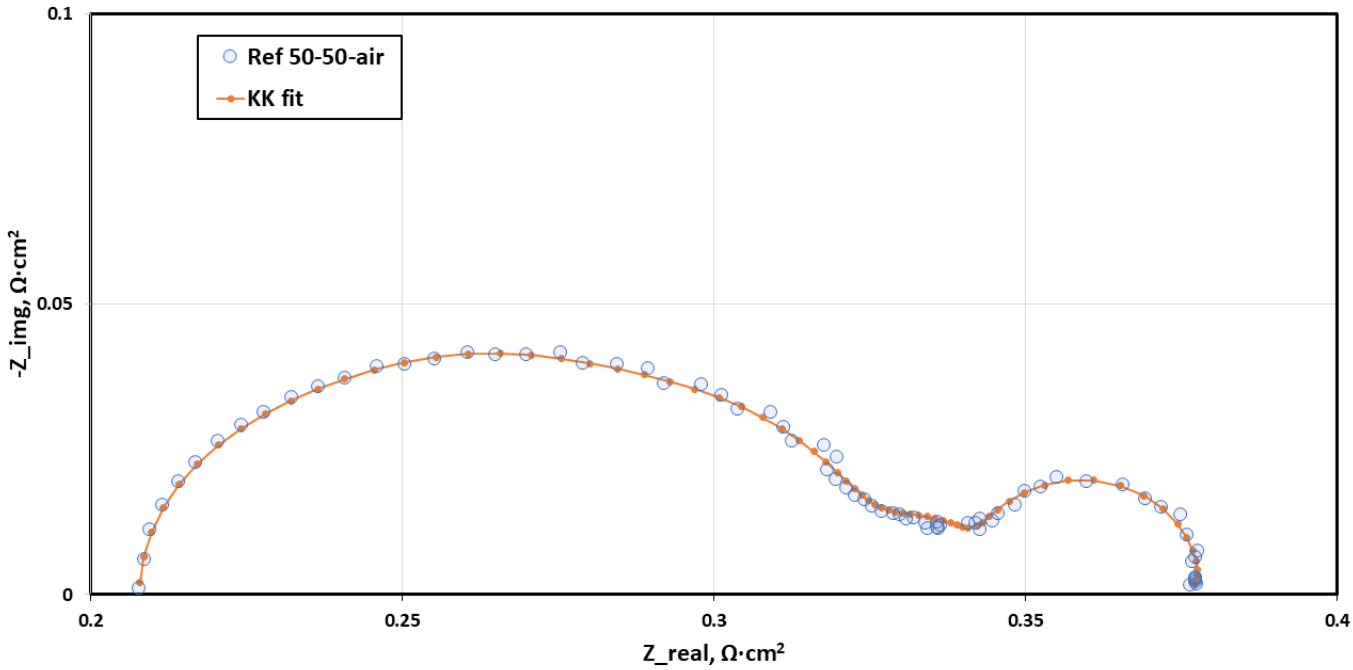

Figure F.2: Good fit of reconstructed and experimental values on a Nyquist plot.

For the discussed EC and FC operating points the data quality deteriorates due to more noise. The assessment for EC operating points is shown in Figure F.3.

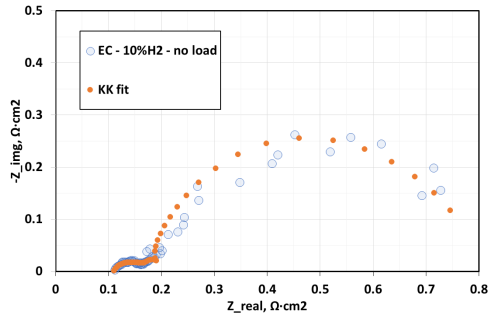

(a) Fit of the EC operating point at OCV

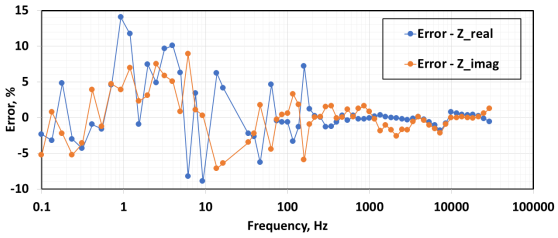

(b) KK residuals of the EC operating point at OCV

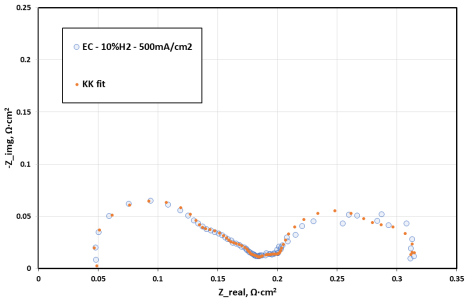

(c) Fit of the EC operating point at 500 mA/cm^2

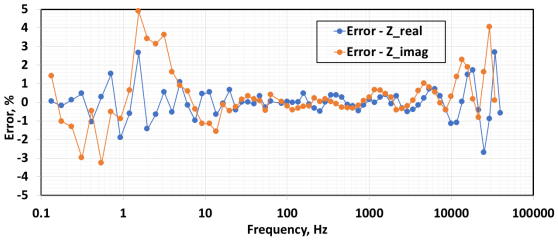

(d) KK residuals of the EC operating point at at 500mA/cm^2

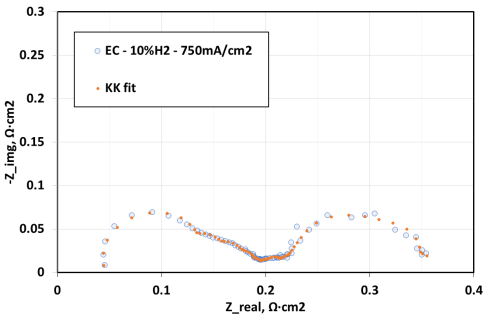

(e) Fit of the EC operating point at 750mA/cm^2

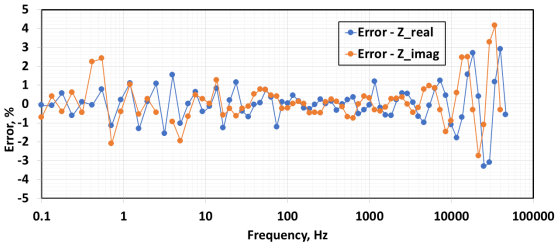

(f) KK residuals of the EC operating point at at 750mA/cm^2

Figure F.3: The EC operating still display decent fits The residuals lay between -5% and 5% for majority of data points. At lowest and highest frequencies datasets have the highest residuals.

Appendix G

Appendix: OCV interpolation in the model

As the model cannot operate at OCV, interpolation is performed to calculate ohmic and polarization loss in the cell. The model is unable to operate at OCV, as no current flows at this voltage. The model is setup in such way, that current density is a necessary variable for computation. A model with an operating voltage sweep is ran for four different U_{op} around OCV. The results read as as averages over the cell area from each these simulations are shown in Figure G.1 in light blue color. While the calculated values for OCV are marked up in darker blue.

U_op, V	J, A/cm2	Local U_N, V	eta_diff+act, V	eta_ohmic, V	eta_cont, V	gas conversion, V	ohmic loss j_ele, V	Total overpot from model, V
0.8	0.0908	0.8233	0.0176	0.0127	0.0071	0.0571	0.0020	0.0804
0.85	0.0965	0.8611	0.0073	0.0060	0.0033	0.0198	0.0020	0.0309
0.9	-0.0302	0.8920	0.0048	0.0043	0.0024	0.0105	0.0020	0.0185
0.95	-0.1208	0.9169	0.1004	0.0174	0.0094	0.0350	0.0020	0.0680
OCV=0.881	0.0000	0.8771	0.0028	0.0042	0.0023	0.0103	0.0020	0.0178

U_op, V	R0 from model, ohm·cm2 (eta_ohmic/J)	Rpol from model, ohm·cm2 (∑ eta + gas convresion/J)	Ro + Rpol in the model, ohm·cm2 (U_N, inlet – U_op)	Ro +Rpol in the model, ohm·cm2 (R0 + Rpol)
0.8	0.13873	1.5317	1.5871	1.67043
0.85	0.14059	0.90191	0.9903	1.0425
0.9	0.14289	0.60443	0.7134	0.74732
0.95	0.1447	0.50744	0.6237	0.65214
OCV=0.881	0.1420	0.6877	**0.7843**	**0.829803**

Figure G.1: A model with a voltage sweep in potentiostatic operation is run. For each model, parameters necessary to calculate the ohmic loss and polarization loss are written down in the table. They are averages over the area of the cell model.

The expressions used to calculate model results in OCV are compiled in the Table G.1.

Table G.1: Expressions for calculated parameters as a function of U_{op}.

Parameter	Unit	Expression
J	A/cm^2	$-1.5227 \cdot U_{op} + 1.3415$
U_N	V	$0.6235 \cdot U_{op} + 0.3278$
$\eta_{act} + \eta_{diff}$	A/cm^2	$10.591 \cdot U_{op}^2 - 18.042 \cdot U_{op} + 7.6775$
η_{ohm}	V	$1.9776 \cdot U_{op}^2 - 3.4356 \cdot U_{op} + 1.496$
Gas Conversion	V	$6.1745 \cdot U_{op}^2 - 10.957 \cdot U_{op} + 1.496$
Ohmic losses of j_{ele}	V	0.002
$\sum \eta$	V	$9.9038 \cdot U_{op}^2 - 17.431 \cdot U_{op} + 7.6876$
$R_0 + R_{pol}$	$\Omega \cdot cm^2$	$50.709 \cdot U_{op}^2 - 95.075 \cdot U_{op} + 45.187$
R_0	$\Omega \cdot cm^2$	η_{ohmic}/J
R_{pol}	$\Omega \cdot cm^2$	$(\eta_{act} + \eta_{diff} + \text{Gas Conversion})/J$
Sum by hand, $R_0 + R_{pol}$	$\Omega \cdot cm^2$	$R_0 + R_{pol}$

G.1 EC and FC operating points

Even though the results under loads are not fit to be compared with the model, it is interesting to see the influence of load on the measurement, as it is a point of analysis in the MS measurements. The results are shown in Figure G.2.

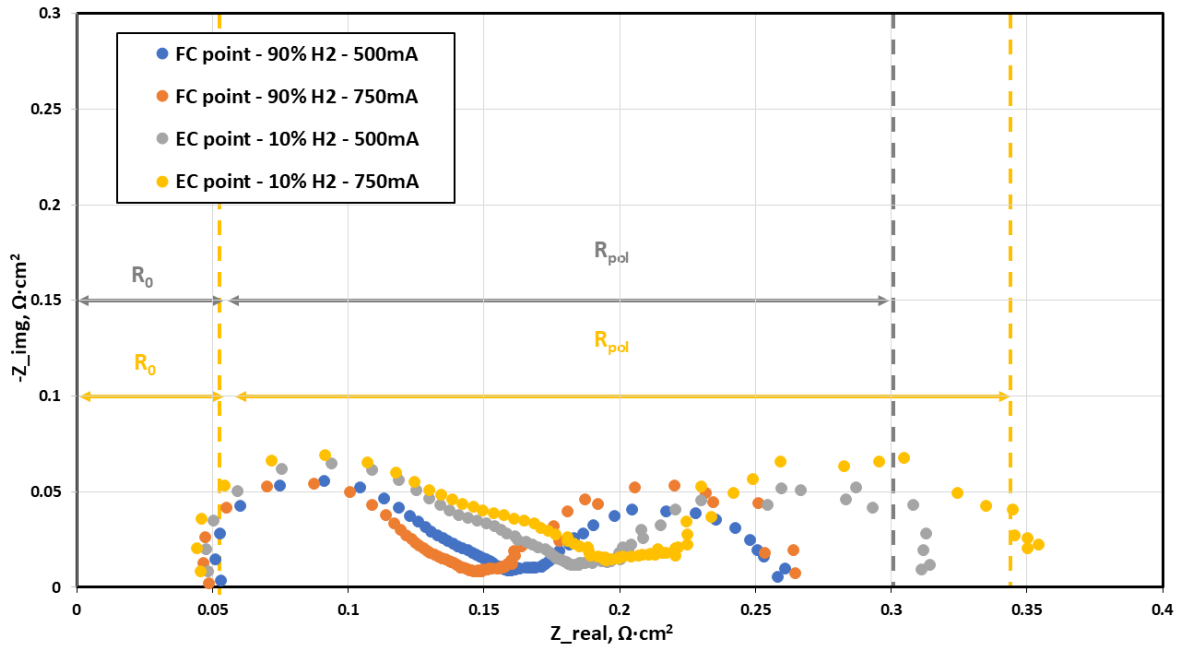

Figure G.2: EIS spectrum of two operating points under loads (500mA/cm^2 and 750 mA/cm^2). Flow on the fuel side: 193 ml/min, with 90% H_2O in EC and 10% H_2O in FC

In the Figure G.2, the ohmic resistance and polarization resistance can be read directly, as introduced in Figure 2.6. EC operating points consistently exhibit higher total polarization resistance than FC points. The semicircles at low frequencies are wider in EC mode, indicating greater concentration loss. Additionally, higher current loads result in increased polarization resistance, further supporting the conclusion that gas conversion becomes a dominant loss mechanism under loads.

Because the active area of the cell is 16 cm^2, a significant influence of gas conversion losses is expected [31], which could be attributed to the significant influence of the concentration overpotential. This size is deliberately chosen, as the goal is to assess gas composition changes along the cell with mass spectrometry. In such larger cells, activation loss tends to be less distinguishable on the Nyquist plots, or even for DRT analyses. As the semi circles/peaks showing concentration overpotentials overlap in frequency with the peaks representing electrochemical effects.